Naval Research Laboratory

Washington, DC 20375-5320

Wide Area Detection and Identification of Underwater UXO Using Structural Acoustic Sensors – Final Report to SERDP MR-1513

J.A. Bucaro

Excet, Inc.
Springfield, Virginia

B.H. Houston
H. Simpson
Z. Waters
M. Saniga
S. Dey
A. Sarkissian

Physical Acoustics Branch
Acoustics Division

D. Calvo

Acoustic Systems Branch
Acoustics Division

L. Kraus
T. Yoder

Global Defense Technology and Systems Inc.
Crofton, Maryland

July 8, 2011

REPORT DOCUMENTATION PAGE

Form Approved
OMB No. 0704-0188

1. REPORT DATE *(DD-MM-YYYY)*	2. REPORT TYPE	3. DATES COVERED *(From - To)*
08-07-2011	Memorandum Report	

4. TITLE AND SUBTITLE

Wide Area Detection and Identification of Underwater UXO Using Structural Acoustic Sensors – Final Report to SERDP MR-1513

5a. CONTRACT NUMBER

5b. GRANT NUMBER

5c. PROGRAM ELEMENT NUMBER

6. AUTHOR(S)

J.A. Bucaro,* B.H. Houston, H. Simpson, Z. Waters, M. Saniga, S. Dey, A. Sarkissian, D. Calvo, L. Kraus,† T. Yoder,†

5d. PROJECT NUMBER
MR-1513

5e. TASK NUMBER

5f. WORK UNIT NUMBER
71-9024

7. PERFORMING ORGANIZATION NAME(S) AND ADDRESS(ES)

Naval Research Laboratory, Code 7130
4555 Overlook Avenue, SW
Washington, DC 20375-5350

8. PERFORMING ORGANIZATION REPORT NUMBER

NRL/MR/7130--11-9337

9. SPONSORING / MONITORING AGENCY NAME(S) AND ADDRESS(ES)

SERDP Program Office
901 North Stuart St., Suite 303
Arlington, VA 22203

10. SPONSOR / MONITOR'S ACRONYM(S)
SERDP

11. SPONSOR / MONITOR'S REPORT NUMBER(S)

12. DISTRIBUTION / AVAILABILITY STATEMENT

Approved for public release; distribution is unlimited.

13. SUPPLEMENTARY NOTES

*On-site contractor with Excet, Inc. Springfield, VA 22151
†On-site contractor with Global Defense Technology & Systems, Inc. Crofton, MD 21114

14. ABSTRACT

This project explored the feasibility and advantages of applying the structural acoustic feature-based technique to the detection and identification of underwater unexploded ordnance (UXO) especially for buried targets. In the structural acoustic regime, the echoes are related to the vibrational dynamics of the object, and time-frequency features in the scattered echoes can be used to "fingerprint" the target. The research centered around (1) comprehensive state-of-the-art UXO scattering measurements in the NRL structural acoustic underwater laboratory free-field and sediment facilities and off the coast of Panama City, FL, using a rail-based robotic sonar system and (2) the application of time and frequency based numerical models. The structural acoustic approach to target detection and identification offers significant advantages over more conventional acoustic approaches which rely on the formation of high resolution images. These advantages include: diverse set of "fingerprints" leading to low false alarm rates; longer range operation leading to wide area coverage; and low frequency sediment penetration leading to buried target prosecution.

15. SUBJECT TERMS

Underwater UXO
Structural acoustic identification
Sonar detection of UXO

16. SECURITY CLASSIFICATION OF:			17. LIMITATION OF ABSTRACT	18. NUMBER OF PAGES	19a. NAME OF RESPONSIBLE PERSON
a. REPORT	**b. ABSTRACT**	**c. THIS PAGE**	UL	85	B.H. Houston
Unclassified	Unclassified	Unclassified			**19b. TELEPHONE NUMBER** *(include area code)* (202) 404-3840

Standard Form 298 (Rev. 8-98)
Prescribed by ANSI Std. Z39.18

TABLE OF CONTENTS

LIST OF TABLES

LIST OF FIGURES

with respect to the sediment surface; b)90 degrees with respect to the sediment surface.

Figure 37 – Ensemble Averaged Reverberation Backscattered Intensity. Time series for the half-buried infinite cylinder and a 2 degree source angle.

Figure 38 – Ensemble Averaged Target Echo versus Reverberation Backscattered Intensity. The time series are shown for 2º, 28º (critical angle), and 90º source angles. The simulation used a wide-band Ricker source pulse centered at 10 kHz covering a band 2 kHz to 30 kHz.

Figure 39 – Bistatic TS Measurements for Five-Inch Rocket. Bistatic target strength displayed in dB as a color map measured for the five-inch rocket.

Figure 40 – Measured Forward Scattering TS versus Analytic Model. Measured free-field forward scattered target strength versus frequency in black. (a) 90° source; blue/green soft/rigid boundary condition theory, respectively; (b) 0° source; blue theory.

Figure 41 – Possible Forward Scattering System Geometry, Corresponding Range-Cross Range Plots, and Forward Scattered TS versus Frequency And Angle. (a) Hypothetical long range forward scattering measurement range: R_{ST}, R_{SR}, and R_{TR} are the source to target distance, the distance from the source to a particular receiver, and the distance from the target to a particular receiver, respectively; (b) time-cross range plots in dB for the direct source 150 meters from the center receiver (heavy line) and for the forward scattered signal x 30 with TS given by Eq. 4; (c) scattering TS in dB versus frequency and angle in the forward scattered sector for the scattering response given by Eq. (4); and (d) that extracted from the numerical results shown in (b).

Figure 42 – Measurement Details at St. Andrew's Bay. Upper right: Measurement site and water depths; lower right: UXO targets and their positions and the locations of the source and rail based sensor system; upper left: drawing of the source and rail system with both a moving source and receiver.

Figure 43 – Measured Target Strength. Magnitude of the bistatic target strength for 0° incidence coded in color versus frequency and scattering angle as measured in the Bay (left) and in the sediment pool (right) for the proud 155 mm shell.

Figure 44 – Measured Target Strength. Magnitude of the bistatic target strength for 0° incidence coded in color map versus frequency and scattering angle as measured in the Bay (left) and in the sediment pool (right) for the proud155mm shell.

Figure 45 – Simulated Effect of Propagation on the Monostatic TS. Upper left: Measured monostatic free-field target strength versus angle and frequency for the 155mm shell shown in the upper photograph; lower: the measured and simulated (using RAM) acoustic pressure in the water and sediment versus time at the receiver for the St. Andrew's Bay site.

Figure 46 – The Major Rays Which Account for the Acoustic Propagation in the Water Column and Sediment. Upper: The important rays from the source to the receiver array; lower: the measured and simulated (using RAM) acoustic pressure in the water and sediment versus time at

the receiver for the St. Andrew's Bay site with some of the ray arrival times identified with arrows.

Figure 47 – Target Strength versus Frequency and Aspect Measured in St. Andrew's Bay Compared to That Simulated Using RAM and the Laboratory Measured Free-Field TS. In the Bay results, the stationary source and moving receiver are 42 and 52 meters, respectively, from the 155mm shell target.

Figure 48 – Typical Forward Scatter Geometry. Point source and real or synthetic receiver array.

Figure 49 – Log of Ratio of Source to Scattered Pressure. Parameterized by total range and plotted versus source to target distance over total range.

Figure 50 –Forward Scatter Measurements in the Gulf of Mexico. Cartoon of the rail system, measurement geometry, and photo of the spherical shell.

Figure 51 – Range – Cross-Range Maps of Gulf Receiver Measurements. Left: unfiltered data with various ray paths labeled. Right: after filtering using the wavenumber filter.

Figure 52 – Forward Scatter Acoustic Color Maps. Left: rail measurement after filtering. Middle: computation with four rays. Right: finite element calculation.

Figure 53 – Target Strength versus Frequency. TS at various angles for the filtered measurement (red), ray calculation (blue), and finite element calculation (green).

Figure 54 – The Three UXO Sonar Configurations. The case 3 look-down configuration is highlighted. It is a short range, above critical angle, limited bistatic angle configuration.

Figure 55 – New Look-Down Measurement System in the NRL Sediment Pool. The system uses a near-field synthetic receiver array and a single point source.

Figure 56 – Diagram for Buried Target Scattering Measurements. The targets are buried 10 cm below the surface and include a five inch rocket (horizontal and 30 degree pitch), a rock, and a cinder block (flat and a 45 degree roll).

Figure 57 – Sediment Pool Look-Down Measurements. Geometry and range (time) cross-range (receiver position) plots for one line scan.

Figure 58 – Target Strength versus Frequency and Angle. Targets include the five inch rocket, the rock, and the cinder block flat and rolled 45 degrees. Upper displays for line scan A and lower displays for line scan B.

Figure 59 – Target Feature Separation for RVM. Red curves for the five inch rocket (horizontal and 30 degree pitch) blue curves for the rock and cinder block (flat and rolled 45 degrees) for various S/N ratios.

LIST OF ACRONYMS

AUV – Autonomous underwater vehicle
CSS – Coastal Systems Station, Panama City, FL
EFIT – Elastodynamic finite integration technique
HMM – Hidden Markov models
ID – Identification
KMP – Kernal Matching Pursuits
LDV – Laser Doppler vibrometry
Logit – Logistic regression
LSA – Laboratory for Structural Acoustics
MigLogit – Migratory logistic regression
NAH – Nearfield acoustic holography
NRL – Naval Research Laboratory
PE – Parabolic Equation
PML – Perfectly matched layer
RVM – Relevance vector machines
SA – Structural Acoustics
SERDP – Strategic Environmental Research and Development Program
TS – Target strength
UXO – Unexploded ordnance

KEYWORDS

Underwater UXO, structural acoustic identification, sonar detection of UXO

ACKNOWLEDGEMENT

ABSTRACT

Objective

This project explored the feasibility and advantages of applying the structural acoustic feature-based technique to the detection and identification of underwater unexploded ordnance, especially for buried targets. In the structural acoustic regime, the echoes are related to the vibrational dynamics of the object, and time-frequency features in the scattered echoes can be used to "fingerprint" and identify the target.

Technical Approach

The research focused on (1) comprehensive state-of-the-art UXO scattering measurements in the NRL structural acoustic underwater laboratory free-field and sediment facilities and off the coast of Panama City, FL using a rail-based robotic sonar system and (2) the application of time and frequency based numerical models.

Results

The majority of the effort was associated with the long range *mono-static* scenario, and the research established the following. (1) Typical proud or partially buried UXO have sufficiently high target strength levels over the structural acoustic frequency band to be detectable out to modest ranges. (2) RVM identification algorithms trained on data in this band allow one to distinguish between UXO and non-UXO and to also distinguish between various UXO themselves. (3) RVM training data will have to include echoes for various burial pitch angles in addition to in-plane aspect angles. (4) Multi-path acoustic propagation significantly alters the frequency-angle features; however, a realistic propagation model can be used to include this complication in the operation of the RVM identification process. A relatively modest portion of the program's efforts was expended on the long range *bi-static* scenario, in particular forward and near-forward scattering. Here the research clearly established the following. (1) UXO forward scattered echo levels remain higher than typical backscattered levels for all source-to-target aspect angles. (2) Unlike backscattering, forward scattering remains strong for typical UXO targets as the target becomes buried in the sediment. (3) A properly designed wave-number filter can be used to extract the forward echo from the overlapping and much stronger incident source signal. Some effort was expended addressing in a preliminary fashion issues associated with the *short-range, down-looking case,* and the following results were achieved. (1) A strategy was developed for processing the acoustic color feature space associated with this 2-D measurement plane. (2) 2-D echo data bases were collected on a UXO target and two false targets buried 10 cm beneath the sediment surface. Preliminary RVM identification algorithms, trained on this data base as well as on comparable data bases generated by a finite element-based structural acoustics model, demonstrated good target feature separation. And (3) simple time-based images were successfully generated on the measured data and exhibited some promise for image based data calls.

Benefits

The structural acoustic approach to target detection and identification offers significant advantages over more conventional acoustic approaches which rely only on the formation of high resolution images. These advantages include: diverse set of "fingerprints" leading to low false alarm rates; longer range operation leading to wide area coverage; and low frequency sediment penetration leading to buried target prosecution.

1

OBJECTIVE

The objective for SERDP Project MR-1513 was to address the technical issues necessary to implement an innovative structural-acoustics (non–imaging) sonar system for wide search area identification using structural acoustic features from proud and buried UXO objects. In addition to providing wide-area capability, the structural-acoustic features may be integrated with other SERDP near-range sensors, including magnetometer, induction, and acoustic-imaging devices to increase identification performance. In contrast to imaging, the structural-acoustic technique exploits both non-specular and specular scattering features. This represents a new approach to acoustic identification of UXO; and we believe a number of exploitable structural-acoustic mechanisms exist for the in-water UXO problem and that the features derived therefrom will be sufficiently separable from individual classes of UXO and from those associated with clutter. Further, some of the features should manifest themselves at frequencies where significant bottom penetration persists, allowing detection and identification of buried UXO even at long ranges due to evanescent wave penetration.

The broad objective stated above can be broken into three objectives. The first is to understand the UXO target and clutter structural acoustic scattering signature phenomenology and the environmental impact on those signatures by performing controlled, high fidelity acoustic scattering and propagation measurements in the laboratory and at sea. Understanding the scattering phenomenology and the environmental impact on the signatures is the key to generating features that provide robust target identification. The first part of this objective was met in the first year of the program through laboratory measurements on target set 1 and extended to target set 2 in the second year, while the second environmentally-related goal was achieved in the latter years of the program. The second objective is to extract structural–acoustic features from scattered echoes collected both in the laboratory and at sea and to demonstrate that UXO and clutter can be separated via kernel–based identification algorithms exploiting these features. This objective was met in the second year as it relates to laboratory data and, to some extent, in the out years regarding at-sea data. The third objective is to apply site–specific active–learning paradigms developed under previous SERDP support and determine the bounds on performance of system concepts based on structural acoustic ID. This final objective was only partially addressed in this program.

BACKGROUND

Many active and former military installations have ordnance ranges and training areas with adjacent water environments in which unexploded ordnance (UXO) now exists due to wartime activities, dumping, and accidents. These contaminated areas include coastal and inland waters both in the United States and abroad. SERDP goals require the development of innovative technologies able to separate UXO from false targets and to discriminate amongst individual UXO targets themselves. Over time, such geographic areas are becoming less and less remote as the adjacent lands become further developed, and the potential hazard to the public from encounters with such UXO has begun to rise. Presently there exists no sufficiently effective capability to survey such underwater areas and map UXO locations.

This project (SERDP Project MR-1513) explored the potential for developing a structural acoustics (SA) based sonar methodology[1] for wide area search and identification of underwater unexploded ordnance (UXO). This new approach may have significant advantages over more conventional acoustic approaches which rely on the formation of high resolution images. These advantages include: diverse set of "fingerprints" leading to low false alarm rates; longer range operation leading to wide area coverage; and low frequency sediment penetration leading to buried target prosecution[2]

Conventional sonar approaches which form images (see Fig. 1) must operate at relatively high frequencies since the image resolution size is directly proportional to the acoustic wavelength. In this regime, acoustic wavelengths are short compared to the target dimensions and the waves are scattered for the most part from the external boundary of the target (specular scattering). In contrast, in the structural acoustic regime, acoustic wavelengths are comparable to, or longer than, the target dimensions. Sound readily penetrates the target, and the acoustic scattering is now related to the vibrational dynamics of the object, both whole-body and internal structure. The time-frequency features[3,4] in the scattered echoes can then be used to "fingerprint" the target without the need to form an image.

Acoustic Imaging Regime

$\lambda \ll d$

Acoustic scattering "specular" in nature used to form image of the external shape of the target of interest.

Structural Acoustic Regime

$\lambda \lesssim d$

Acoustic scattering related to vibrational dynamics of the object, both whole-body and internal structure. Resulting time-frequency features used to "fingerprint" target.
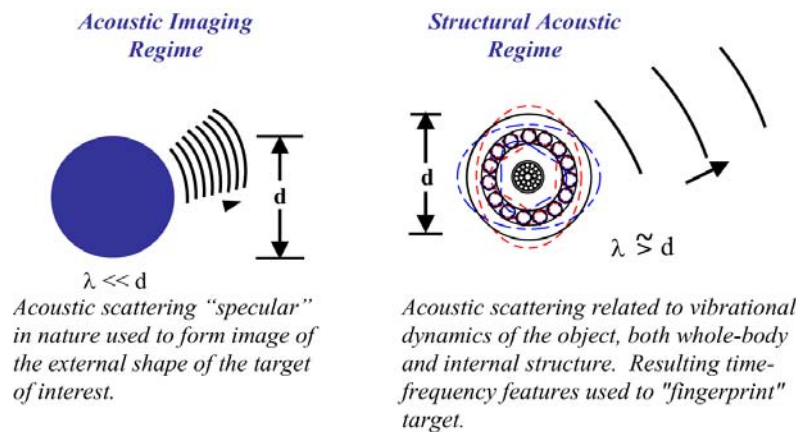
Figure 1 – Structural Acoustic ID vs. Imaging

MATERIALS AND METHODS

The program addressed three fundamental questions about UXO structural acoustic scattering phenomenology in a marine environment. 1) Does enough acoustic energy reach proud/buried UXO to produce a detectable and exploitable scattered signal at reasonable ranges? 2) Are the structural-acoustics signatures from underwater UXO and clutter sufficiently separable in a marine environment? 3) Can we structure identification algorithms so as to be robust with respect to the environmental and historical circumstances? We believe these questions were answered in the affirmative and thus provide the foundation for a new structural acoustics-based approach for identifying proud and buried UXO objects. The four main tasks included: 1) experimental measurements of the structural acoustic UXO and false target responses; 2) demonstration of the separability of UXO and false targets using structural acoustic features; 3) the development of a robust, concept drift active learning identification algorithm which could exploit the structural acoustic features regardless of the environment or historical conditions; and 4) prosecution of a test program both in the laboratory free-field and sediment facilities and in the waters off Panama City Florida for the purpose of more fully characterizing

targets and clutter *as they would present themselves in real-world environments.* The focus of the effort was to understand what features are important for determining whether detections *in a real-world environment* are or are not associated with UXO. Understanding the basic underwater scattering phenomenology for UXO and clutter in the structural acoustics band and then determining the environmental impact on the scattering phenomenology is the key to generating features that will provide robust target detection and identification in the real-world applications of this technology.

A core element of the project was a comprehensive examination of the scattering levels and features exhibited by typical UXO targets in the SA regime using NRL's state-of-the-art underwater scattering facilities, both laboratory-based[5] and sea-based[6]. In the first year, a representative UXO target set (target set 1) was identified, and the specific targets were obtained from the Aberdeen Proving Grounds. This four target set included a 155 mm artillery shell, a 5 inch rocket warhead, an 80 mm mortar round, and a 120 mm mortar round. Each target was then filled with a material system designed by NRL to roughly approximate the elastic moduli and density of a generic explosive. In the second year, additional targets were added to this UXO list. These included a 105 mm SABOT HEAT projectile, a water-flooded 120 mm mortar round, a 25 mm M794 dummy cartridge whose cavity is filled with an epoxy resin to approximate the weight of service cartridges, and two so-called overlap targets to be used in comparisons of the measurements made at NRL to those made at the Coastal Systems Station Laboratory (CSS) in Panama City Florida and to also serve as false targets. The overlap targets were two different size concrete-filled metal pipes. In addition to the UXO targets, a large rock and a common cinder block were used to represent examples of potential false targets. Systematic acoustic scattering measurements were carried out in the NRL Laboratory for Structural Acoustics Facility yielding full 360 degree broadband (1 kHz - 140 kHz) data bases. These measurements were completed on target set 1 in 2006; in 2007, the broadband measurements were completed on the 105 mm SABOT HEAT projectile, the 25 mm solid dummy round, the two overlap targets, and the large rock and the common cinder block false targets. These measurements made in the free-field were augmented by those made on some of the targets in the proud and partially buried conditions using a laboratory-based sediment scattering facility and an at-sea rail-based system.

Figure 2 – NRL Laboratory for Structural Acoustics.
One million gallon pool facility with adiabatic walls and acoustic coatings, vibration isolation system, and complex acoustic scanners, sources, and processing algorithms.

The Laboratory for Structural Acoustics (LSA)[5] at NRL (see Fig. 2) is a state-of-the-art

underwater acoustic research laboratory unique in the world. The LSA infrastructure includes a large cylindrical one million gallon (17 m diameter x 15 m deep) de-ionized water tank located in Building 5. This tank is vibration isolated, temperature controlled, and heavily instrumented with in-water precision robots for nearfield acoustic holography (NAH), laser Doppler vibrometry (LDV), and compact range measurements.

The free-field scattering measurements reported here were conducted with the facility in its compact scattering range mode as shown in Fig. 3. Each UXO target was suspended at mid-depth in the tank together with the source and receiver. Two sources were used for these experiments. The first source is a 3 meter long nearfield line array mounted horizontally. The array elements are shaded in such a way as to produce a plane-wave sound field in its nearfield throughout a limited volume centered at the target position. The line array generates a broadband pulse approximately 1 ms in duration which covers the band from 1 – 25 kHz. The
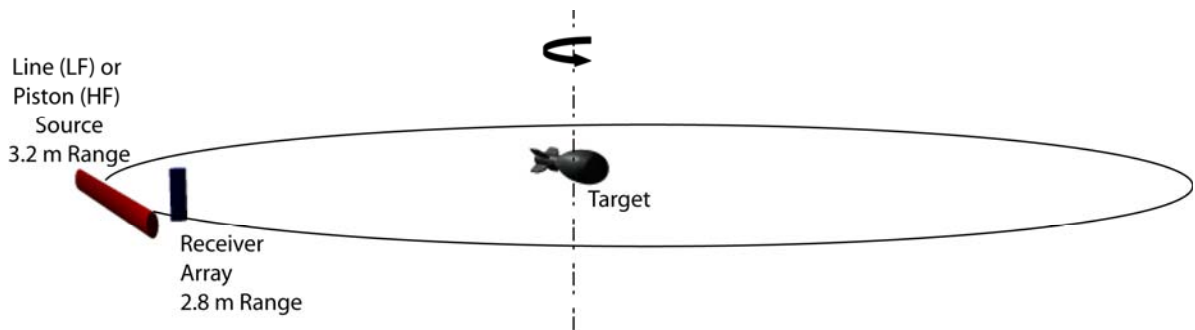
Figure 3 – Experimental Measurement Geometry
The target is placed in the plane-wave region of (1) a nearfield cylindrical source at low frequency (LF) or (2) a farfield piston source at high frequency (HF) with a nearly co-located broadband short vertical receiver array. The target (which is ~ 2.7 m from the receiver) is rotated over a full 360 degrees in increments of 1 degree.

receiver used in these experiments is a vertical line array that was also suspended at the mid-depth of the tank. A second piston-like source was used to collect data in the band from 8 kHz – 140 kHz. The measurement system is designed for collection of both monostatic and bistatic scattering data. However, for the free-field measurements reported here, only the monostatic configuration was used, i.e. the source and receiver fall along the same bisector to the target center. The scattered echo response was measured 2.7 meters from the target in 1 degree increments over 360 degrees. The data was processed to recover full complex scattering cross-sections expressible as target strength referenced to 1 meter in the following way. In order to obtain the target strength, three quantities are measured: the incident acoustic pressure, the pool clutter (background) pressure, and the scattered pressure. First, the source is excited and the incident pressure measured at the location corresponding to the target center for the scattering measurement. Second the source is excited and the clutter pressure field measured at the location at which the receiver will be placed for the scattering experiment. Lastly, the target is inserted and the scattered pressure field measured.

In this method, the time domain scattered data from the target at a given aspect angle is cleaned to remove unwanted reflections (clutter) not associated with a target return, Fourier transformed, and then normalized by a reference measurement. The target strength is obtained

by first subtracting the clutter measurement from the scattering measurement. This process removes energy from any indirect paths due to reflections from the finite-size pool boundaries or submerged equipment. This step is only possible through precise control of the locations of the acoustic elements and only if fluctuations in the acoustic medium with time are sufficiently small. For our facility (which meets these demands), robotic control of the source and receiver position is approximately 30 microns, and the iso-velocity water is maintained to within 0.01° C for more than a 24 hour period. With the clutter removed from the scattered signal, the parameter $X(f,\theta)$ is formed in terms of the scattered signal, $P_{scat}(f,\theta)$, and the incident field measured at the target center, $P_{inc}(f)$:

$$X(f,\theta) = \frac{P_{scat}(f,\theta)}{P_{inc}(f)} \frac{r_{scat}}{e^{ikr_{scat}}},$$ (1)

where r_{scat} is the distance from the target center to the receiver. The target strength (TS) is then defined and displayed as $10\log_{10}\left(|X(f,\theta)|^2\right)$.

The basic data acquisition parameters are summarized as follows: overall bandwidth 1 kHz – 140 kHz; sample rate (per channel) 500 kHz (min.); record length (per channel) ~32 k; record length (time) 16 ms; ensemble number ~16; dynamic range ~ 80 dB; and typical measurement duration ~1 week.

In some cases, it is anticipated that structural acoustic features could be integrated with responses from existing SERDP near-range sensors such as induction detectors in order to further increase identification performance. To permit evaluation of this possibility at a later time, inductive measurements were also carried out using a Geonics Limited EM61-MK2 submersible sensor system, a high powered time domain pulsed-induction device suitable for detecting both ferrous and non-ferrous metals. Metallic objects interact with the transmitted field inducing secondary fields which are subsequently detected by coils co-located with the transmitter. The data was collected on a battery operated data acquisition system which was also provided by Geonics and down-loaded to a PC. In these measurements, the 155mm artillery shell target filled with the explosive simulant was hung with Kevlar fishing line (non-magnetic) in the NRL pool facility. The measurements, taken as ensemble data to be averaged off line, were monostatic covering angular aspects from 0 to 360 in increments of 15 degrees with a source/receiver to target center distance of 1.27m. The completed data base will be used at a future time to evaluate the merits associated with combining structural acoustic ID with this additional sensor modality.

In the second year, the target set 1 and target set 2 data bases were processed using feature extractors such as matching pursuits, and this led to a positive result for the first critical "go-no go" decision point in the second year. Kernel–based algorithms such as Relevance Vector Machines[7] (RVM) and Kernel Matching Pursuits[8] (KMP) which use the structural acoustic features for identification were demonstrated using the experimental data bases. Measurements in the sediment pool facility begun in the second year were continued into the third year. Also in the third year, targets were seeded in the maritime environment off the coast of Panama City, and acoustic scattering data were collected using an existing rail-based measurement system. In order to allow the structural acoustic identification algorithms to adapt to new site-specific details such as target type/orientation and environmental conditions, the

development of a concept drift active learning identification algorithm suitable for UXO was initiated in the second year. Research in the fourth and fifth year focused on the collection of laboratory-grade data sets regarding target burial and vertical orientation, the analysis of these data bases, and the determination of the impact of these effects on scattering and on the associated structural acoustic features. In addition to monostatics, other geometries were also addressed including bistatics, the special case of forward scattering, and some limited large angle look-down arrangements in the sediment pool facility. There was also collection of additional at-sea data bases in the structural acoustics frequency band at the Panama City off-shore site. The objective here was to more fully characterize targets and clutter *as they would present themselves in real-world environments,* to understand what features are important for determining whether detections in a real-world environment are or are not associated with a UXO and to demonstrate the feasibility of obtaining meaningful forward scatter target strength in a marine environment.

RESULTS AND DISCUSSION

MEASURED SCATTERING DATA

The measured data over the complete, composite band from 1 – 140 kHz are displayed in Figs. 4-13 as a function of frequency and target aspect for the six UXO targets, the two "false targets", and the concrete-filled pipes with the color scale mapping actual target strength levels.
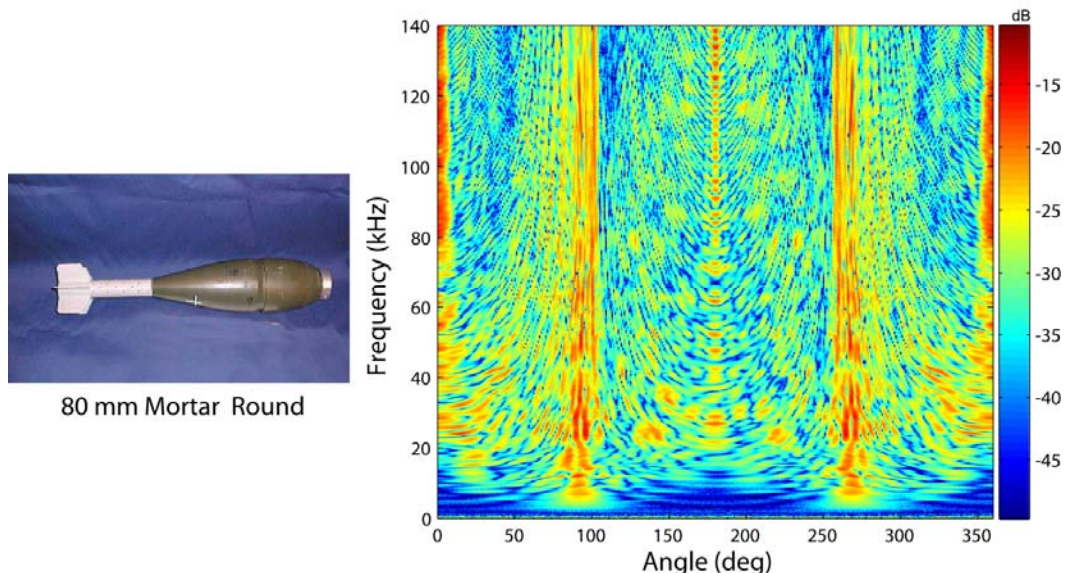
Figure 4 – Measured Target Strength & Target Photo
Magnitude of the target strength coded in color map versus frequency and target aspect for the 80 mm mortar round.

8
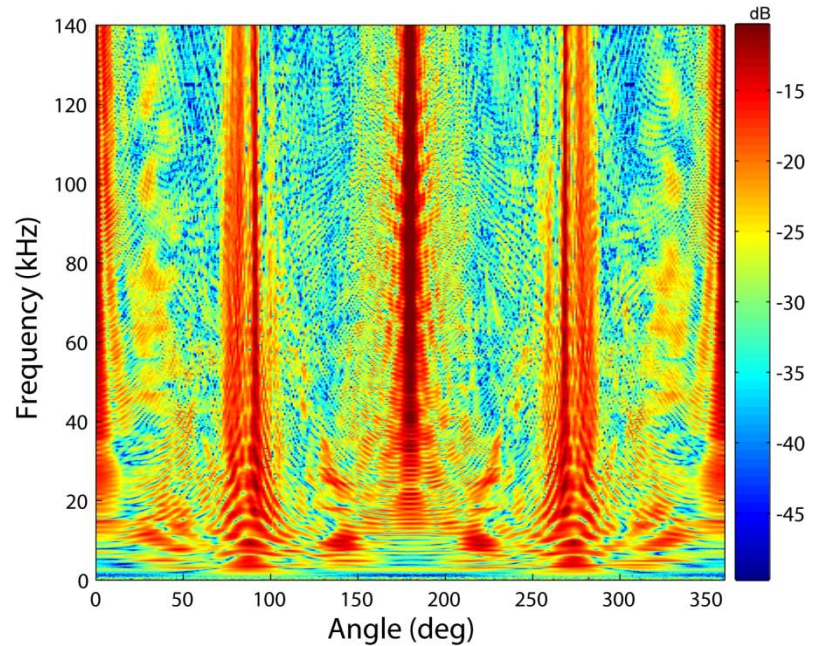
Figure 5 – Measured Target Strength & Target Photo.
Magnitude of the target strength coded in color map versus frequency and target aspect for the 155 mm artillery shell.
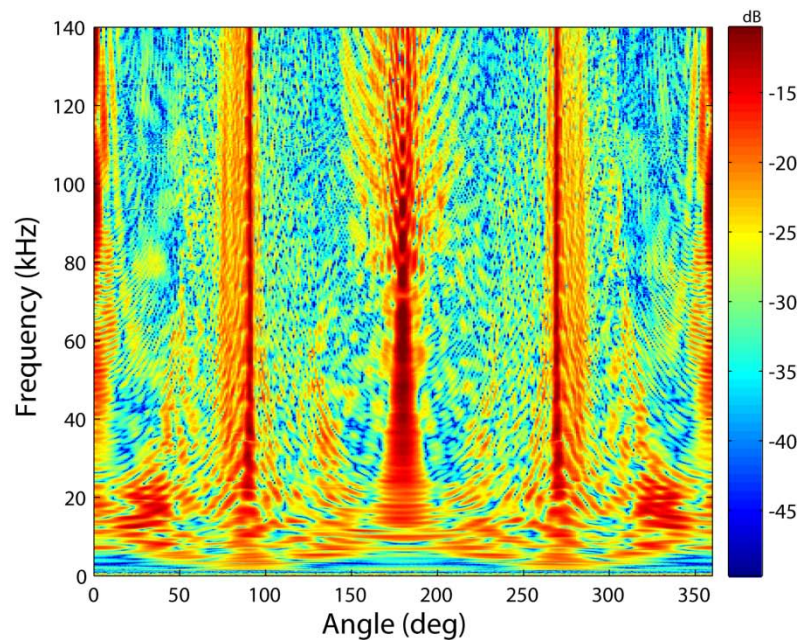
Figure 6 – Measured Target Strength & Target Photo.
Magnitude of the target strength coded in color map versus frequency and target aspect for the 5 inch rocket warhead.

Figure 7 – Measured Target Strength & Target Photo.
Magnitude of the target strength coded in color map versus frequency and target aspect for the 120 mm mortar round.
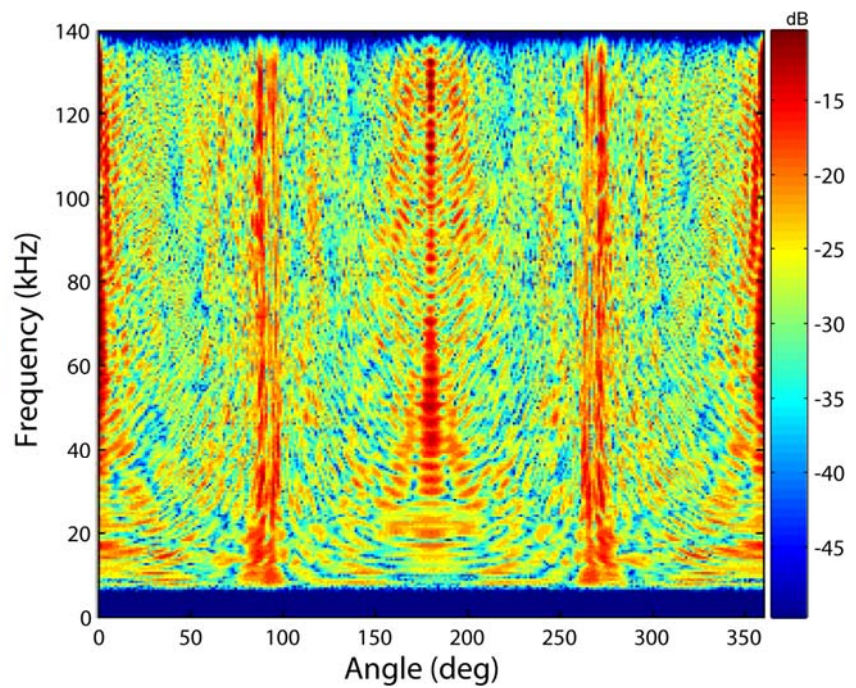
Figure 8 – Measured Target Strength & Target Photo.
Magnitude of the target strength coded in color map versus frequency and target aspect for the 105 mm SABOT round.

10
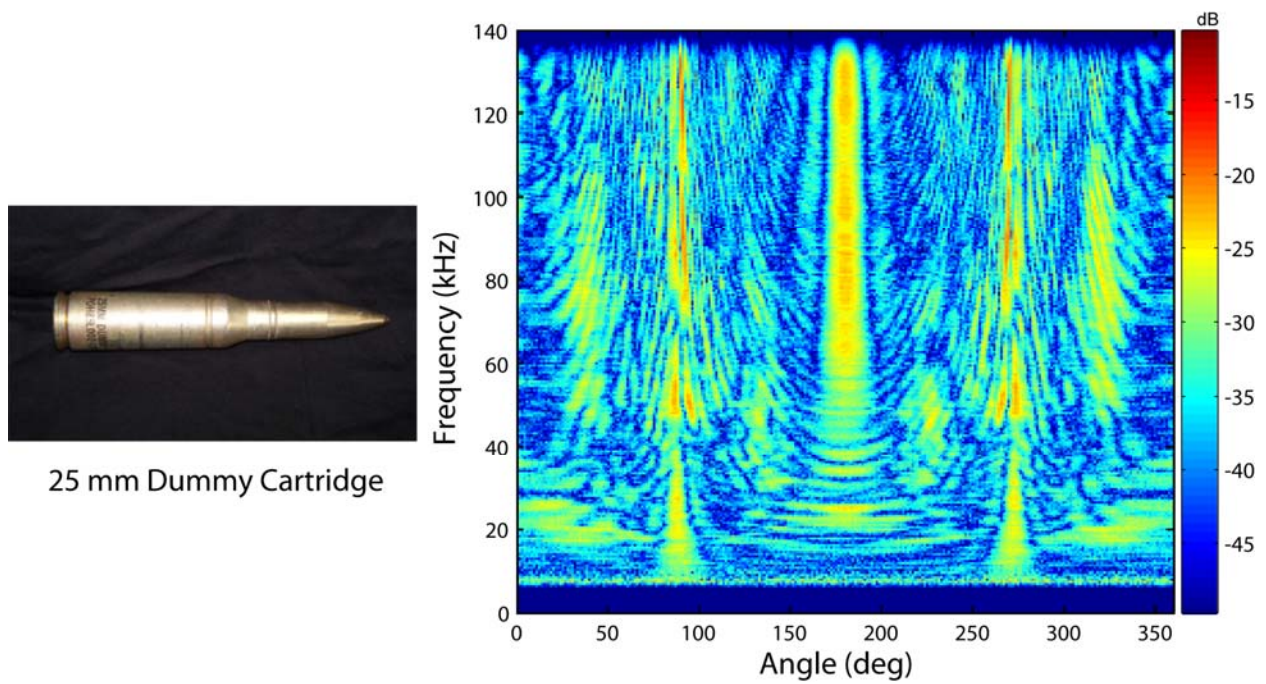
Figure 9 – Measured Target Strength & Target Photo.
Magnitude of the target strength coded in color map versus frequency and target aspect for the 25 mm cartridge round.
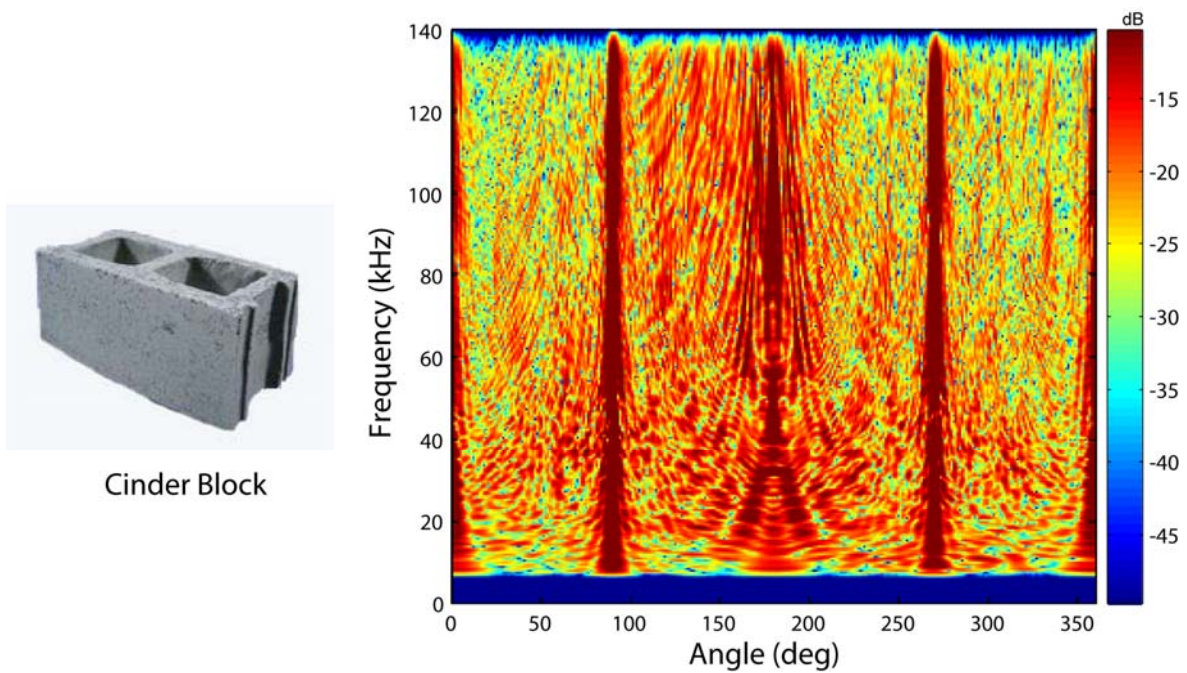
Figure 10 – Measured Target Strength & Target Photo.
Magnitude of the target strength coded in color map versus frequency and target aspect for the cinder block oriented in its normal construction orientation.

11
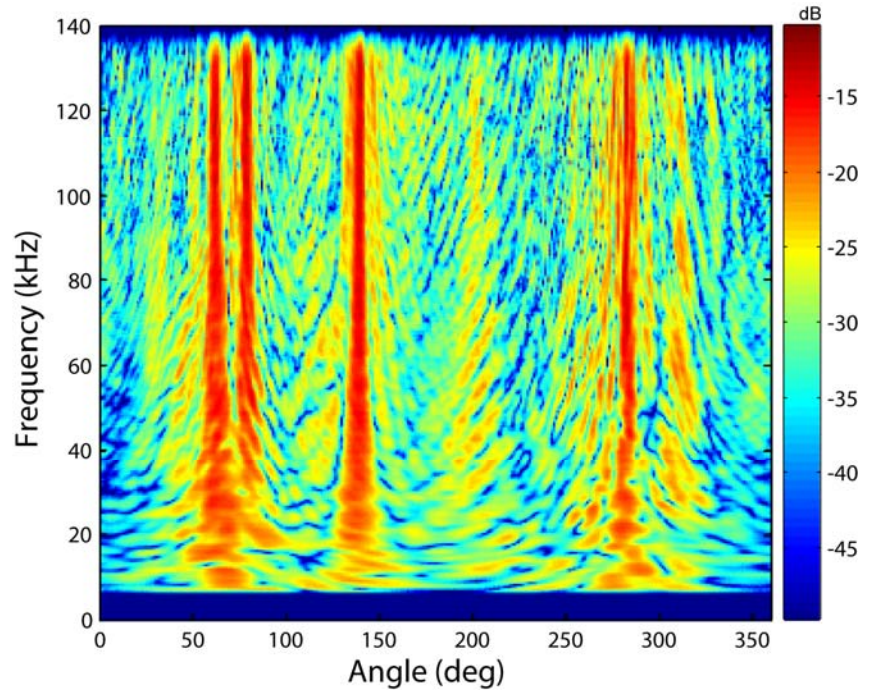
Figure 11 – Measured Target Strength & Target Photo.
Magnitude of the target strength coded in color map versus frequency and target aspect for the large rock.
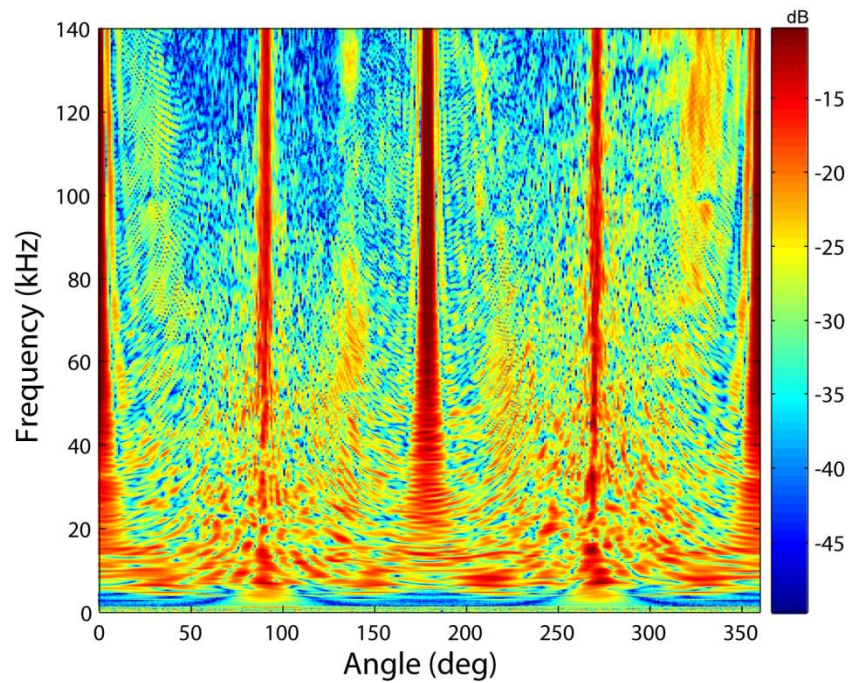
Figure 12 – Measured Target Strength & Target Photo.
Magnitude of the target strength coded in color map versus frequency and target aspect for the concrete-filled metal pipe #1.
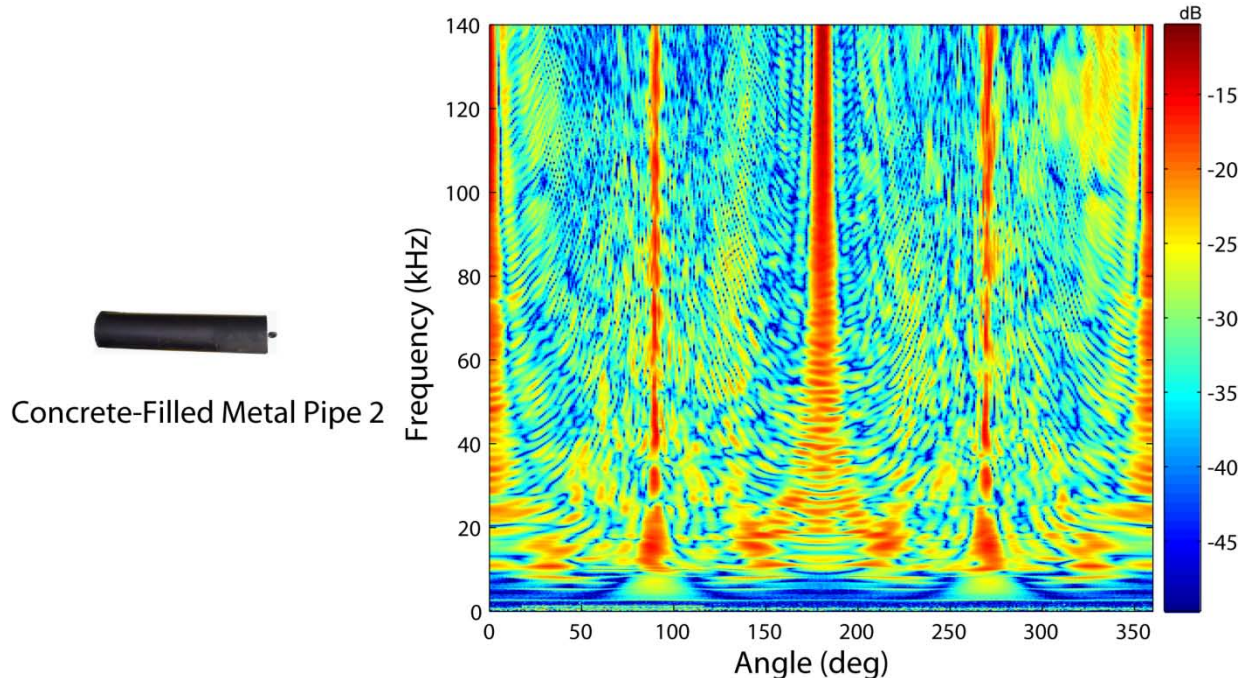
Figure 13 – Measured Target Strength & Target Photo.
Magnitude of the target strength coded in color map versus frequency and target aspect for the concrete-filled metal pipe #2.

UXO SCATTERING LEVELS

As can be seen, leaving aside for the moment the very small 25mm cartridge, the highest target strength level observed for each UXO target ranges from about -15 dB for the smallest target (80 mm mortar round) to > -10 dB for the largest (155 mm artillery shell). Taken as a set, at any particular aspect we can readily observe scattering features at some frequencies in the structural acoustic band with levels > -20dB. Based on our experience (and as we establish below), such levels should *generally* provide sufficient signal-to-noise for detection out to modest ranges (~100 meters).

In Fig. 14 we show the result of a simple estimate based on the sonar equation[10] of the maximum detection
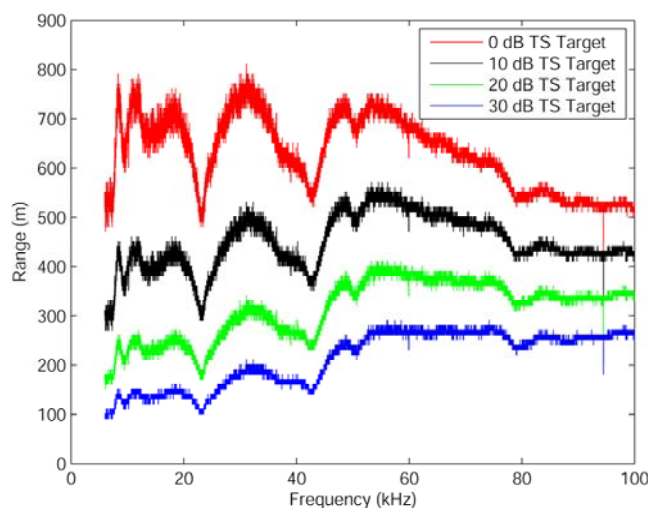
Figure 14 – Maximum Detection Range versus Frequency.
Maximum distance that a target could be detected (S/N = 1) for a medium without boundaries, noise spectral levels measured in the San Diego Harbor, and a source level of 170 dB re:µPa.

13

range for the following simple case. We assume a source level of 170dB re:μPa, a medium with no boundaries, two-way propagation loss based only on spherical spreading and a frequency dependent absorption[11], and a frequency dependent noise level derived from measurements in the San Diego harbor[12]. This frequency dependent, relatively high noise spectral level is about 60 dB re:μPa^2/Hz at 5 kHz falling non-monotonically to about 30 dB re:μPa^2/Hz at 100 kHz. The predicted range (defined by the range for which the S/N =1) is plotted versus frequency for 0 dB, -10 dB, -20 dB, and -30 dB targets. As can be seen, for these conditions the -20 dB target features would be detectable at the low end of the band (5 kHz) well beyond 100 meter ranges and at 20 kHz beyond 200 hundred meters. Further, -10 dB scattering levels would be detectable beyond even these ranges. Returning now to the very small 25 mm dummy cartridge (Fig. 9), we see that the maximum target strength levels are between about – 25 dB and – 30 dB in the band 15 kHz to 25 kHz. As can be seen from Fig.14, these levels are detectable out to 100 meter ranges. Considering that this target is about the smallest UXO size we would expect to encounter, we should be able to detect all UXO's out to 100 meter ranges. We have assumed in the estimate relatively low source levels so that reductions in detection range resulting from boundary effects not considered here should be able to be countered by increases in source level. We conclude that the features present in the structural acoustic band from UXO in general should be detectable out to ranges sufficiently long for the intended application viz. acoustic detection and identification of UXO objects in coastal and inland waters.

UXO SCATTERING MECHANISMS

Geometric (rigid) scattering[13] is that scattering which arises only from the acoustic impedance mismatch at the interface between the fluid and the target surface and which is caused by simple reflection. At high frequencies this scattering obeys the laws of geometric optics. The geometric response is important for two reasons. First, it provides a "floor" TS level whose angular highlight pattern can be simply inferred from the target's shape. Further, interference with any elastic scattering effects also taking place would produce TS decreases from this "floor" only over limited bandwidths if at all. Second, knowledge of the geometric response when compared to the actual measurements allows one to determine the degree of participation of elastic mechanisms in the scattering.

The casings of our targets are stiffer than the surrounding fluid so that we can obtain the geometric scattering by taking the target to be rigid. Accordingly, the rigid-body target strength was calculated for the precise shape of one of the targets, the 5 inch rocket, using a highly-parallelized finite element-based code[14] over as high a frequency band as was practical (up to 40 kHz). This in turn was determined by the largest grid resolution that could be run on our available parallel computing resource. The results are shown in a semi-log plot in Fig. 15 along with the measured result. In the following, we attempt to put this geometric scattering result into some perspective.
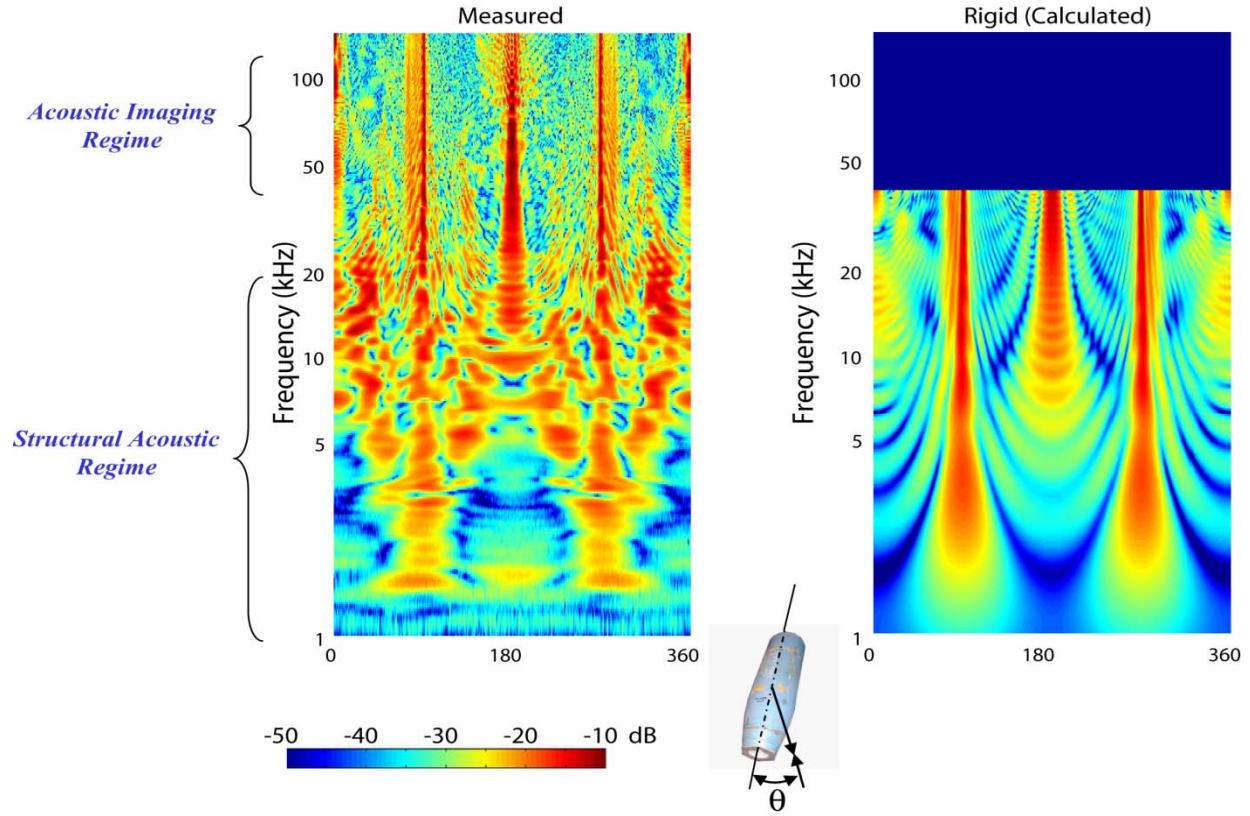
Figure 15 – Measured Target Strength & Calculated Rigid Response.
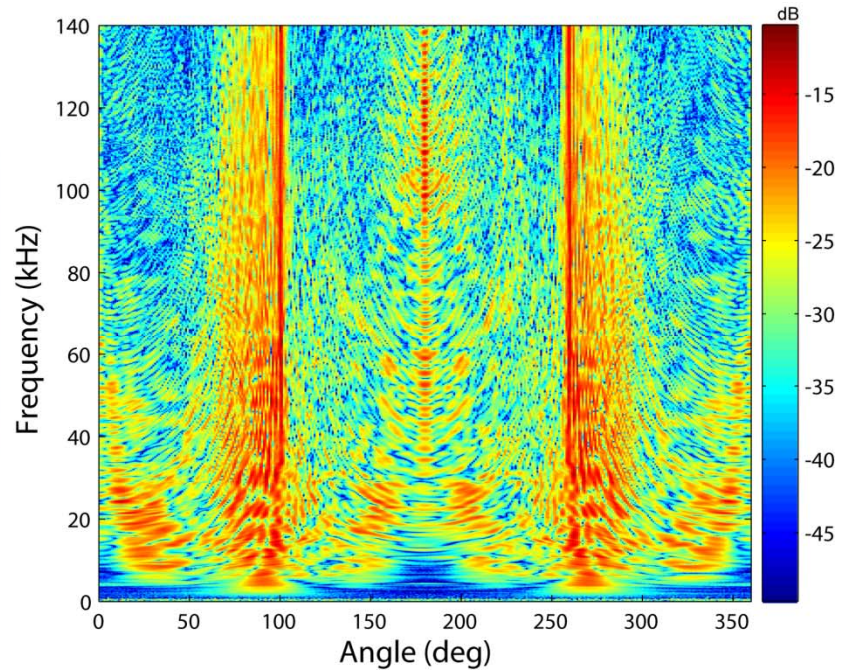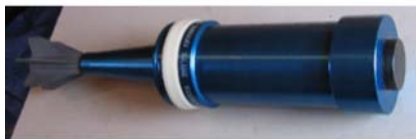*Semi-log plot of the magnitude of the target strength coded in color map versus frequency and target aspect for the 5 inch rocket. (Left: measured; right: rigid response computed using FE-based scattering code.)*

Beam Aspect TS for the 5 inch Rocket (and the 155 mm Shell)

If one approximates the lateral surface of both the 5 inch rocket and the 155mm shell as a finite circular cylinder, the beam aspect target strengths (TS) of these targets can then be estimated directly from simple expressions. In particular, the far field TS of a finite cylinder can be closely approximated[13,15,16] as:

$$TS = 10\log\left\{a\ell^2/2\lambda\right\} + 20\log\left|f_{\infty,}\right| \tag{2}$$

where "a" is the radius, "ℓ" is the length of the cylinder, "λ" is the wavelength of the incident sound, and "f_∞"is the form function. The first term of Eq. 2 represents the geometric response[13] of the target, which provides the TS floor. At beam aspect, this geometric floor provides most of the backscattered energy over most of the frequency band. Inserting the length and radius (maximum value) for the 5 inch rocket gives -13.6dB at 10 kHz, which is close to that computed for the actual shape using the finite element model (see Fig. 15). We also point out that the additional response at aspects just before beam seen in both the finite element and measured responses are the highlights from the tapered section.

15

Stern Aspect TS for the 5 inch Rocket (and 155mm Shell)

The stern of the 5 inch rocket (and the 155mm shell) ends in a circular disk shape that should lend itself to TS estimation by computing the response of a circular plate. For a rigid circular plate, the TS is given by[13]

$$TS = 20 \log(A/\lambda) + 20\log\{(2J_1(\beta)/\beta)\cos(\vartheta)\}, \tag{3}$$

where "A" is the area of the circular disk, "β" is $\{ka \sin(\vartheta)\}$ where "k" is $2\pi/\lambda$, "a" is the radius of the disk, and "ϑ" is the angle measured from the normal to the disk. At normal incidence the second term in Eq.3 is 0 dB. If we assume a frequency independent reflection coefficient of 0.7, the response of the plate at exactly stern incidence would be approximated by

$$TS = 20 \log(A/\lambda) + 20 \log (0.7). \tag{4}$$

For the size of the 5 inch rocket stern end, at 10 kHz this would predict a TS of about -21 dB which should then rise at the rate of 6 dB per octave (first term in Eq. 4) which is close to what is observed in the finite element calculation (Fig. 15).

Conical Response Prediction

The mortar rounds with their strong lateral curvature, sharp bow taper, and fin-like stern are targets for which no strong beam, stern, or bow responses are expected. There are however truncated conical portions of the target which should produce a modest TS near beam aspect. Considering the 120 mm round, the largest of these extends from the vicinity of the indentation (driving band), located near the center of the mortar shell, to the stern. This conical feature should produce a maximum backscattered response at 10° beyond beam aspect (100°). Observation of the measured scattering response for this target (see Fig. 7) clearly shows this feature as well as the lack of strong responses at bow and stern. As can be seen, the response at 100° is indeed larger than the response at beam aspect (90°) for this target, again indicating that geometric scattering from the cut-off cone portion is a dominant mechanism. The TS of a truncated, circular cone illuminated at normal incidence to its lateral surface is given by[17]
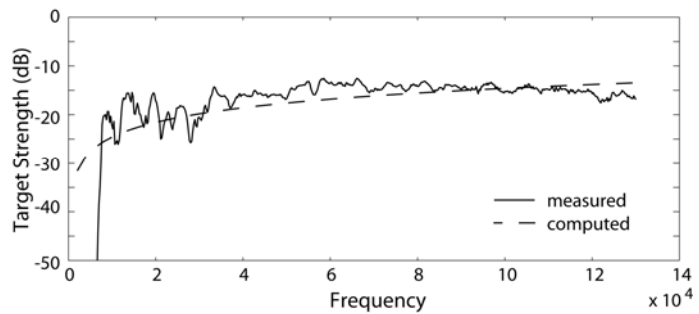
Figure 16 – TS (dB) at 100° versus Frequency for the 120mm Mortar Round.
Measured (solid) and as computed (dashed) using Eq 5.

$$10\log\left\{\left[\tfrac{2}{9}\lambda\right]\left[L_2^{3/2} - L_1^{3/2}\right]^2 [\sin(\alpha)\cos^4(\alpha)]\right\} \tag{5}$$

where L_2 is the length that the full cone would extend if continued to its pointed end, L_1 is the

length of the missing portion of the cone, and α is the half angle of the cone. Figure 16 compares the response of the 120 mm mortar round measured at 100° with the computation made from Eq. 5. Above 20 kHz, where the geometric response appears to be the dominant scattering mechanism, the conical approximation is generally within 5 dB of the measured response. Carrying out this analysis for the smaller mortar round produced similar results.

Elastic Response

We now return to the comparison in Fig.15 between the measured response versus the computed geometric result for the 5 inch rocket. The comparison clearly shows the impact of elastic effects on, and contributions to, the scattered response in the structural acoustic frequency domain. Notwithstanding these significant elastic effects, the imprint of the geometric response at beam and stern is still visible, although modulated in frequency through the interference of geometric and elastic responses. Even though limited resources prevented us from carrying out the rigid finite-element computations for the other targets, comparing the general character in the measured responses for these UXO targets in Figs. 4-9 and considering our discussion of the rigid responses based on the simple TS formulas, we can infer that the other targets have significant contributions from elastic mechanisms as well. In general, the elastic scattering could be related to a number of mechanisms which include shell dynamics, reflection and mode conversion of elastic shell-borne waves, air-cavity responses, penetration and re-radiation from the internal material, etc. Regarding the 25mm dummy cartridge, we also expect elastic responses related to shear and longitudinal elastic wave generation and propagation in the solid interior portion.

For all six UXO targets, we find evidence over broad aspects that at least some of the elastic energy involves scattering from the internal structure. To support this fact, in Fig. 17 we show a standard time/angle plot for the scattered echo from the 5 inch rocket along with an outline based on what we know about the target geometric details properly converted to travel time (using the sound speed in water). On this outline we have labeled the two loci of points on the target profile representing the minimum (A) and maximum (B) acoustic arrival times. At 0° aspect, (A) is associated with the target front and (B) with the target rear. In producing this result, we used a frequency domain filter to suppress the low and high end of the band where the signal-to-noise was low due to source level roll off. The associated impulse response of the filter was such that the ring down time for the return to drop at least 30dB is 0.1 msec. (One can see this ring-down artifact in Fig. 17 where there is some received signal level about 0.1msec before the minimum acoustic arrival time.) In the figure we can see resonant-like signals originating beyond the A contour and extending well beyond the contour labeled B. These are most likely due to elastic responses from the target interior from some of the mechanisms listed above. These responses are most visible in roughly 30° angular bands centered at 35° and 135° and the corresponding angles on the other side of the target. These internal scattering effects, whose specific source we have not yet identified, could be related to the dynamics of local as well as more global structural detail.
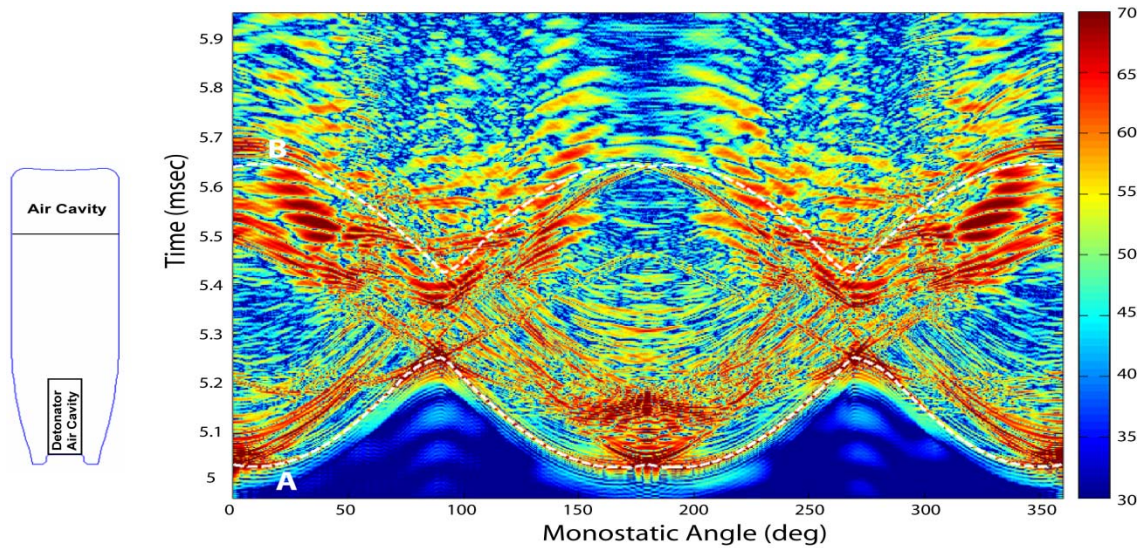
Figure 17 – Time-Angle Plots for the Scattering Returns from the Five Inch Rocket.
The contours labeled A and B represent the minimum and maximum acoustic arrival times, respectively. They are associated with the front (A) and back (B) of the target.

One possible explanation is related to phase matching of the water-borne acoustic wave at some angles to the interior waves. The longitudinal speed, C_L, is relatively low in the filler material, typically somewhere between 2000 m/s and 2900 m/s, and one could get phase matching for a waterborne wave incident at an angle θ from bow to a longitudinal wave in the filler traveling along the length of the somewhat cylindrical target. Phase matching would occur when $\lambda_{filler} = \lambda_{water} / \cos\theta$, or when $\theta = \theta_P = \cos^{-1} (C_{water}/C_{filler})$. The forcing pressure would have to work against the stiff casing (steel) material. If enough force could be transferred to the interior filler material, a longitudinal wave could be excited in the material which would travel down the cylinder. If it could reflect efficiently from the end, it would travel back and through the same phase-matching mechanism launch a backscattered echo. If the end conditions are right at front and back, we should see returns from this effect at θ_P, $180° \pm \theta_P$, and $360 - \theta_P$. The lowest value given above for the longitudinal speed in the filler (2000m/s) would give $\theta_P \sim 41°$ predicting returns at angles of 41°, 139°, 221°, and 319°. This is more or less what we see for the UXO except for the dummy cartridge where only the response at θ_P and $360° - \theta_P$ is observed. This, however, is consistent with the fact that the end condition for the interior elastic wave traveling from stern to bow does not look very conducive to a strong reflection.

SUMMARY OF UXO SCATTERING RETURNS

The scattering data of the six UXO targets can be seen to have both expected common features as well as those that are more target specific. The former include strong, narrow aspect, broadband signatures from the broadside (90 degrees) or near broadside of the target associated with specular reflection. Four of the targets also have similar strong returns from their backsides which present a nearly flat surface. This return is greatly diminished from the two mortar targets

18

because of their fin-like stern construction. Although there is a fin on the stern of the SABOT round as well, the rear of the body to which the long fin is attached also presents a large, flat reflector. All but the 120 mm mortar round present large specular returns from their more or less flat bow while the nearly tapered front of the latter precludes this effect. (The 80 mm mortar would also have very little bow return had we not replaced the missing detonator with a flat end piece.) In addition to these specular highlights, other features unique to each target can also be observed at various frequency-aspect locations. Examples here include the strong responses of the 155 mm artillery shell localized around 8 kHz and 145 degrees and a number of weaker localized responses from the 80 mm mortar round between 20 kHz and 40 kHz and for aspects from 145 degrees and 215 degrees. What appears to be a common feature is the strong response between 10 kHz and 20 kHz at aspects near $40°$, $140°$, $220°$, and $320°$ from the 5 inch rocket warhead, the 155 mm artillery shell, the SABOT round, the dummy cartridge, the 120 mm mortar, and to a lesser degree for the 80 mm mortar. We believe these responses are related to elastic wave phenomena within the interior of the targets. The returns from the more cylindrical targets (the 155 mm mortar round and the 5 inch rocket warhead) also exhibit the well known ring resonance structure at beam aspect (resulting from the interference of specular reflection and elastic circumferential wave re-radiation) an effect readily predicted for elastic cylinders.

Based on the observed structural acoustic scattering details and the above discussion, five of the UXO targets appear to break into two classes consistent with their rough shapes: Class (1) includes the five inch rocket warhead, the 155 mm shell, and the 105 mm SABOT round and Class (2) the two mortar rounds. Class (1) has a strong broadband highlight exactly at beam ($90°$) due to the cylindrical-like shape; this feature is scalloped with frequency due to the interference of radiation from circumferential elastic waves with the specular return. There is also a broadband return just below $90°$ from the shorter tapered side and a strong stern response from the flat end. The latter is also scalloped in frequency and spread in angle due to interference between it and a return from the air cavity/internal structure boundary. Finally, there is a low frequency response region centered roughly at quartering aspects associated with the internal structure.

Class (2) has no strong beam ($90°$) response; however, there are similar broadband highlights *near* beam from the two cone-like sections that make up the round. For the 120mm mortar, the scattering from the front and stern is low owing to the sharp taper (detonator) and fin-like structure, respectively. The modest return seen at bow in the 80mm mortar TS plot is actually an artifact due to our use of a flat disc to seal off and waterproof the device which was absent its sharp tapered detonator. As a class, we expect low bow and stern returns in general. As with Class 1, there also exists a modest response region at low frequencies roughly centered at quartering aspects associated with the internal structure.

Finally, we mention the sixth UXO target, the dummy cartridge. This target is in a class of its own. Its size is sufficiently small that only a few scattering highlights are clearly observable. These include the beam response, a lower return from the flat stern, and the return a low frequency response region centered roughly at quartering aspects associated with the internal structure. In addition, there are two lower level returns whose mechanisms are unknown at this time. They include resonance-like responses (narrow frequency band) around 5-6 kHz with broad angular lobes centered at bow, beam, and stern aspects and a response around 17 kHz near $135°$ and $225°$.

FALSE TARGETS AND CONCRETE-FILLED PIPES (OVERLAP TARGETS)

Regarding the measured scattering data from the "false targets", for the cinder block, the very strong specular returns from each of its four sides are to be expected from these large planar reflectors. (Note that in the measurements the block was placed horizontally.) The low frequency scattering levels for the large rock are asymmetric with respect to aspect as expected given its irregular shape.

Finally, the low frequency responses for the two concrete-filled pipes can be seen to have noticeable differences from the UXO targets in part owing to the significant differences between their filler materials and to their regular cylindrical shape.

POTENTIAL FOR FEATURE-BASED TARGET IDENTIFICATION

We address next the question as to whether the observed scattering returns would lend themselves to feature-based target identification. Runkle et. al[4] considered the scattering from a set of five similarly sized, submerged cylindrical shell targets with identical shapes but differing internal structure. Those authors were able to train discrete hidden Markov models (HMM) on the measured shell scattering patterns, and the HMM's were subsequently shown to be very effective at identifying the individual shell target when presented with test data from a target randomly selected without knowing which target aspects were included in the data set. Even in cases with additive noise, the HMM algorithm provided robust identification performance despite the high degree of similarity in the scattered patterns among the five shell targets. Further, using these same data bases, Krishnapuram and Carin[18] achieved improved discrimination using a support vector machine (SVM) classifier. Dasgupta, et. al.[19] demonstrated *class-based* identification using measured data from both the same set of air-filled shells as in Ref. 4 and ellipsoidal shells of different sizes and different material properties for which a finite element-based structural acoustic code was used to generate the scattering data. We find that the *general* character, *gross* features, and echo levels observed in the frequency aspect-dependent UXO scattering patterns presented here are qualitatively similar to the scattering reported from the shells in all the cases referenced above. It is therefore reasonable to expect that similar results would be obtained for identification algorithms trained and tested on the UXO scattering returns measured here.

We also point out that even a cursory comparison of the UXO target data taken as a class to that of the two false targets (the rock and the cinder block) suggests that feature-based separation of the UXO from these types of false targets should be straightforward. Furthermore, an additional, gross feature discriminate might be the symmetry of the scattering patterns. Unlike many false targets, UXO tend to be symmetric bodies of revolution; and the resulting almost perfect right/left symmetry in the UXO scattering patterns should be directly exploitable for false target separation.

20

TARGET SEPARATION RESULTS

The next step in the project involved post processing of the measured data bases using the various identification algorithms. The post processing algorithms which had already been developed in other work include feature extractors such as Matching Pursuits[4] and identification algorithms such as Relevance Vector Machines (RVM)[7], Hidden Markov Models (HMM)[4] , and Kernal Matching Pursuits (KMP)[8].

We show below an example of the degree of target separation possible using even a simple feature set and a KMP algorithm. The feature set was taken to be the energy in each of thirty five equally-spaced sub-bands between 8 and 25 kHz with random noise added to the scattering data.

In Figs. 18 – 30 we show the degree to which various targets separate versus target aspect angle for various angular apertures. In particular, in Figs 18 – 23, the red curves represent the 155 mm shell, the 80mm mortar, the 5 inch rocket, the 120mm mortar, the 105mm SABOT, and the 25 mm dummy cartridge, respectively, and in each case the remaining five UXO represented by the green. For all targets, three different data sets were used for each target by adding three different noise realizations to each target data set. Thus each of these results depicts how a particular UXO separates from all the others.

Figures 24 – 29 depict how well each individual UXO target separates from the clutter which is taken to be the rock, the cinder block, and a background noise without a target. In this case, seven different noise realizations were used for each target. Here the red curves represent the 155 mm shell, the 80mm mortar, the 5 inch rocket, the 120 mm mortar, the 105 mm SABOT, and the 25 mm dummy cartridge, respectively, and in each case the three clutter targets are represented by the green curves.

Figure 18 – Probability for Correct Target Identification.
Red curves represent the 155mm shell UXO target and the green curves the five remaining UXO targets.
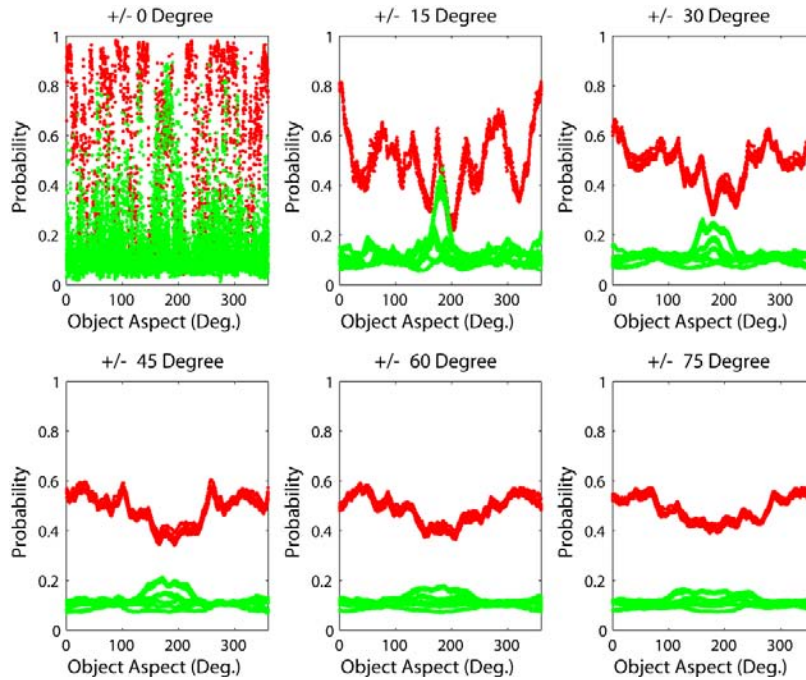
Figure 19 – Probability for Correct Target Identification.
Red curves represent the 80mm mortar UXO target and the green curves the five remaining UXO targets.

22
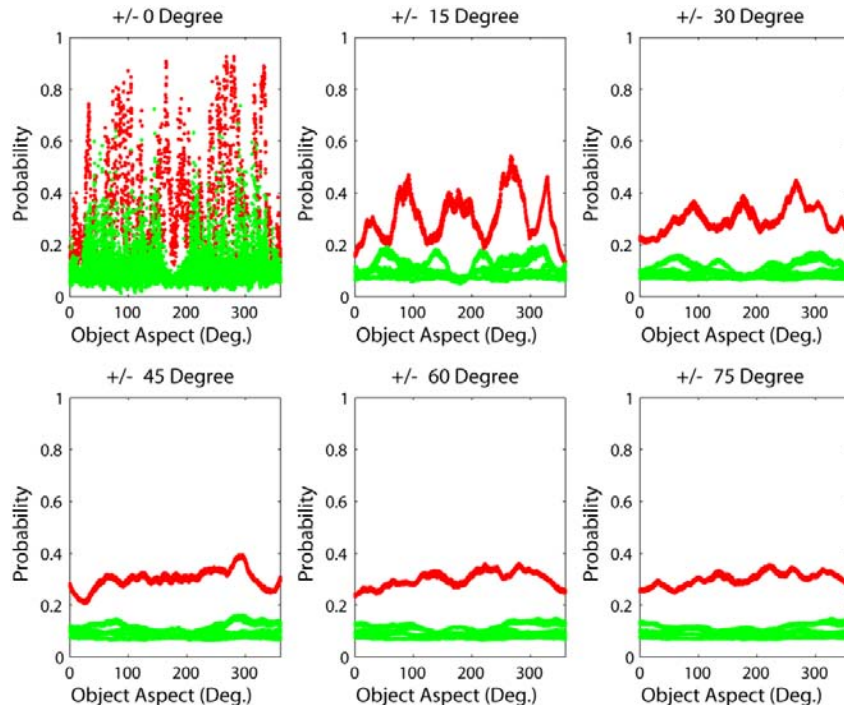
Figure 20 – Probability for Correct Target Identification.
Red curves represent the 5 inch rocket UXO target and the green curves the five remaining UXO targets.
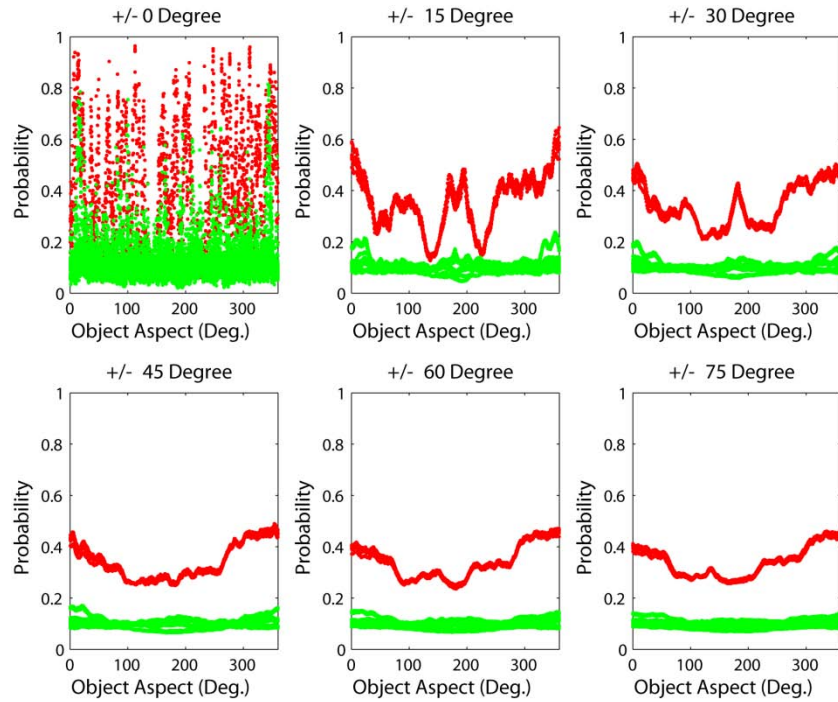
Figure 21 – Probability for Correct Target Identification.
Red curves represent the 120mm mortar UXO target and the green curves the five remaining UXO targets.
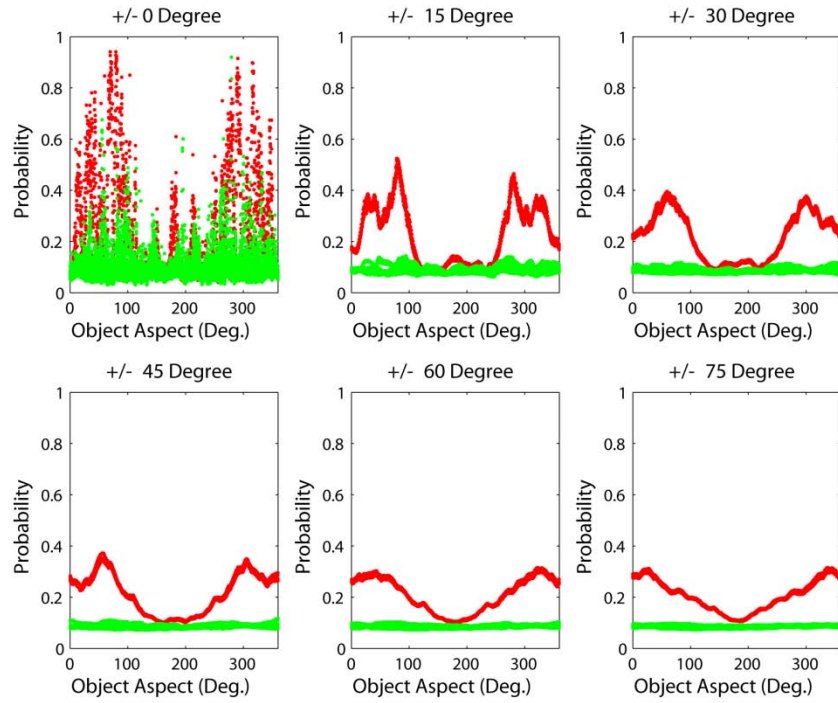
Figure 22 – Probability for Correct Target Identification.
Red curves represent the 105mm SABOT UXO target and the green curves the five remaining UXO targets.
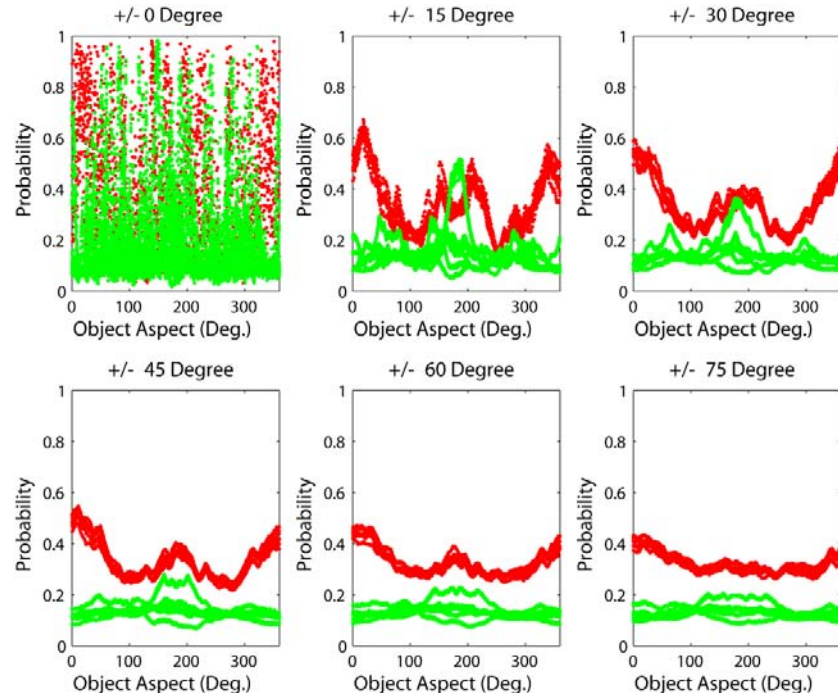
Figure 23 – Probability for Correct Target Identification.
Red curves represent the 25mm dummy cartridge UXO target and the green curves the five remaining UXO targets.
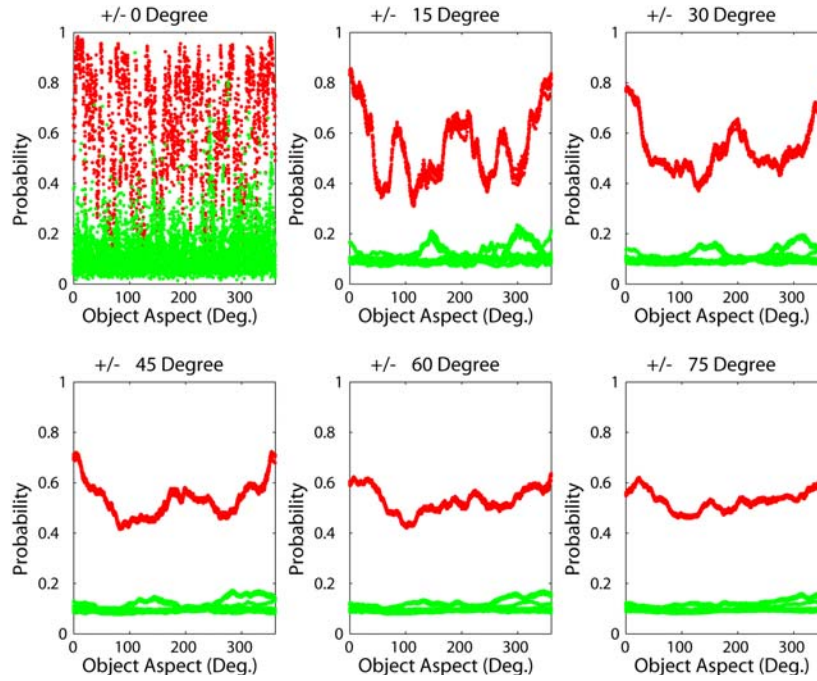
Figure 24 – Probability for Correct Target Identification.
Red curves represent the 155mm shell UXO target and the green curves the rock, cinder block, and background noise.
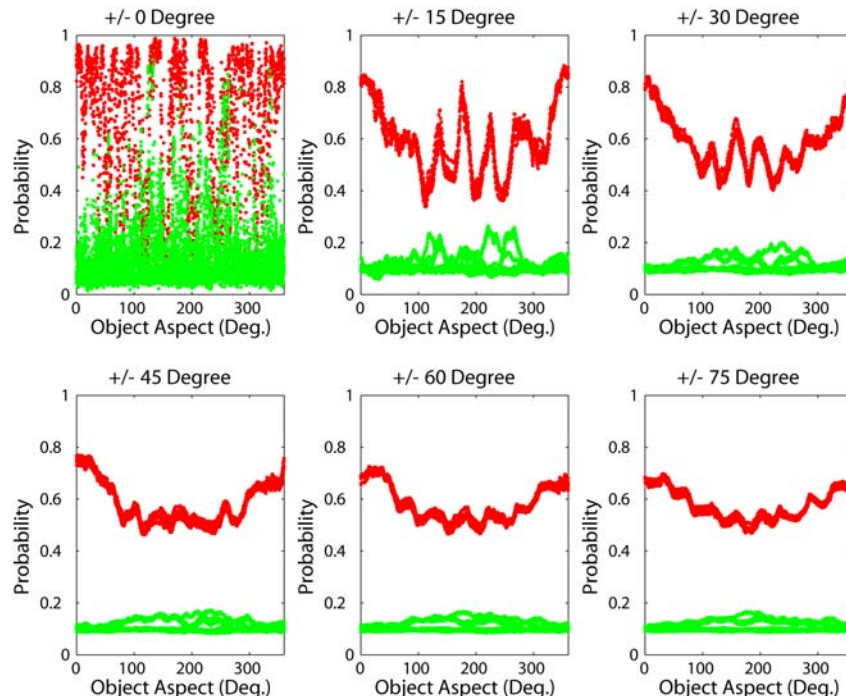
Figure 25 – Probability for Correct Target Identification.
Red curves represent the 80mm mortar UXO target and the green curves the rock, cinder block, and background noise.
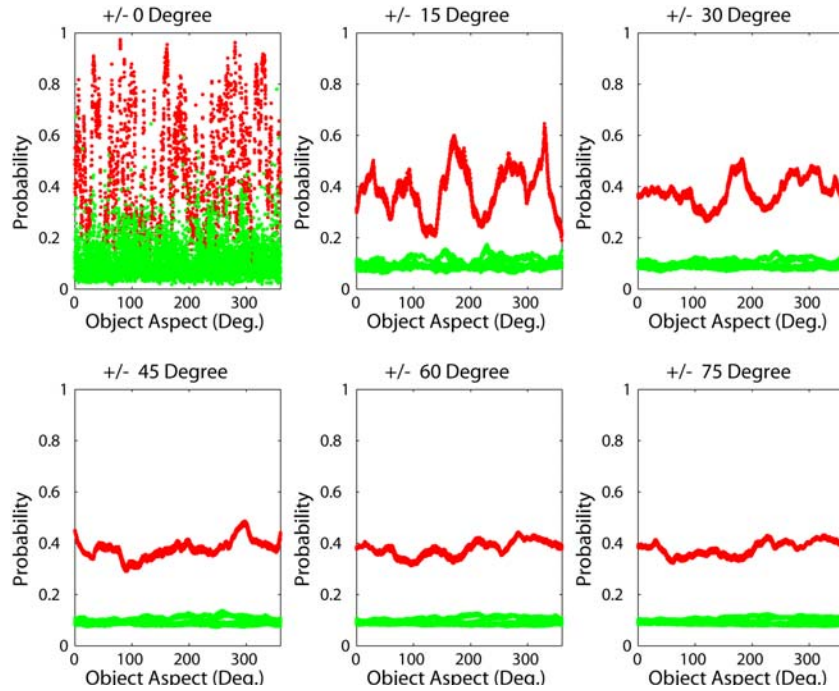
Figure 26 – Probability for Correct Target Identification.
Red curves represent the 5 inch rocket UXO target and the green curves the rock, cinder block, and background noise.
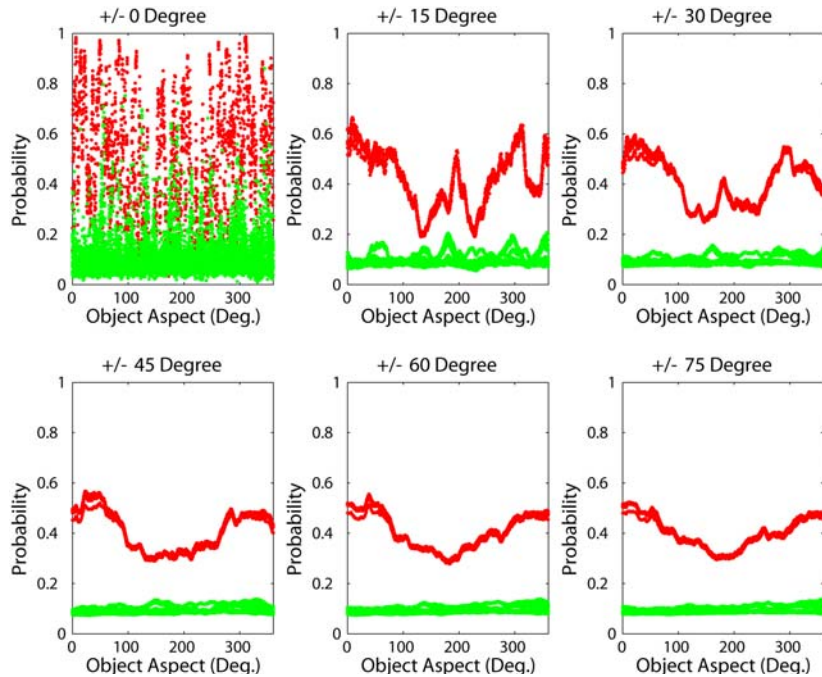
Figure 27 – Probability for Correct Target Identification.
Red curves represent the 120mm mortar UXO target and the green curves the rock, cinder block, and background noise.
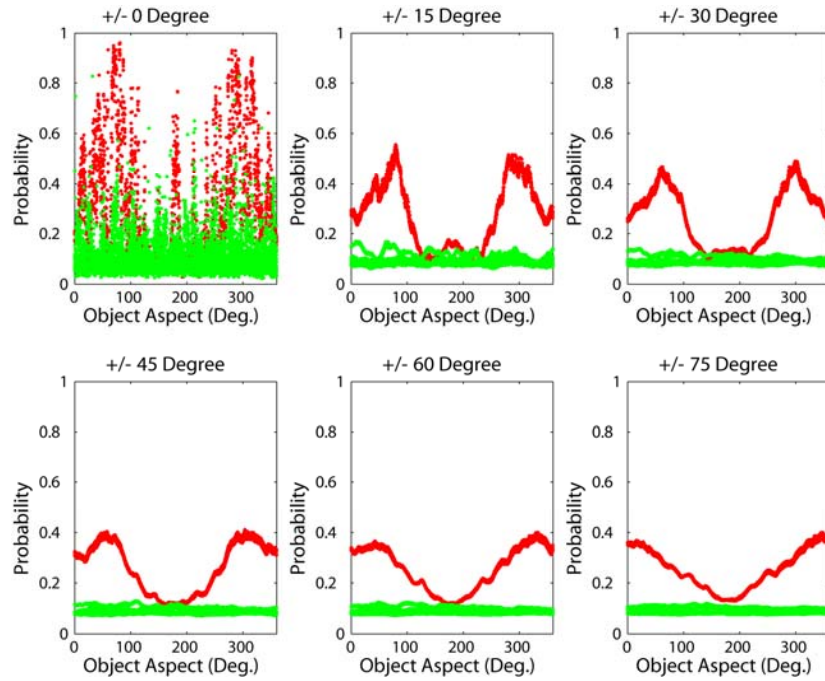
Figure 28 – Probability for Correct Target Identification.
Red curves represent the 105mm SABOT UXO target and the green curves the rock, cinder block, and background noise.
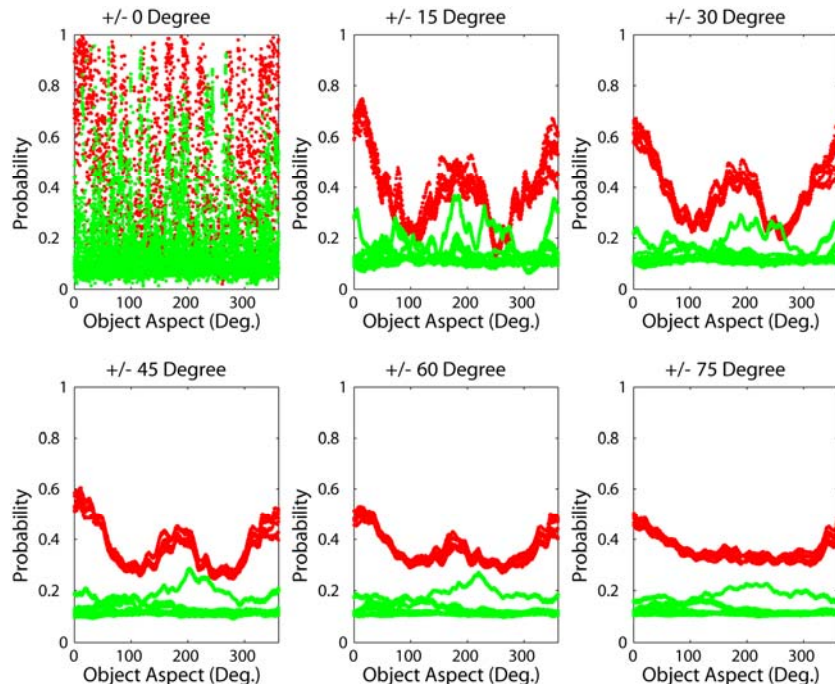
Figure 29 – Probability for Correct Target Identification.
Red curves represent the 25mm dummy cartridge UXO target and the green curves the rock, cinder block, and background noise.
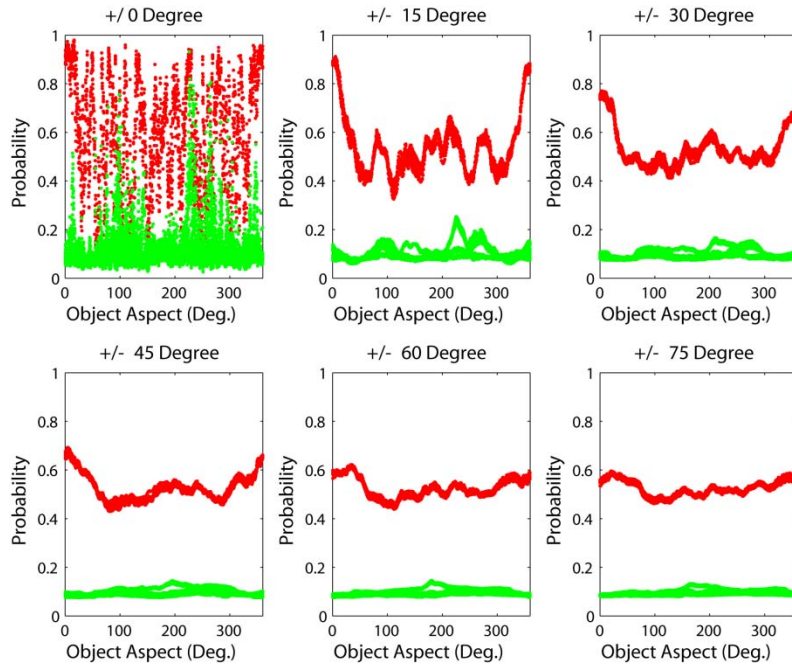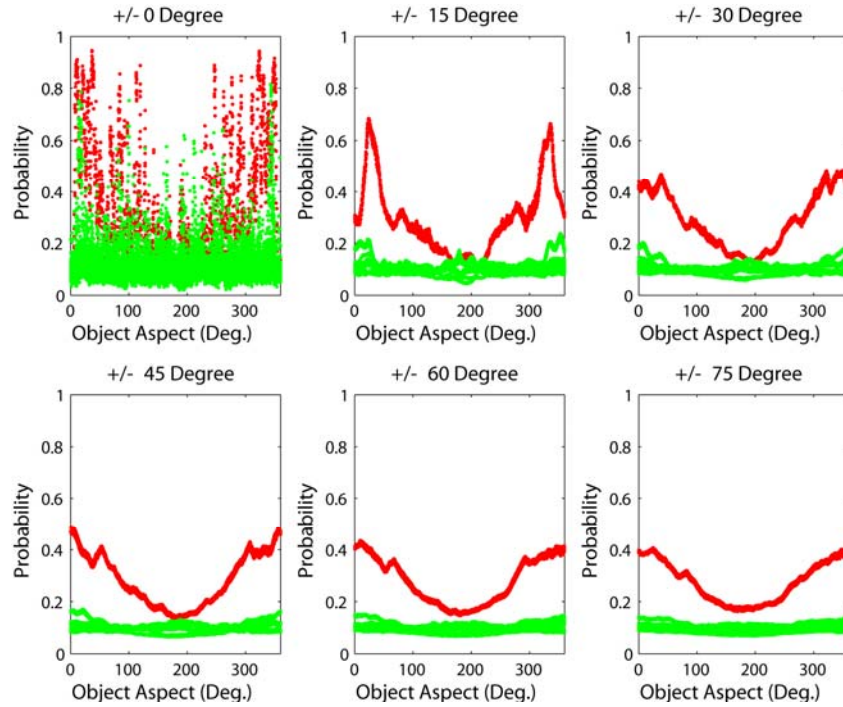
Figure 30 – Probability for Correct Target Identification.
Red curves represent the wet 120mm mortar UXO target and the green curves the five remaining UXO targets.

The above results clearly demonstrate our ability to separate UXO and false targets based on their structural acoustic features, at least as far as noise-corrupted free-field laboratory data is concerned. This represents a positive result for the first critical "go-no go" decision point of the program.

Finally, we discuss the last figure in this set which serves to present some indication regarding the robustness of the separation for this set of features. In the case of the 120mm mortar, scattering measurements were obtained for two conditions of the round, viz. wet and dry. The wet case corresponds to the situation in which water was allowed to penetrate the front end fusing compartment, not an extremely unlikely situation for a round immersed for a very long period of time. The results of the feature separation study are shown in Fig. 30 where we trained on the dry mortar round but tested with the wet round. This is to be compared to the dry case shown in Fig. 21. As can be seen, for the larger angular apertures, the results are roughly comparable suggesting that this feature set has some degree of robustness. For the narrower apertures there are some noticeable differences. These show up for the most part at stern aspects, which is somewhat curious in that the water penetrated into the front end.

CONCEPT-DRIFT ALGORITHM DEVELOPMENT

Background and Motivation

L. Carin at Duke University has been developing algorithms that infer inter-relationships between data collected at the current scene under test, and data collected at previous scenes. The algorithms are general, applicable to general sensor data, including acoustic-scattering data of interest for UXO detection. This class of algorithms is of particular interest here because of the fact that the acoustic signature from targets and clutter may be a relatively strong function of environmental factors, and therefore training (labeled) data from previous environments may or may not be relevant for the new scene under test. By inferring the inter-relationships between multiple data sets, the previous labeled data can be used appropriately.

The algorithms are based on the Dirichlet process, a hierarchical Bayesian algorithm. The Dirichlet process imposes the following prior on the model/algorithm: while it is possible that not all previous environments are relevant for the scene under test, it is likely that at least some are relevant. The Dirichlet process acts as a sieve to determine which previous data collections are relevant, and if none are relevant this is determined as well (in this latter case, for which no previous data are relevant, active learning is applied to acquire the set of labels required for learning). This overarching algorithmic approach is referred to as "life-long learning", because the algorithm makes inferences within the context of all data and experience collected over the "lifetime" of the sensor, and in this sense the algorithm is continually learning and inferring inter-relationships between previous experiences.

In UXO detection and identification, we are interested in the conditional distribution $p(y|\mathbf{x})$, where y is a binary variable indicating the presence or absence of UXO and $\mathbf{x}$ is a vector containing characteristic features of the items being interrogated. Normally we assume that the examples used to estimate $p(y|\mathbf{x})$ are *truly* drawn from $p(y|\mathbf{x})$, so that we can obtain an unbiased estimate based on the training examples. When training examples are drawn from a different distribution, say $q(y|\mathbf{x})$, we may end up with a biased estimate, which will then produce systematic errors even though the estimation is based on a large set of training examples.

A biased estimate of $p(y|\mathbf{x})$ can be a situation often encountered in UXO detection. One particularly common example results from the fact that the UXO signatures can be dependent on the sediment properties of the environment where they reside. UXO acoustic training data may come from measurements made in the NRL structural acoustic facilities, from areas off-shore where the appropriate measurement systems are available, or from former military training or weapons testing sites that have been cleaned. There is an issue as to whether such extant training data are relevant for a new site under current testing.

When the training data set and the test data set are collected under different environmental conditions, the two sets are characterized by different distributions. To make this point clear, let $p(\mathbf{x})$ and $p(y|\mathbf{x})$ denote the distributions governing the *test* examples, and $q(\mathbf{x})$ and $q(y|\mathbf{x})$ denote the distributions for the *training* examples. Unless the scattering features in the different environments do not exhibit significant variations, $p(y|\mathbf{x})p(\mathbf{x})$ and $q(y|\mathbf{x})q(\mathbf{x})$ cannot be

treated as identical; their difference must be taken into account when performing the estimation, in order to avoid biased estimate of p(y|**x**).

Within the maximum likelihood framework, the estimation of p(y|**x**) is based on maximization of the logarithmic likelihood function,

$$\ell(\mathbf{w}) = \frac{1}{N}\sum_{i=1}^{N}\log p(y_i \mid \mathbf{x}_i; \mathbf{w}), \quad \text{with } (\mathbf{x}_i, y_i) \overset{iid}{\sim} p(\mathbf{x})p(y \mid \mathbf{x}) \tag{6}$$

where **w** represents the parameters of p(y|**x**), and the training examples are truly drawn from the same distribution as test examples, with p(**x**) the distribution of test features. When training examples are drawn from a different distribution, say q(y|**x**)q(**x**), the logarithmic likelihood can be equivalently expressed as

$$\ell(\mathbf{w}) = \frac{1}{N}\sum_{i=1}^{N}\frac{p(\mathbf{x}_i)p(y_i \mid \mathbf{x}_i)}{q(\mathbf{x}_i)q(y_i \mid \mathbf{x}_i)}\log p(y_i \mid \mathbf{x}_i, \mathbf{w}), \quad \text{with } (\mathbf{x}_i, y_i) \overset{iid}{\sim} q(\mathbf{x})q(y \mid \mathbf{x}) \tag{7}$$

The equivalence between Eqs. (6) and (7) is based on the principle of importance sampling[20].

The major difficulty of applying Eq.(7) is that the importance weights $\dfrac{p(\mathbf{x}_i)p(y_i \mid \mathbf{x}_i)}{q(\mathbf{x}_i)q(y_i \mid \mathbf{x}_i)}$ are not available, since p(y|**x**)p(**x**) is unknown. Even though one may estimate p(**x**) from the test data, one cannot know p(y|**x**) because this is the very distribution we are trying to estimate.

Method and Technical Development

The method we employ here was first presented by Liao et al.[21], which solves the general problem of learning on examples from q(y|**x**)q(**x**) with the goal of generalizing to instances from p(y|**x**)p(**x**), assumed different from q(y|**x**)q(**x**). We consider the case in which we have a fully labeled auxiliary data set D^a and a partially labeled primary data set $D^p = D^p_l \cup D^p_u$, where D^p_l are labeled and D^p_u unlabeled. We assume that D^p are examples drawn from the primary (test) distribution p(y|**x**)p(**x**) (the one we are interested in) and D^a are examples drawn from the auxiliary (training) distribution q(y|**x**)q(**x**) (the one providing indirect and auxiliary information about p(y|**x**)p(**x**)). Our objective is to use a mixed training set $D^a \cup D^p_l$ to estimate the parameters **w** of p(y|**x**), which gives the classifier to predict the labels of D^p_u. We hope D^p_l is required to have a far smaller number of examples than that required when not using D^a.

As discussed earlier, when q(y|**x**)q(**x**) is significantly different from p(y|**x**)p(**x**), we must use Eq. (7) to seek the maximum likelihood estimate of **w**. To overcome the difficult of directly estimating the importance weights to correct the mismatch, we take an alternative approach. We introduce an auxiliary variable μ for each example in the auxiliary set D^a, to reflect its mismatch with D^p_l and to control its participation in the learning of **w**. The μ's play a similar role as the importance weights in Eq. (7). However, unlike the importance weights, the auxiliary variables

are estimated along with primary parameters **w** during the learning.

We assume D^p_l are fixed and nonempty and, without loss of generality, we assume D^p_l are always indexed prior to D^p_u, i.e., $D^p_l = \{\mathbf{x}^p_i, y^p_i\}^{N^p_l}_{i=1}$ and $D^p_u = \{\mathbf{x}^p_i, y^p_i\}^{N^p}_{i=N^p_l+1}$. We use N^a, N^p, and N^p_l to denote the size of D^a, D^p, and D^p_l, respectively. (Later, discuss how to actively determine D^p_l when D^p_l is initially empty.) We consider detection or binary classification and assume the labels y^a, $y^p \in \{-1,1\}$. For notational simplicity, we let **x** always include one as its first element to accommodate a bias (intercept) term, thus $\mathbf{x}^p, \mathbf{x}^a \in R^{d+1}$ where d is the number of features. For a primary data example $(\mathbf{x}^p_i, y^p_i) \in D^p_l$, we follow standard logistic regression[21] to write

$$p(y^p_i \mid \mathbf{x}^p_i; \mathbf{w}) = \sigma(y^p_i \mathbf{w}^T \mathbf{x}^p_i) \tag{8}$$

where

$$\sigma(\mu) = \frac{1}{1+\exp(-\mu)} \tag{9}$$

is the sigmoid function. For a auxiliary example $(\mathbf{x}^a_i, y^a_i) \in D^a$, we define

$$p(y^a_i \mid \mathbf{x}^a_i; \mathbf{w}, \mu_i) = \sigma(y^a_i \mathbf{w}^T \mathbf{x}^a_i + y^a_i \mu_i) \tag{10}$$

where μ_i is an auxiliary variable. Assuming the examples in D^p_l and D^a are drawn i.i.d., we have the log-likelihood function

$$\ell(\mathbf{w}, \boldsymbol{\mu}; D^a \cup D^p_l) = \sum_{i=1}^{N^p_l} \ln \sigma(y^p_i \mathbf{w}^T \mathbf{x}^p_i) + \sum_{i=1}^{N^a} \ln \sigma(y^a_i \mathbf{w}^T \mathbf{x}^a_i + y^a_i \mu_i) \tag{11}$$

where $\boldsymbol{\mu}$ collects all auxiliary variables.

The auxiliary variable μ_i is introduced to reflect the mismatch of $(\mathbf{x}^a_i, y^a_i) \in D^a$ with D^p_l and to control its participation in the learning of **w**. A larger $y_i \mu_i$ makes $p(y^a_i | \mathbf{x}^a_i, \mathbf{w}, \mu_i)$ less sensitive to **w**. Geometrically, the μ_i is an extra intercept term that is uniquely associated with $\mathbf{x}^a_i$ and causes it to migrate towards class y^a_i. If $(\mathbf{x}^a_i, y^a_i)$ is mismatched with the primary data D^p, **w** cannot make $\sum_{i=1}^{N^p_l} \ln \sigma(y^p_i \mathbf{w}^T \mathbf{x}^p_i)$ and $\ln \sigma(y^a_i \mathbf{w}^T \mathbf{x}^a_i)$ large at the same time. In this case $\mathbf{x}^a_i$ will be given an appropriate μ_i to allow it to migrate towards class y^a_i, so that **w** is less sensitive to $(\mathbf{x}^a_i, y^a_i)$ and can focus more on fitting D^p_l. Evidently, if the μ's are allowed to change freely, their influence will override that of **w** in fitting the auxiliary data D^a and then D^a will not participate in learning **w**. To prevent this from happening, we introduce constraints on μ_l and maximize the log-likelihood subject to the constraints:

$$\max_{\mathbf{w}, \boldsymbol{\mu}} \ell(\mathbf{w}, \boldsymbol{\mu}; D^a \cup D^p_l) \tag{12}$$

31

$$\text{subject to } \frac{1}{N^a}\sum_{i=1}^{N^a} y_i^a \mu_i \le C, \quad C \ge 0 \tag{13}$$

$$y_i^a \mu_i \ge 0, \qquad i = 1,2,\cdots N^a \tag{14}$$

where the inequalities in Eq. (14) reflect the fact that, in order for $\mathbf{x}^a_i$ to fit $y^a_i=1$ (or $y^a_i=-1$), we need to have $\mu_i >0$ (or $\mu_i <0$), if we want μ_i to exert a *positive* influence in the fitting process. Under the constraints in Eq. (14), a larger value of $y^a_i\mu_i$ represents a larger mismatch between $(\mathbf{x}^a_i,y^a_i)$ and D^p_l and accordingly makes $(\mathbf{x}^a_i,y^a_i)$ play a less important role in determining $\mathbf{w}$. The logistic regression classifier resulting from solving the problem in (7)-(9) is referred to as *migratory logistic regression* (MigLogit). The C in Eq. 13 reflects the average mismatch between D^a and D^p_l and controls the average participation of D^a in determining $\mathbf{w}$. The optimization in Eqs. (12)-(14) is a convex problem and the unique globally solution of $\mathbf{w}$ is guaranteed.

In the above discussion, we assumed that D^p_l had already been determined. We now describe how D^p_l can be actively selected from D^p, based on the Fisher information matrix. The approach is known as active learning. Let $\mathbf{Q}$ denote the Fisher information matrix of $D^a \cup D^p_l$ about $\mathbf{w}$. By definition of the Fisher information matrix[23], $\mathbf{Q} = E_{\{y_i^p\},\{y_i^a\}} \dfrac{\partial \ell}{\partial \mathbf{w}} \dfrac{\partial \ell}{\partial \mathbf{w}}^T$, and substituting Eq. (11) into this equation gives

$$\mathbf{Q} = \sum_{i=1}^{N_l^p} \sigma_i^p (1-\sigma_i^p) \mathbf{x}_i^p (\mathbf{x}_i^p)^T + \sum_{i=1}^{N^a} \sigma_i^a (1-\sigma_i^a) \mathbf{x}_i^a (\mathbf{x}_i^a)^T \tag{15}$$

where $\sigma_i^p = \sigma(y_i^p \mathbf{w}^T \mathbf{x}_i^p)$, $\sigma_i^a = \sigma(y_i^a \mathbf{w}^T \mathbf{x}_i^a + y_i^a \mu_i)$, and $\mathbf{w}$ and $\boldsymbol{\mu}$ represent the true classifier and auxiliary variables.

It is well known the inverse Fisher information $\mathbf{Q}^{-1}$ lower bounds the covariance matrix of the estimated $\mathbf{w}$. In particular, $\det(\mathbf{Q}^{-1})$ lower bound the variances of the elements in $\mathbf{w}$. The goal in selecting D^p_l is to reduce the variances, or uncertainty, of $\mathbf{w}$. Thus we seek the D^p_l that maximize $\det(\mathbf{Q})$.

The selection proceeds in a sequential manner. Initially $D^p_u = D^p$, D^p_l is empty, and $\mathbf{Q} = \sum_{i=1}^{N^a} \sigma_i^a (1-\sigma_i^a) \mathbf{x}_i^a (\mathbf{x}_i^a)^T$. Then one at a time, a data point $\mathbf{x}^p_i \in D^p_u$ is selected and moved from D^p_u to D^p_l. This causes $\mathbf{Q}$ to be updated as: $\mathbf{Q} := \mathbf{Q} + \sigma_i^p (1-\sigma_i^p) \mathbf{x}_i^p (\mathbf{x}_i^p)^T$. At each iteration, the selection is based on

$$\max_{\mathbf{x}_i^p \in D_u^p} \det[\mathbf{Q} + \sigma_i^p(1-\sigma_i^p)\mathbf{x}_i^p(\mathbf{x}_i^p)^T] = \max_{\mathbf{x}_i^p \in D_u^p} \{1 + \sigma_i^p(1-\sigma_i^p)(\mathbf{x}_i^p)^T Q^{-1}\mathbf{x}_i^p\} \tag{16}$$

where we assume the existence of $\mathbf{Q}^{-1}$, which can often be assured by using sufficient auxiliary data D^a.

Evaluation of Eq. (16) requires the true values of $\mathbf{w}$ and $\boldsymbol{\mu}$, which are not known *a priori*. We follow ref. 24 and replace them with the corresponding estimates obtained in the most recent iteration, based on D^a and $D^p{}_l$ selected up to the present.

Results and Discussions

We considered a UXO data set consisting of six items, including four targets (the two mortar rounds, the 155 mm shell, and the 5 inch rocket) and two false targets (cinder block and large rock). Each item has low-frequency as well high-frequency measurements at every one degree of azimuth angle, covering the full 360 degrees. We formed a vector of characteristic features by concatenating the low-frequency and high-frequency measurements at every azimuth angle for every item. The measurement angle of low-frequency measurements starts from 0°, while that of high-frequency measurements starts from 0.5°. Since the sensor's operating frequencies are not high, the signatures should not change too much with a 0.5 degree variation. We therefore ignored the difference and concatenated the low-frequency measurements at 0°, 1°, 2°, etc to the high-frequency measurements at 0.5°, 1.5°, 2.5°, etc.

Table 1. UXO/Clutter configuration of training set and test set

Experiment	Training Set		Test Set	
	UXO	**CLUTTER**	**UXO**	**CLUTTER**
1	155mm shell, 80mm mortar	Cinder Block, Rock	5 in rocket, 120mm mortar	Cinder Block, Rock
2	155mm shell, 5" rocket	Cinder Block, Rock	80mm mortar, 120mm mortar	Cinder Block, Rock
3	155mm shell, 120mm mortar	Cinder Block, Rock	80mm mortar, 5 in rocket	Cinder Block, Rock
4	155mm shell, 80mm mortar	Cinder Block, Rock	5 in rocket, 120mm mortar	Rock
5	155mm shell, 5" rocket	Cinder Block, Rock	80mm mortar, 120mm mortar	Rock
6	155mm shell, 120mm mortar	Cinder Block, Rock	80mm mortar, 5 in rocket	Rock

We performed 6 "experiments", with the training and test UXO/Clutter types configured as shown in Table 1. In each experiment, we have a total of four training items and four test items, each item having 360 feature vectors constructed as described earlier; this yields a training set of 1440 feature vectors and a test set of equal size.

We compared the concept-drift learning against regular learning, where the former is implemented by Migratory logistic regression (MigLogit) and the latter implemented by standard logistic regression (Logit). The MigLogit is trained on the training set D^a plus a subset $D^p{}_l$ actively selected from the test set D^p. Three Logit classifiers are trained, based on $D^a \cup D^p{}_l$, $D^p{}_l$,

and D^a, respectively. The four classifiers are then tested on $D^p{}_u=D^a\backslash D^p{}_l$.

We found that the concept-drift learning yields significantly better performance than that of regular learning, regardless of how the standard Logit is trained. When trained on $D^p{}_l$ alone, the performance of Logit catches up with that Miglogit when $D^p{}_l$ grows significantly large (>400, for example).

We also found that the performance of Logit trained on $D^p{}_l$ alone changes dramatically with the size of $D^p{}_l$, when $D^p{}_l$ is small. This can be explained by the fact that the examples in $D^p{}_l$ are the only determining factors affecting the formation of the final decision boundary. With a small number of examples in $D^p{}_l$, the decision boundary is not yet mature and can wander around, which produces the irregular part of the curve. As $D^p{}_l$ grows large, the decision boundary converges to the optimal one, which explains why the performance finally catches up with that of MigLogit.

We did observe some temporary cases in which the Logit trained on a small $D^p{}_l$ alone outperforms MigLogit. These cases are purely accidental and the performance drops easily as more data come into $D^p{}_l$. The accidental cases can occur when the corresponding $D^p{}_l$ happen to produce a decision boundary that coincides with the optimal one. The performance in these accidental cases does not represent the optimal one upon convergence, when the performance is consistently good as $D^p{}_l$ grows.

Summarizing the results to this point, an extensive, broadband acoustic scattering data base has been generated for six UXO targets, two false targets, and two concrete-filled metal pipe overlap targets. The UXO targets include a 80mm mortar round, a 120mm mortar round, a 105mm SABOT round, a 155mm shell, a five inch rocket, and a small 25mm dummy cartridge. The UXO target scattering data base taken in the free-field is the first of its kind covering frequencies from 1 kHz to 140 kHz over the complete 360 degrees of aspect. All six UXO targets show scattering levels which should be detectable at reasonably long range (>100m) even in noisy background environments. A variety of structural acoustic mechanisms including elastic phenomena produce features over large sectors of aspect which can be exploited for target identification using modern day classifiers such as Relevance Vector Machines and Kernel Matching Pursuits. Using the latter, it is shown how the target features separate from UXO to UXO and from UXO to false target. Some progress has been made on the development and application of identification algorithms that could, using training data gathered from one site, operate effectively on targets in another site having different environmental acoustic parameters.

NUMERICAL STUDIES OF FREE-FIELD, PROUD, AND BURIED TARGETS AND THE EFFECTS OF SEDIMENT SURFACE ROUGHNESS

We have carried out numerical studies of backscattering from the 5" rocket UXO near a smooth or rough water-sand interface using EFIT two-dimensional simulation model[25]. The elastodynamic finite integration technique[26] (EFIT) code is a time-domain method which uses a time-domain version of a perfectly matched layer (PML) to truncate boundaries. The code is

useful for the treatment of pulse propagation in inhomogeneous fluid-elastic environments such as are of interest in the underwater UXO problem. The generality of EFIT allows for the inclusion of stratified bottoms with rough interfaces and volume inhomogeneities such as rocks, shells, and other buried objects. Current code (written by Calvo) has a Cartesian grid and requires computations with and without the target present to isolate scattering. For these numerical studies, the following conditions are applicable: 1) Two-dimensional EFIT numerical models were applied to model scattering at beam incidence; 2) a correction factor of $10\log_{10}$ $(aL^2/2\lambda)$ is added to the 2D target strength to obtain an approximate 3D target strength in order to compare with experimental data; 3) we have neglected attenuation/absorption in the EFIT code (although we plan to include it at a later time); 4) an effective cylinder length (equal to the un-tapered casing length) of 0.3 meters is used.

a)

b)
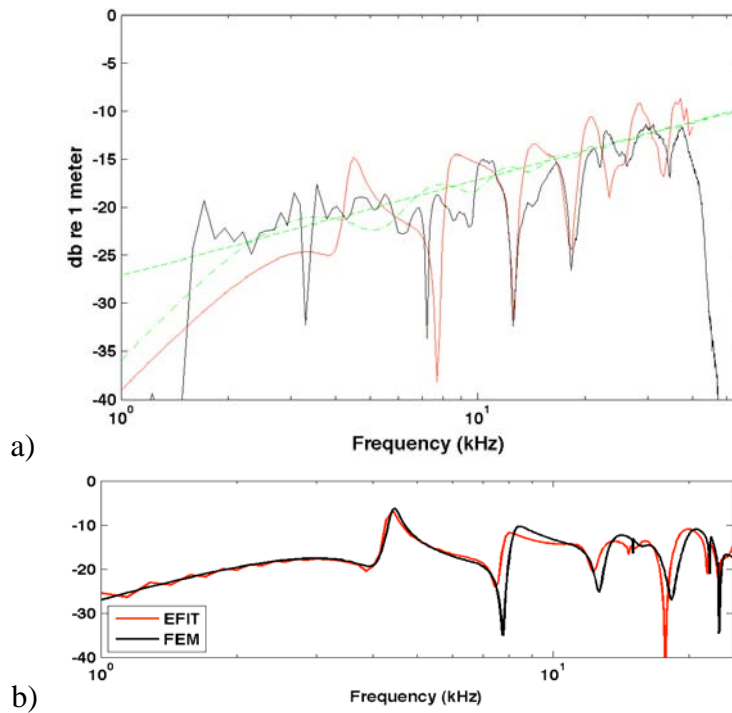
Figure 31 – Target Strength versus Frequency for Infinite Cylindrical Shell with Five Inch Rocket Parameters.

a) Broadside target strength versus frequency computed for infinite cylindrical shell with five inch rocket parameters and 3D wave correction compared to measurement. Black: measured data; red: COMSOL 2-D FE calculation with 3D wave correction; green-dashed: $10\log_{10}$ ($aL^2 / 2\lambda$); green-dashed-dot: wave theory rigid 2D cylinder with finite length 3D wave theory correction. b) comparison between the EFIT and finite element broadside scattering predictions for infinite cylindrical shell with five inch rocket parameters and 3D wave correction. Target strength in dB: red – EFIT; black- finite element both wave-corrected for 3D.

Shown in Fig. 31a is a comparison of the results of the EFIT 2D model with finite length 3D wave theory correction for an infinite cylindrical shell with 5 inch rocket parameters compared to the measured data for broadside (90º) backscattering. Also shown are the results

35

using 2-D finite element-based model with 3D wave correction. As can be seen, the 3-D corrected EFIT result is in overall agreement with the levels and trends of the measured data. In Fig. 31b is shown the comparison between the EFIT versus finite-element result. As can be seen, the main features are in reasonable agreement, and the discrepancies can likely be eliminated by: 1) modifying EFIT to solve directly for the scattered and not the total field (source effects may cause shifting of the TS with frequency and time-domain methods are like experiments); 2) reducing numerical dispersion or dissipation (although the shell is 13 grid cells thick for EFIT); and 3) using a non-uniform grid instead of a constant step size Cartesian grid. In any case, we believe the agreement is sufficient to allow confidence in the following case study results using EFIT.
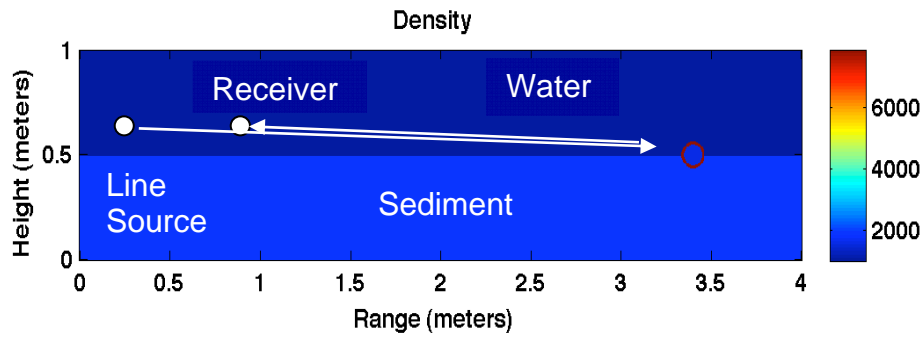
Figure 32 – Scattering Geometry for EFIT Calculations.
The receiver and source are below the critical angle.

Figure 32 shows the geometry for both the EFIT calculations as well as the laboratory measurements. The sediment is assumed non-dispersive with speed 1680 m/s and density 1966 kg/m^3. The water has sound speed 1482 m/s and density 1000 kg/m^3. The receiver and source are 10 cm above the sediment, with the former at a 2.01 m range and the latter at a 2.75 m range.

In Fig. 33a we show the comparison between the EFIT simulation and the laboratory measurement[9] for the free-field target case. Overall, the agreement is reasonably good given the lack of a direct inclusion of scattering and elastic wave interactions that can take place by virtue of the presence of the physical ends of the target

FREE FIELD
3D corrected 2D target strength (monostatic) for 5 inch rocket, beam angle.
Computed using EFIT
2 degree grazing angle, line source, no 3D correction of result
Source and receiver height above sand = 10 cm
Distance to source 2.75 meters, distance to receiver 2.01 meters

Figure 33a – Target Strength versus Frequency.
EFIT model result for infinite cylindrical shell with five inch rocket parameters and 3D wave correction compared to laboratory measurement for free-field five-inch rocket target.

PROUD
3D corrected 2D target strength (monostatic) for 5 inch rocket, beam angle.
Computed using EFIT
2 degree grazing angle, line source, no 3D correction of result
Source and receiver height above sand = 10 cm
Distance to source 2.75 meters, distance to receiver 2.01 meters

Figure 33b – Target Strength versus Frequency.
EFIT model result for proud infinite cylindrical shell with five inch rocket parameters and 3D wave correction compared to laboratory measurement for proud five-inch rocket target.

37

HALF-BURIED
3D corrected 2D target strength (monostatic) for 5 inch rocket, beam angle.
Computed using EFIT
2 degree grazing angle, line source, no 3D correction of result
Source and receiver height above sand = 10 cm
Distance to source 2.75 meters, distance to receiver 2.01 meters
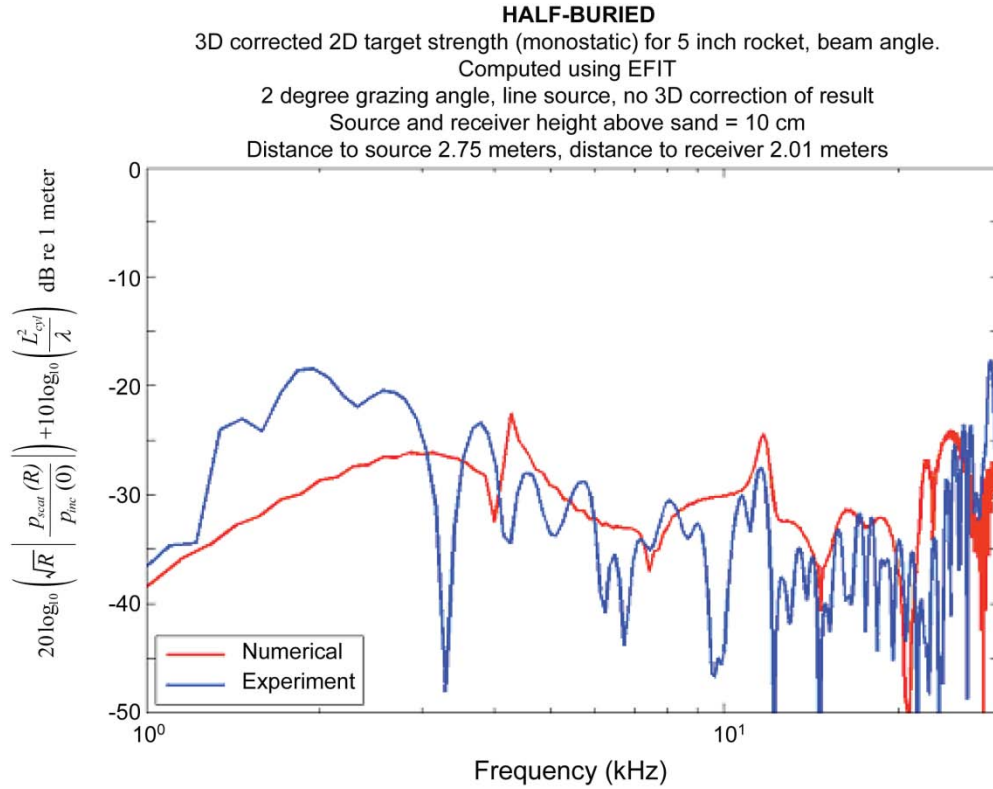
Figure 33c – Target Strength versus Frequency.
*EFIT model result for half-buried infinite cylindrical shell with five inch rocket parameters and
3D wave correction compared to laboratory measurement for half-buried five-inch rocket target.*

In Fig. 33b we show the comparison between the EFIT simulation and the laboratory measurement for the proud target case. Again, the agreement is reasonably good given the lack of a direct inclusion of scattering and elastic wave interactions that can take place by virtue of the presence of the physical ends of the target. The largest disagreement can be seen at around 1 kHz where the measurement shows an anomalously high peak. This peak is not observed in the free-field measurements suggesting that it may be an error in the processing for the measurement.

Next, we show in Fig. 33c the comparison between the EFIT simulation and the laboratory measurement for the half buried target case. Again, the agreement is reasonably good given the lack of a direct inclusion of scattering and elastic wave interactions that can take place by virtue of the presence of the physical ends of the target. We note that the experimentally observed peak in the proud case at the lowest frequencies is not seen in the half-buried case consistent with its absence in the free-field further suggesting that this peak may be related to a processing error in measurement for the proud case.

Finally, we show the calculated beam backscattered target strength for free-field, proud, half buried, and flush buried all plotted together in Fig. 34. It is clear from this figure that for beam back-scattering from a cylinder: (1) For a proud target, the impact of the surface of a

smooth sediment is minimal compared to the free-field case. In particular, at some frequencies the sediment acts to increase the target strength while at others to decrease it. However, in both cases the changes are relatively small. (2) Burial causes a large decrease in the target strength. Except at the lowest frequencies, even only half burial results in roughly a 10 dB decrease. In the flush burial case, however, there is anywhere from a 15 to 25 dB decrease across the band.
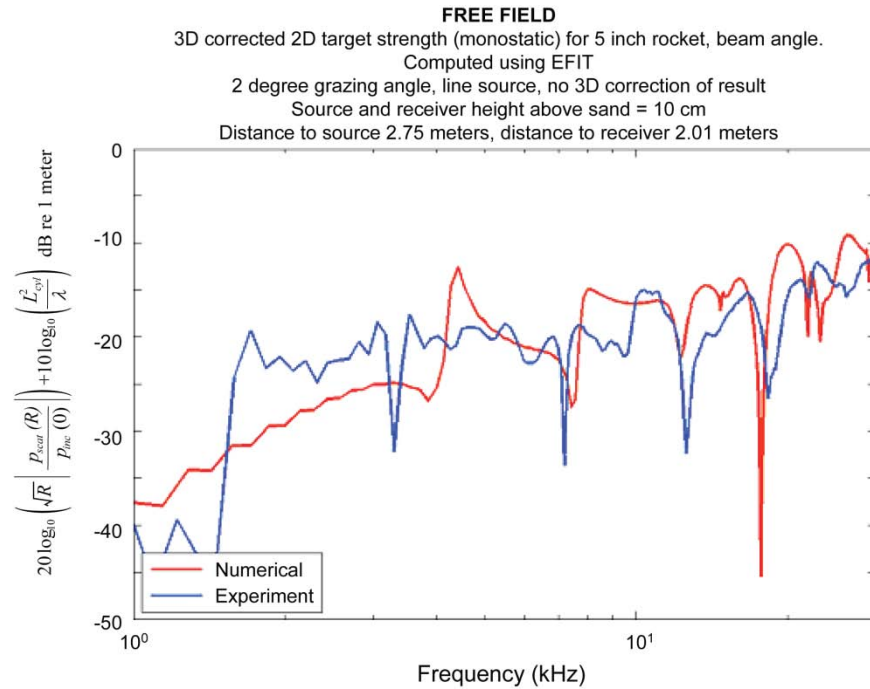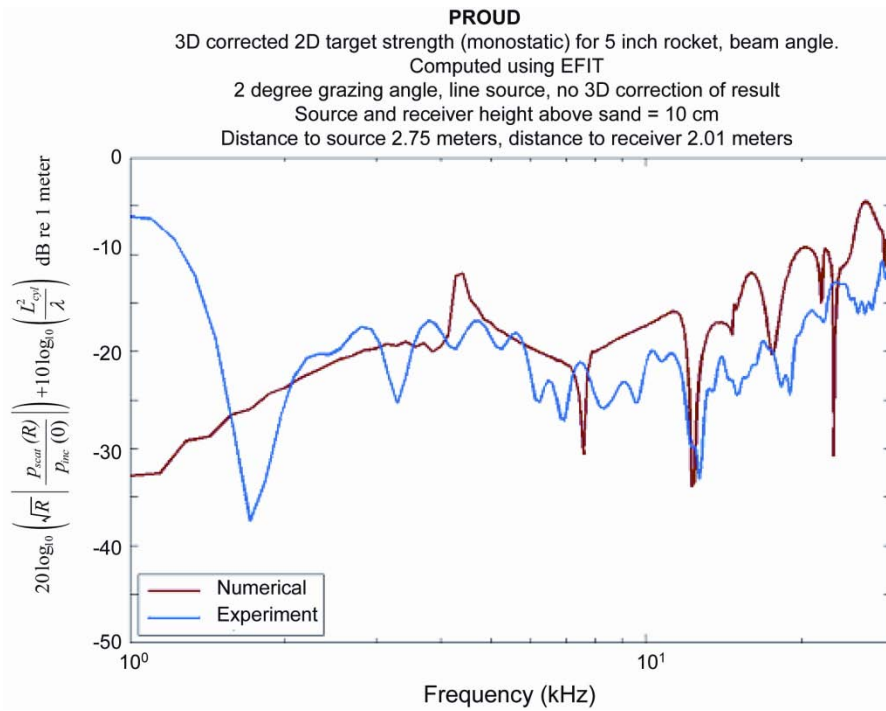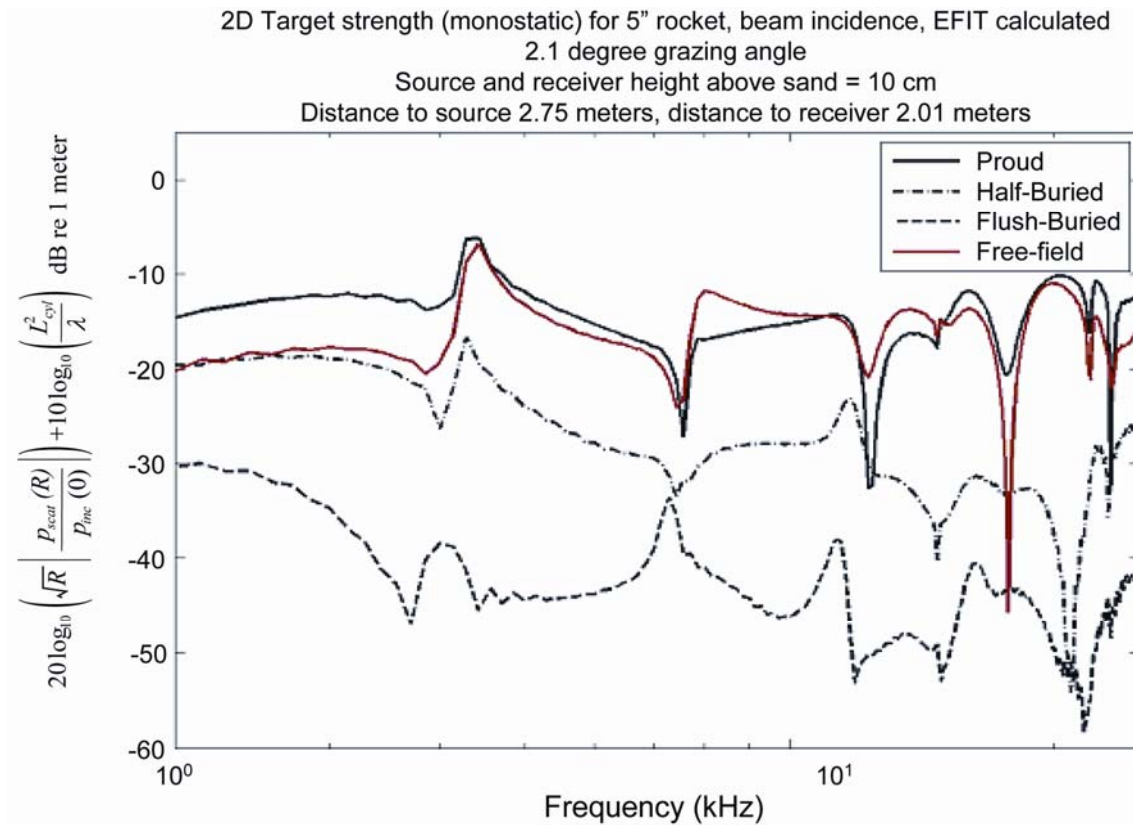

Figure 34. Backscattered Target Strength versus Frequency.
Calculated using EFIT model for infinite cylindrical shell with five inch rocket parameters and 3D wave correction for geometry shown in Fig. 6 and various burial conditions.

We have also used the EFIT model to better understand the effects of sediment interface roughness. Two effects due to roughness on which we have focused are (1) the impact of surface roughness on sediment sound penetration and on the subsequent echo from a buried target and (2) the scattering from the rough surface itself which acts as a reverberant field which can mask the returning echo. Other modeling techniques applied to this problem have been either perturbation approaches or high frequency approximations. In contrast, the EFIT method is uniformly valid in all frequency or interface height regimes and can be used to intuit, for example, at what frequency roughness begins to impact bottom penetration and the subsequent echoes.

We first introduce a randomly rough surface height in terms of a power-law spectrum, $W_S(K)$, where $W_S(K) = \eta\, K^{-\upsilon}$ if $K_{hp} < |K| < K_{lp}$ and is 0 for all other values of K. Here K is the interface Fourier wavenumber. In the following calculations we take $\upsilon = 3$, $K_{hp} = 10$ rad/m and $K_{lp} = 31.5$ rad/m. The interface profile is created by Fourier synthesizing the wavenumber spectrum with random (with equal probability) phases chosen between 0 and 2π for each discreet Fourier component. The constant η is chosen such that the RMS height of the interface is 2.5 cm. A Monte-Carlo method was then used to develop statistics by performing realizations (multiple full calculations in parallel) with typically 15 realizations. Three example realizations are shown in Fig. 35.
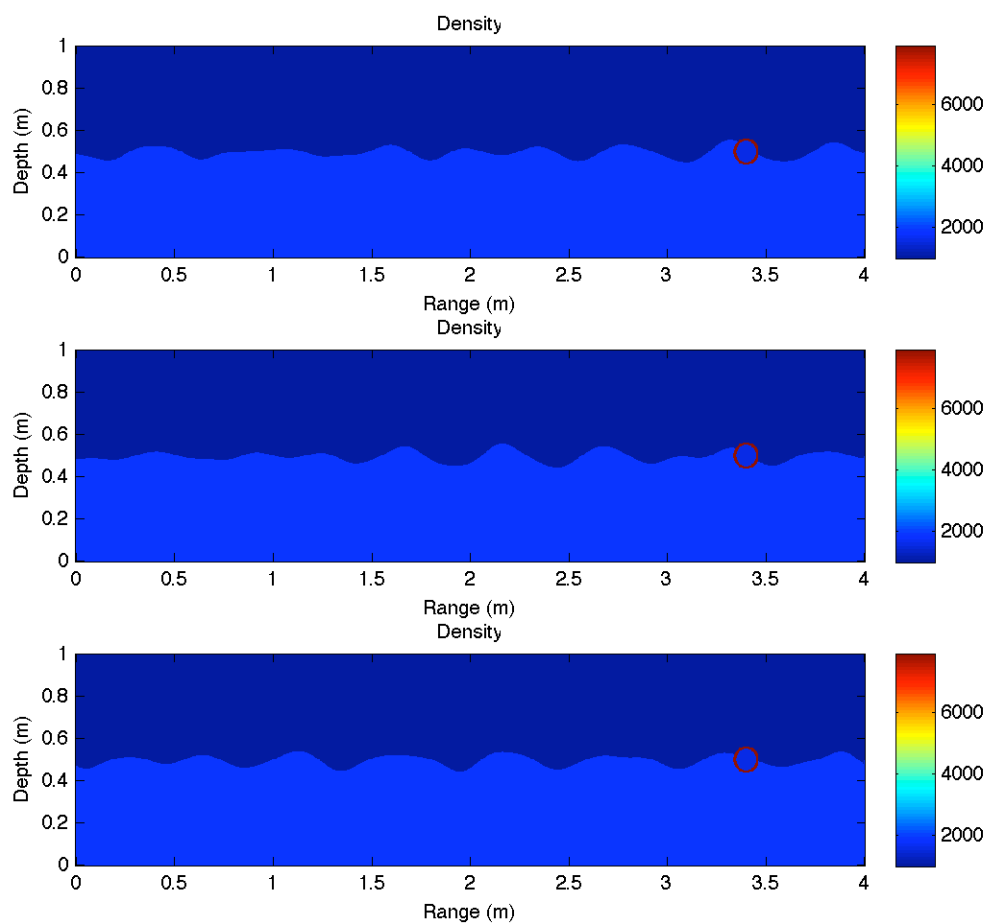
Figure 35 – Example Surface Roughness Realizations.
Three example surface roughness realizations.

First, we show the effects of surface roughness with the parameters discussed above on the echo from a flush buried infinite cylinder target insonified at beam. Figure 36a shows the echo versus frequency and receiver angle for a flat versus rough sediment interface for a 2 degree angle between the source to target direction and the sediment.
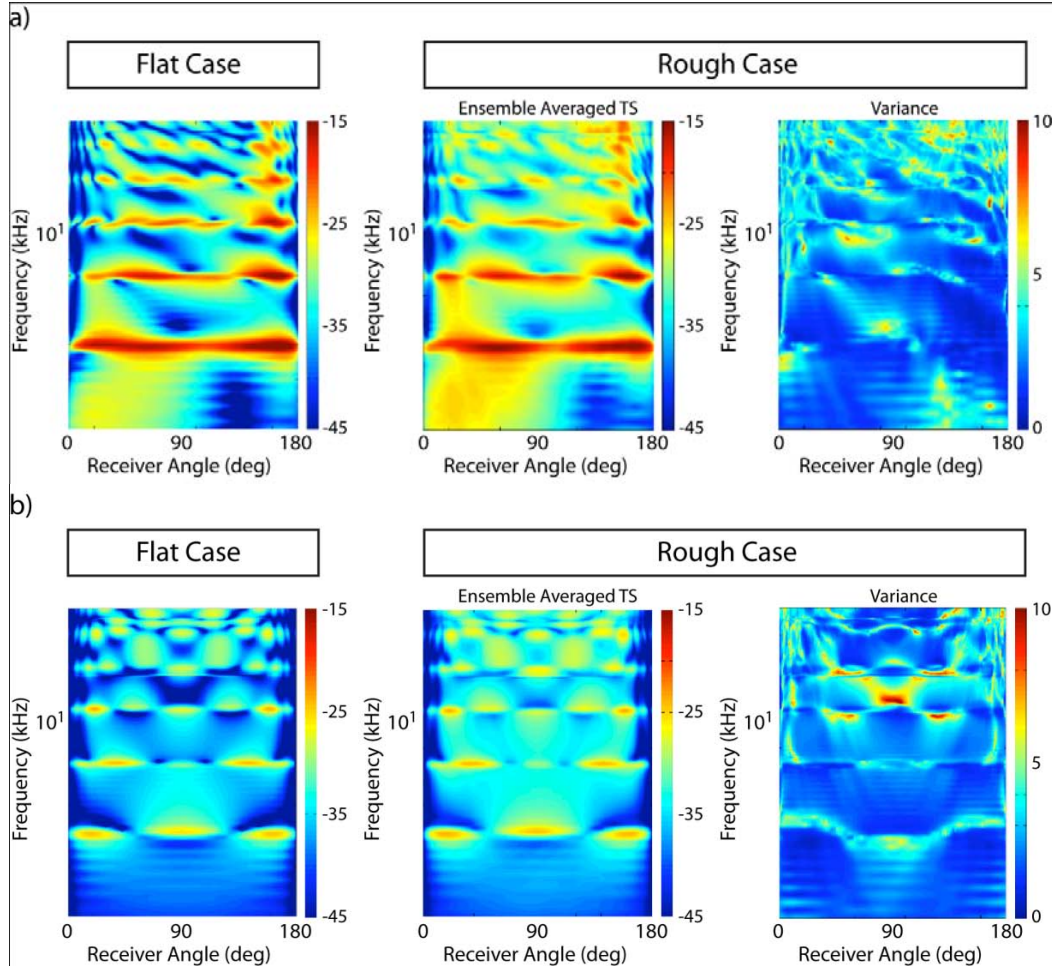
Figure 36 – Target Strength versus Frequency and Receiver Angle.
Effects of roughness for flush-buried infinite cylinder target with sound incident at beam on the target and a) 2 degrees with respect to the sediment surface; b)90 degrees with respect to the sediment surface.

Also shown is the variance between the two. As can be seen, on average there is some tendency for the rough surface to fill in the deep nulls and to cause some restructuring of the main frequency-angle features. Generally, but especially at higher frequencies, the variance is largest in the forward direction (180º).

Although the focus of these numerical studies was below critical angle insonification, in Fig. 36b are shown the same displays for the 90 degree source angle (or look-down) case. Here the structure in frequency and angle seems to be more preserved than in the grazing angle case, and the variance in the echo characteristics between flat and rough conditions is for the most part simply a small increase in the background target strength spread throughout frequencies and angles. That the frequency-angle features seem somewhat robust from flat to rough surfaces bodes well for application of the structural acoustic ID technique using the shorter range, look-down sonar configuration.

Next we discuss the time-series simulation results for the backscattered echo which includes contributions from both the sediment interface and a half buried infinite cylinder target insonified at beam by a 2 degree source. The scattered intensity back to the receiver versus time is shown in Fig.37 for an ensemble averaged rough surface compared to that for the flat surface case.
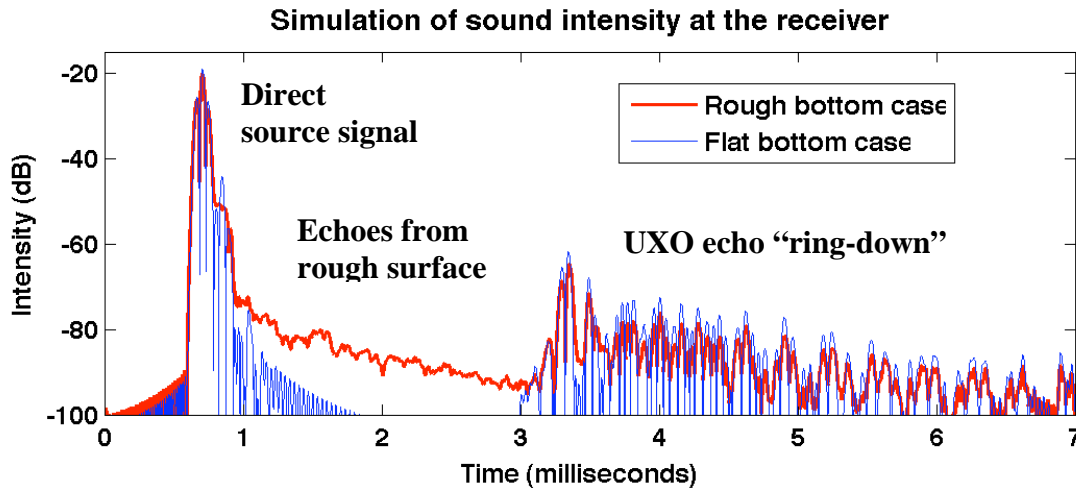
Figure 37 – Ensemble Averaged Reverberation Backscattered Intensity.
Time series for the half-buried infinite cylinder and a 2 degree source angle.

In Fig. 38 we show the target (half-buried) echo and the ensemble averaged reverberation backscattered intensity time series for 2º, 28º (critical angle), and 90º source angles. The simulation used a wide-band Ricker source pulse centered at 10 kHz covering a band 2 kHz to 30 kHz. First, we point out two anomalies in the reverberation simulation. First, the small bump just after 4 ms in the 2 degree case is an artifact related to reflection off the PML boundary. Second, the sudden drop in the reverberation seen in the 28 degree and 90 degree cases at long times is caused by the finite domain width used in the calculation (5.7 m). In any case, in the time window of the scattered target response, the reverberation from the rough sediment boundary generally increases as the source angle grows, from grazing conditions at the smallest angle to 90 degrees (having the sound source vertically above the target), and this is not surprising.
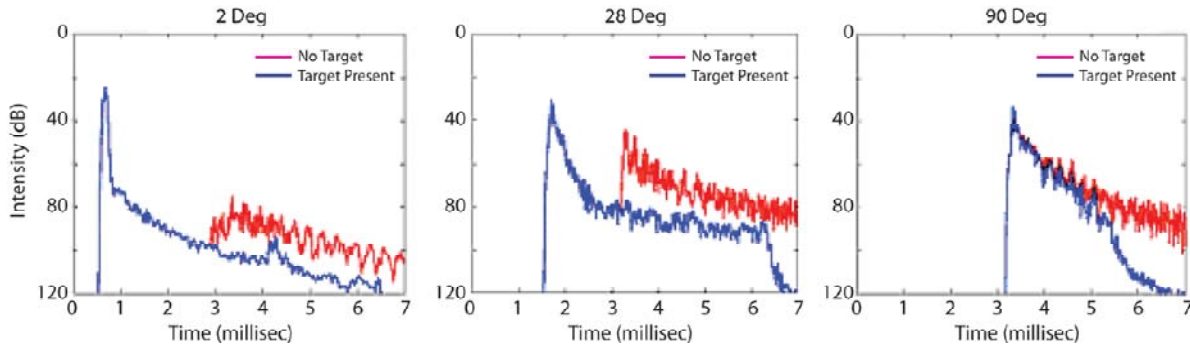
Figure 38 – Ensemble Averaged Target Echo versus Reverberation Backscattered Intensity.
*The time series are shown for 2º, 28º (critical angle), and 90º source angles. The simulation used
a wide-band Ricker source pulse centered at 10 kHz covering a band 2 kHz to 30 kHz.*

We make the following general conclusions regarding the effect of the rough sediment surface. At grazing angles (and thus for the more long range configurations), the reverberant background level is only moderately increased. However, there are some probably important changes in the frequency-angle feature structure. At look-down angles, there is a relatively larger increase in the background reverberant level. But there is less change in the frequency-angle structure.

BI-STATIC MEASUREMENTS BELOW THE CRITICAL ANGLE

Generally, experimental studies of scattering from proud or buried targets[27,28,29] have focused on monostatic scattering wherein the source and receiver are co-located. Here we present results[30] related to bistatic scattering and in particular its forward scattered component. We would like to explore whether forward scattering provides some advantage relative to backscattering especially regarding partially buried targets probed below the critical angle of the sediment/water interface.

Many UXO are more or less cylindrical in shape including the particular target whose bistatic target strength (TS) we discuss here. TS is defined in the usual sense[10] as $10 \log_{10}$ of the ratio of the intensity returned by the target in some direction, at a distance of 1m from its acoustic center, to the incident intensity from a distant source (plane wave). Apart from elastic effects, we can estimate what one would expect for the forward scattered TS of a finite cylinder using the analysis of Ross[31] as applied to the radar cross section of a perfectly conducting cylinder. As discussed by Bowman[32] for an electromagnetic wave incident normally on an infinite conducting cylinder, the problem reduces to the solution of a scalar wave equation for either horizontal or vertical polarization (parallel or perpendicular to the cylinder axis) of the same form as that for the velocity potential of an acoustic wave with soft or rigid boundary conditions, respectively. For this case, in the short wavelength limit the forward scattered TS depends in large part on the target's projected area with a correction term which takes into account the actual surfaces illuminated by the sound wave.

43

For the beam incidence (90°) case, Ross's[31] expression for forward scattering with wavenumber k gives

$$TS = 10\log\left|\sqrt{\sigma^{PO}(90^o)}\; W \exp\left(\frac{j\pi}{2}\right) + \sqrt{\sigma^{side}}\; \exp\left(\frac{j3\pi}{4}\right)\right|^2 \tag{17}$$

where $\sigma^{PO}(90°) = 4(aL/\lambda)^2$, $W = W_{hh} \sim 1 + 0.498(ka)^{-2/3} - 0.011(ka)^{-4/3}$ with $\sigma^{side} = 0$ for horizontal polarization, $W = W_{vv} \sim 1 - 0.432(ka)^{-2/3} - 0.214(ka)^{-4/3}$ with $\sigma^{side} = 7/\pi(a^3/\lambda)$ for vertical polarization, λ is the acoustic wavelength, $k = 2\pi/\lambda$, and L and a are the cylinder length and radius. The unity term in the expression for W is the physical optics result while the terms in inverse powers of ka account for the effect of the curvature near the shadow boundary. The last term gives the scattering from the ends.

For 0° incidence, Ross's result gives:

$$TS = 10\log\left|\left[\sigma^{PO}(0^O)\right]^{1/2} \exp\left(\frac{j\pi}{2}\right) + \left[\sigma^{CS}(0^O)\right]^{1/2} \exp\left(\frac{j3\pi}{4}\right)\right|^2 \tag{18}$$

where $\sigma^{PO}(0°) = \pi^2(a^2/\lambda)^2$, $\sigma^{CS}(0°) = 0.3(\pi aL)(a/\lambda)$. The first term is the physical optics result and the second term takes into account the contribution from the long, curved surface of the cylinder.

The particular target discussed here is the 5 inch rocket warhead. In an earlier report we presented measurements carried out in both free-field and sediment pool facilities with the target placed proud of, and then half buried in, the sediment. In the sediment facility, the source and receiver were 10 cm above the sediment surface; and for source-to-target and receiver-to-target distances used here (2.7 m and 2.0 m), the sound strikes the sediment at an angle much smaller than the critical angle ($\theta_C \sim 27°$).

The bistatic measurement process we employed is similar to that reported in Bucaro et. al.[9] for the monostatic case which used a nearfield cylindrical source array and a small "point" receiver rotating about the target. The data was collected and processed to recover complex scattering cross-section expressible as TS. The incident acoustic pressure in the form of a broadband pulse, the pool clutter (background) pressure, and the scattered pressure were measured in the following way. First, before positioning the target, the source was excited and the incident pressure measured at the location corresponding to the target center. Second the source was excited and the non-target pressure field measured as a function of θ at each receiver position to be used in the scattering experiment. This measurement contains scattering from pool clutter and, in the forward scattering plane, the incident pressure field. Lastly, the target was inserted and the scattered pressure field as a function of scattering angle θ_s was measured.

The TS was obtained by subtracting measurements made with and without the target. This process removes energy associated with the incident wave for bistatic angles in the forward plane as well as from spurious reflections from the finite-sized pool. With the non-target data

file removed from the scattered signal, the range-normalized and incident pressure-normalized parameter $X(f, \theta)$ is formed in terms of the scattered signal, $P_{scat}(f, \theta)$, and the incident field measured at the target center, $P_{inc}(f)$. Here the r dependent factor removes the effects of range from the pressure ratio term. The scattering data was measured at a range (2 m) which is in the near-field for some target aspects and in the far-field for others. Since bistatic data can be readily projected to the far-field, we performed this projection on all the echo measurements. TS values are then defined and displayed as $10\log_{10}(|X(f, \theta)|^2)$. Measured bistatic TS versus frequency and $\Delta\theta = \theta_S - \theta_i$ is shown in Fig. 39 for $\theta_S = 0°$ and $90°$ for the free field (upper row), proud (middle row), and half buried (lower row) cases. Also shown for comparison is the monostatic TS reported by Bucaro et. al.[9] versus frequency (2kHz to 25 kHz) and the source angle minus receiver angle. 0° and 90° source angles are on the left and right, respectively.
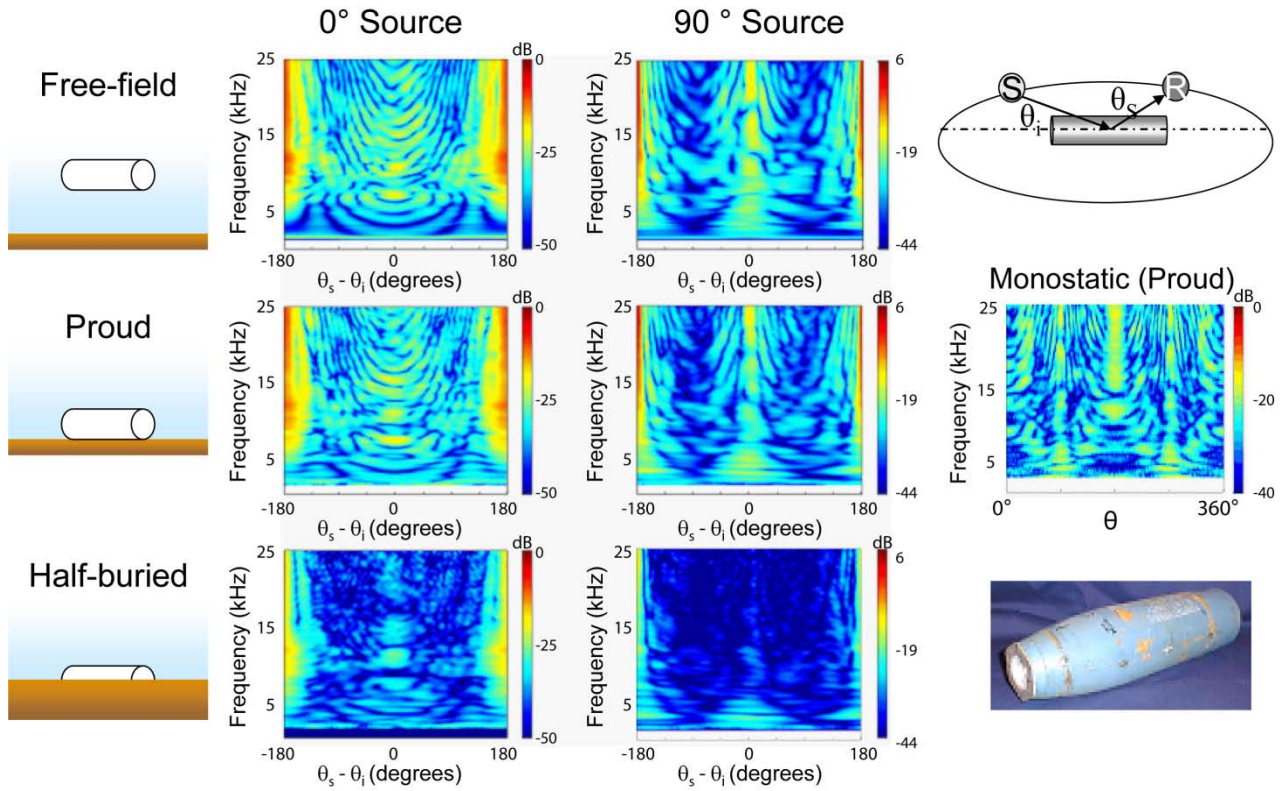
Figure 39 – Bistatic TS Measurements for Five-Inch Rocket.
Bistatic target strength displayed in dB as a color map measured for the five-inch rocket.

We show in Fig. 40a the result of Eq. (17) compared to the measured free-field data for the beam incidence (90°) case taking the rocket as a circular cylinder of length 18 inches and radius 2.5 inches. As can be seen, the two agree well over almost the entire frequency band. Overall, the data are closer to the rigid result than to the free case which is not surprising given that the target is a relatively thick-walled structure (the cylindrical wall is ~ half inch steel). We

note that the sharp peak at the lowest frequencies (which is even more pronounced in the 0° case) is due to a resonance of the air-filled back compartment (the end wall thickness is ~ 0.1 inches) as confirmed by finite element calculations we carried out indicating that at these low frequencies the structure is not totally rigid. As shown in Fig. 40b, for end-on incidence (0°) the agreement is good over most of the band, but Eq. (18) over-predicts TS at the lower frequencies. The analytic result has the same frequency dependence as that computed numerically using a T-matrix approach[16] for a rigid, hemi-spherically capped cylinder of about the same length for equivalent frequencies up to about 8 kHz. The latter has a TS level about 4dB higher, and this is presumably due to additional scattering from the curved versus flat ends. Why Eq. (18) is higher than the measured result at low frequencies is unclear.
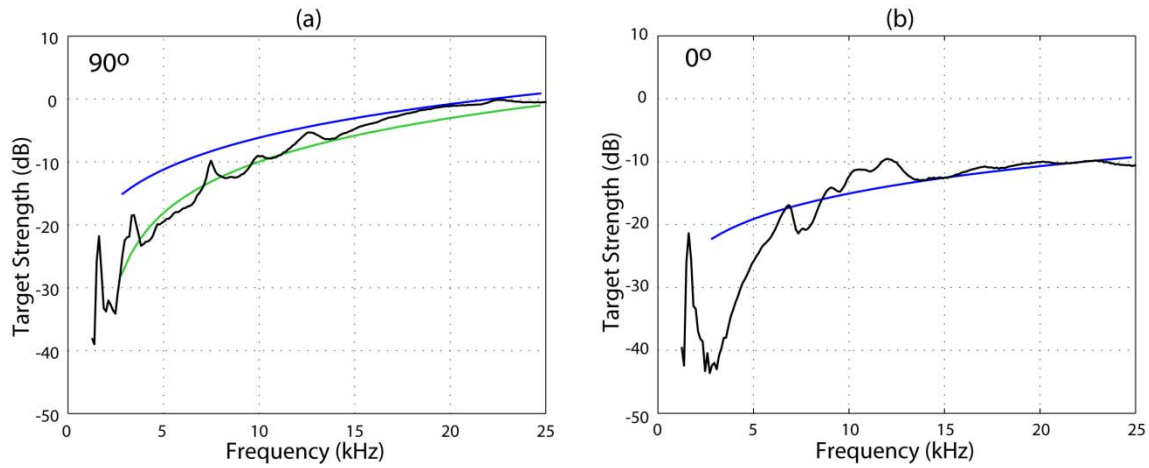
Figure 40 – Measured Forward Scattering TS Versus Analytic Model.
Measured free-field forward scattered target strength versus frequency in black. (a) 90° source; blue/green soft/rigid boundary condition theory, respectively; (b) 0° source; blue theory.

Consideration of these results and very similar results obtained for the 155 mm shell[9,30] leads to the following observations. (1) The forward scattered echo has TS levels that are significantly higher than any other return; (2) half burial of the target significantly reduces the backscattered TS levels but not the forward scattered levels; and (3) the leading forward scattering term for both 0° and 90° incidence is $\sigma^{PO}(90°) = 4(aL/\lambda)^2$ and $\sigma^{PO}(0°) = \pi^2(a^2/\lambda)^2$ which are proportional to the square of the projected areas. We therefore expect that the forward scattered TS for other aspects or other targets would be of order the projected areas with a 6 dB per octave increase with frequency.

We conclude that for the $\theta_i < \theta_C$ case, half-buried targets would be difficult to detect in backscattering. The question then becomes: in order to exploit the higher TS levels for the forward scattered echo upon burial, is it possible to extract the forward scattered echo from the strong overlapping incident field *without* having to remove the target as is done in the laboratory

measurement?

In the laboratory measurements presented here, we have been able to obtain an accurate measure of the forward scattered TS versus frequency and angle by precise mapping of the incident field (which can be one or more orders of magnitude larger than the scattered pressure) at the receiver locations *prior to target insertion*. This is of course not possible in an actual search in the environment for proud and buried targets. Field approaches which attempt to extract the incident field include for example mode filtering in a water channel[33] and apex shifted Radon transforms[34] as applied to ground penetrating radar. The former requires long vertical arrays which are not practical for our application. We illustrate here a source estimation technique[35] related to the latter[34] which uses knowledge of the source location and directivity.

Figure 41 – Possible Forward Scattering System Geometry.
Corresponding range-cross range plots, and forward scattered TS versus frequency and angle. (a) Hypothetical long range forward scattering measurement range: R_{ST}, R_{SR}, and R_{TR} are the source to target distance, the distance from the source to a particular receiver, and the distance from the target to a particular receiver, respectively; (b) time-cross range plots in dB for the direct source 150 meters from the center receiver (heavy line) and for the forward scattered signal x 30 with TS given by Eq. 4; (c) scattering TS in dB versus frequency and angle in the forward scattered sector for the scattering response given by Eq. (4); and (d) that extracted from the numerical results shown in (b).

Figure 41a describes a possible source-receiver-target geometry for long range (below critical angle) detection of proud or buried UXO. These receiver positions might be realized, for example, using an autonomous underwater vehicle (AUV) moving in a straight line. The location of the source relative to the i'th receiver (and therefore the corresponding distance $R_{SR}(i)$ to the i'th receiver) is assumed known a priori apart from random fluctuations but not R_{ST} or $R_{TR}(i)$, the source to target and target to i'th receiver distances. In Fig. 41b we show the time versus cross range plots calculated for signals at the various receiver positions due to a broadband (2 kHz to 50 kHz) point source (monopole) at R_{SR} = 150 m from the closest receiver together with a forward scattered signal (x 30) from an "unknown" target position (100 m from the source). For the latter we use a TS given by $10\log \sigma^{PO}(0°) = 10\log \pi^2(a^2/\lambda)^2$ (the leading term in Eq. (18) for the 0° source case) since 0° is the aspect with the lowest forward scattered level, and we take a that for the 5 inch rocket. The scattering angle dependence (the forward

lobe structure) associated with the physical optics area term above is assumed to be that for the far-field diffraction from an aperture of radius a leading to a TS (k,θ) given by

$$TS(k,\theta) = 10\log\left[\frac{a^2}{4}(ka)^2\frac{\sin^2(ka\sin\theta)}{(ka\sin\theta)^2}\right] \tag{19}$$

where the frequency can be made explicit using $k = 2\pi f/C$ with C the sound speed. We note that the associated scattered pressure we used has an $\exp(j\pi/2)$ phase term (see Eq. (18)) . We have also added -30 dB of random Gaussian noise and a random phase term $\exp(j2\pi fC^{-1}\Delta R(i))$ to the i'th receiver signal with $0 \leq 2\pi fC^{-1}\Delta R(i) \leq 4 \times 10^{-4} \times f$ to simulate random deviations (up to 0.1 m) of the AUV path from a straight line.

As can be seen in Fig. 41b, the source and target scattering signals map into two hyperbolas weakly modulated by the random phase term and noise since both free space Green's functions are of the form $R^{-1}\exp(j2\pi fC^{-1}R)$. Our proposed technique is as follows. (1) There is an angular region (here beyond ~ ±20° from forward) with no overlap of source and echo time signals, and here the forward scattered component is directly accessible. (2) In the overlap region, we would like to subtract the "known" source signal at each receiver from the total signal using the appropriate Green's function leaving the desired scattered pressure. However, the source signal is not known precisely due to the unknown random deviations of the AUV (the $\Delta R(i)$) from a straight line. We can, however, estimate each receiver position deviation by finding the local minimum for the difference between the received signal (the sum of the source, scattered, and noise signals) and an estimate of the source signal based on the known Green's function. Good estimates of the receiver deviations are so obtained because the source signal is much stronger than the other components of the received signal.

Carrying out this procedure on the data in Fig. 41b produces the TS frequency/angle map shown in Fig. 41d compared to that given directly by Eq. (19) in Fig.41c, both with the added noise. Apart from the obvious artifact (the vertical line structure), the process recovers TS(f,θ). The line structure corresponds to loci of receiver positions and frequencies where the path difference $R_{ST}+R_{TR} - R_{SR} = \pi/2$, which when added to the $\pi/2$ in the TS phase term (see Eq. (18)) leaves the echo with no quadrature component i.e. π out of phase with the source signal. As a consequence, our simple fitting procedure for determining the ΔR incorrectly eliminates the scattered signal at these particular (f,θ) points. Although not shown here, the extracted results and Eq. (19) at exactly 180° agree very well (± 0.3 dB) over the entire band.

We note that bistatic scattering measurements at vertical angles well below the critical angle made on a 5 inch rocket and a 155 mm shell UXO in the free-field, proud, and half buried in sediment indicate that for these conditions exploitation of forward scattering may provide a detectable signal with levels higher than that for backscattering and one that persists under partial burial. Above, we have illustrated for a point source in an infinite medium a technique that might be employed in a relatively simple environment to extract the forward scattered component from the much stronger incident field. We show later a wavenumber filter technique based on these dependences and demonstrate its practicality in measurements made in the Gulf of Mexico.

MEASUREMENTS IN ST. ANDREW'S BAY

Scattering measurements[37] were carried out on several proud UXO targets in St. Andrew's Bay where the water depths were on the order of 30 feet. Previously, the data associated with one of the targets, the 155mm shell, was analyzed with reference to measurements made in the sediment pool facility at much shorter ranges. The objective was to understand the differences observed for target scattering in these two environments.
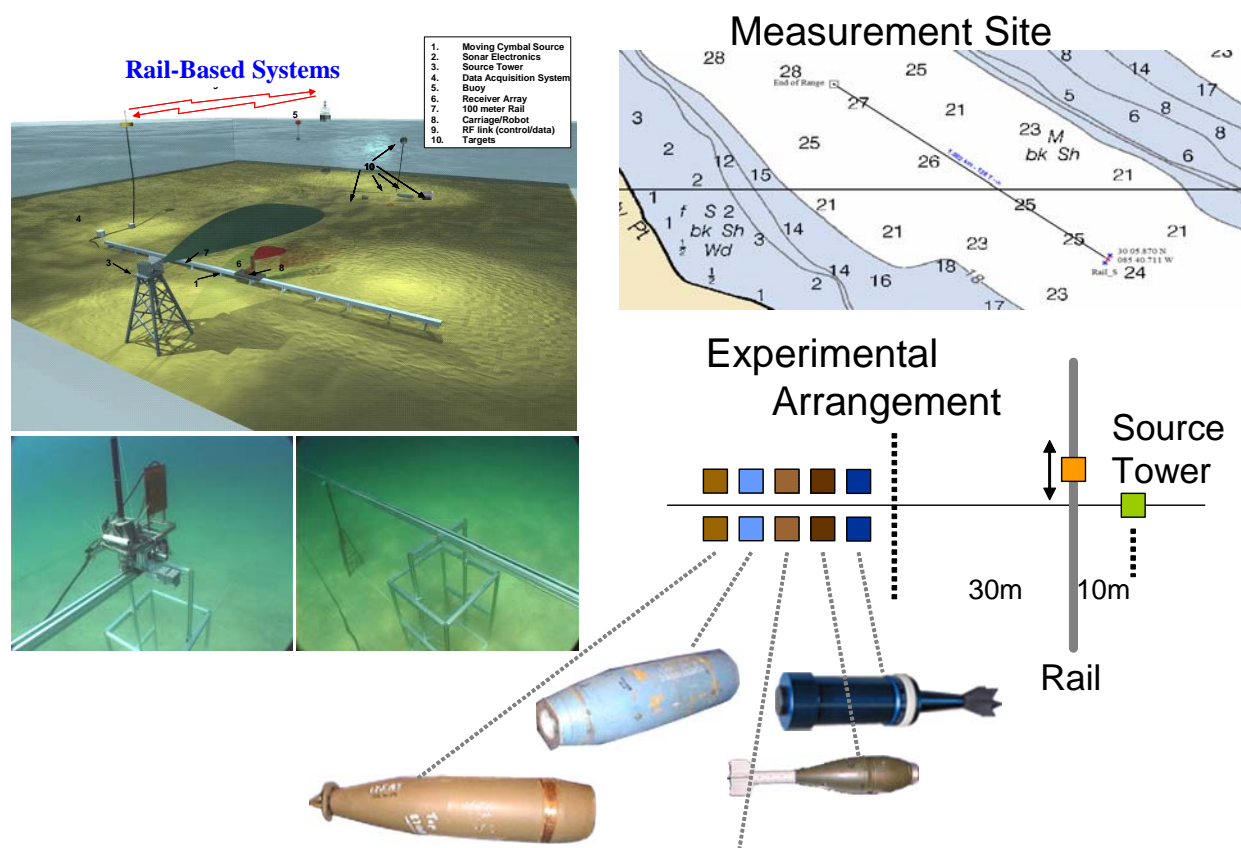
Figure 42 – Measurement Details at St. Andrew's Bay.

Upper right: Measurement site and water depths; lower right: UXO targets and their positions and the locations of the source and rail based sensor system; upper left: drawing of the source and rail system with both a moving source and receiver.

The Bay measurements utilized the NRL rail-based system and geometric layout shown in Fig. 42. The two main components are 1) a 30 meter long horizontal rail-based robotic scanner used to collect bistatic scattering data over a limited angular aperture and 2) a two meter long vertical sediment property scanner. The rail–based system is used in conjunction with a fixed impulsive broadband projector mounted to a tower 10 meters up range from the rail as shown in the figure. The different targets were positioned at various distances beyond the 30m

separation line from the rail as depicted in the figure. Computer-controlled measurements were executed with the raw scattering response from the fixed broadband projector collected from discrete receiver positions along the 30 meter rail. As with the laboratory-based systems, the data is post processed to extract the broadband scattering cross–sections from the area surveyed by the rail out to 100 meters with ~ 0.5 - 1 meter spatial resolution. The sediment property scanner is used to extract the sediment acoustic properties at the rail measurement sites (e.g., sound speed and attenuation versus frequency and depth).

The measurements were made at the St. Andrews Bay site located in the area also shown in Fig. 42. For the measurements, divers were used to deploy the source tower, the 30 m rail, the UXO targets, and the supporting equipment and cables for the system. Cables were pulled along the bottom to the support vessel named Mr. Offshore anchored in a two point mooring 190 m from the source tower. A military van was used to support all the top-side data acquisition and data processing equipment. The support vessel was placed in a "quiet" state during data acquisition, which required the use of an onboard generator that is vibration isolated from the ship hull. These have become standard operating conditions for NRL measurements using Mr. Offshore. A plan view of the experimental arrangement is shown in Fig. 42. As can be seen, the targets are placed at positions starting 30 meters from the rail, and although not indicated, the upper row of targets are aligned with their front facing the source (0°) and the lower row with their long side facing the source (90°).

In the measurement exercises at St. Andrew's Bay, bistatic measurements were collected over a limited range of scattering angles determined by the geometry of the rail-based measurement system. For either incident source direction, the bistatic angle range was about ± 27° about the source direction.

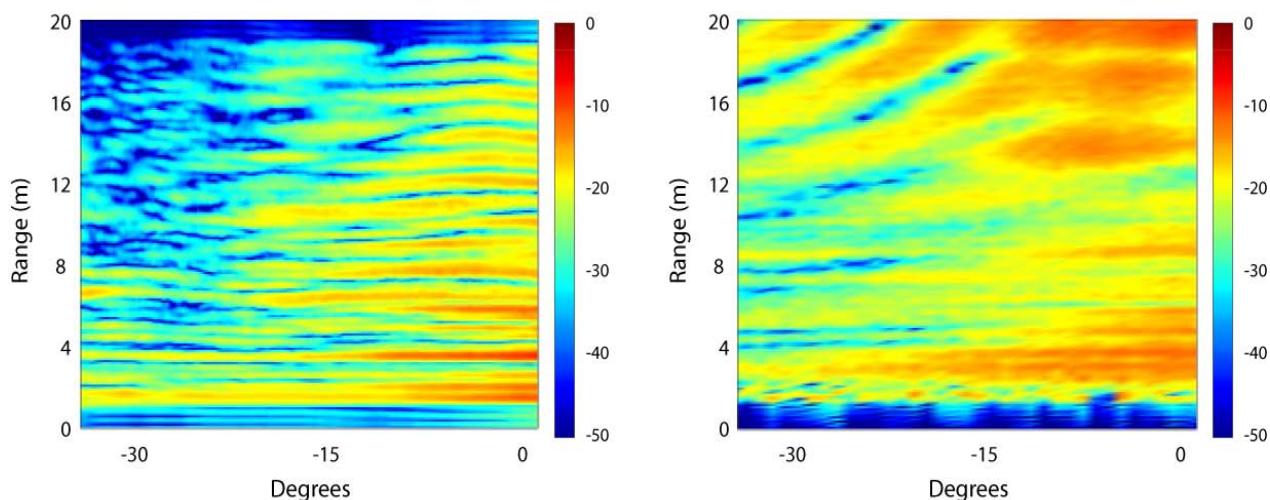**Figure 43 – Measured Target Strength.**
Magnitude of the bistatic target strength for 0° incidence coded in color versus frequency and scattering angle as measured in the Bay (left) and in the sediment pool (right) for the proud 155 mm shell.

50

The results for the 155 mm shell 90° incidence case are shown in Fig. 43 together with a comparison to that obtained over the same angular range for the measurements made in the laboratory sediment pool. As can be seen, the overall target strength levels are comparable. However, the frequency-angle patterns are different. Most noticeable is (1) the increased modulation with frequency of the directly backscattered echo for the Bay result, and (2) the lack of the strong bands for the Bay result in the higher frequency/scattering angle region as seen in the pool result. These bands are the modulation in the backscattered beam highlight caused by the finite target length. The frequency/angle shapes of these bands are determined by simple phase matching to the waterborne wave. In Fig. 44 we show line plots of the near backscattered response versus frequency for the 155 mm target. These plots show that at least for the backscattered case, the overall frequency trends are similar.

The differences observed between the very short range sediment pool measurements and the measurements in the bay are most likely due to one or more of the following conditions: (1) sediment properties; (2) geometric uncertainties; and (3) acoustic propagation. We believe that the largest effect by far relates to the last item, and we have considered this effect in some detail.
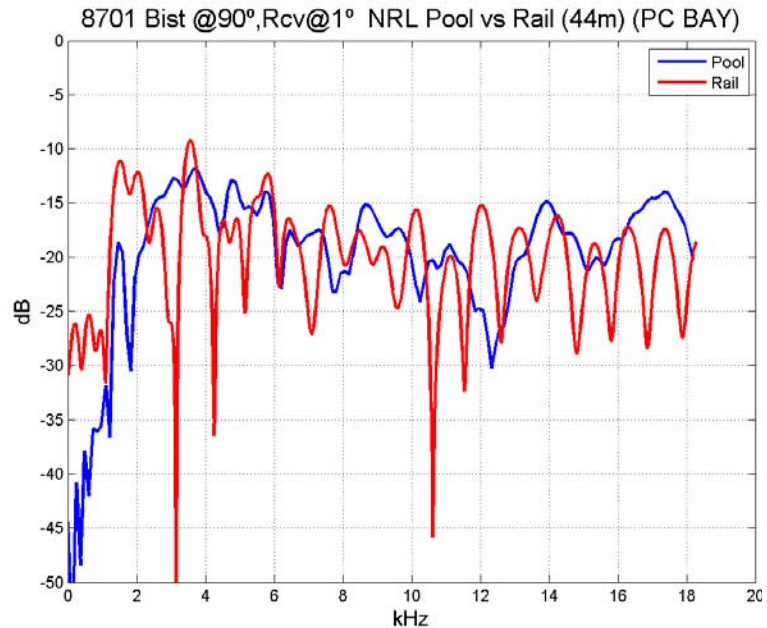
Figure 44 – Measured Target Strength.
Magnitude of the bistatic target strength for 0° incidence coded in color map versus frequency and scattering angle as measured in the Bay (left) and in the sediment pool (right) for the proud155mm shell.

In particular, we have used the Range-dependent Acoustic Model (RAM) model developed at NRL by Michael Collins[38,39]. This model is based on a user-selected multiple-term Padé approximation of the parabolic equation (PE) operator. Because this solution allows range steps much greater than the acoustic wavelength and does not require fine vertical gridding, RAM is a very fast research model.

As an illustrative example[37], we illustrate both the use of the RAM code and the impact of acoustic multi-path propagation in Fig. 45. Here the previously measured monostatic free-field scattered echo versus frequency and aspect angle for the 155 mm shell is projected using the RAM code to a 78 m range in a 30 foot water column with the properties associated with the measurement area of St. Andrew's Bay. The predicted target echo at that range is shown in the upper right of the figure. Also shown are the time pressure signals we have measured in the fluid and the sediment at 78 m using an array of sensors and what the RAM model would predict for this environment. Each of these consists of a number of signals with different arrival times

which are associated with the many propagation paths created by the multiple surface and bottom reflections. Some of these are illustrated in Fig. 46 along with the specific correspondence of a particular ray path with the appropriate time arrival.

Figure 45 – Simulated Effect of Propagation on the Monostatic TS.
Upper left: Measured monostatic free-field target strength versus angle and frequency for the 155mm shell shown in the upper photograph; lower: the measured and simulated (using RAM) acoustic pressure in the water and sediment versus time at the receiver for the St. Andrew's Bay site.
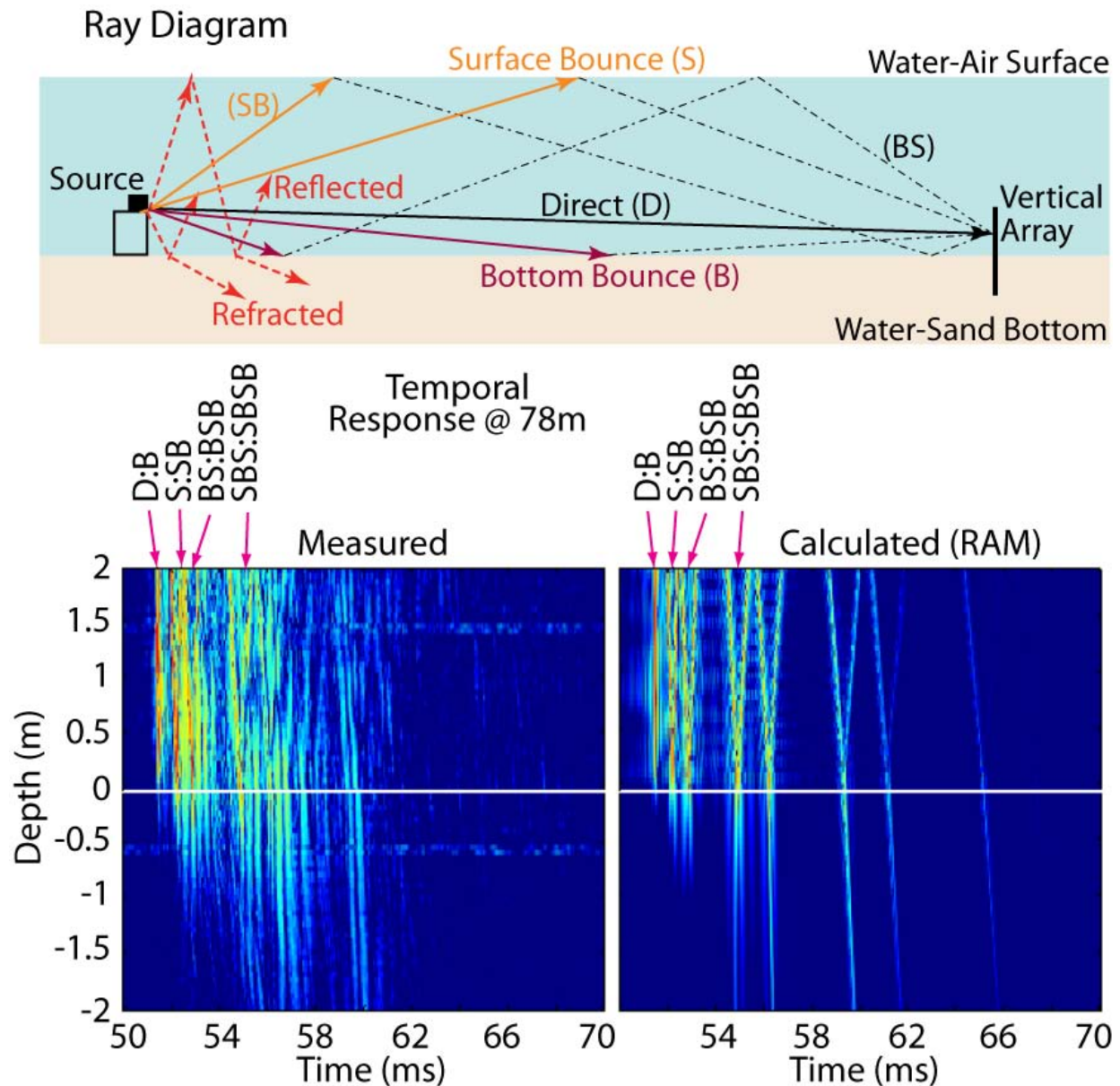
Figure 46 – The Major Rays Which Account for the Acoustic Propagation in the Water Column and Sediment.

Upper: The important rays from the source to the receiver array; lower: the measured and simulated (using RAM) acoustic pressure in the water and sediment versus time at the receiver for the St. Andrew's Bay site with some of the ray arrival times identified with arrows.

Having demonstrated the use of the RAM code and the effects of multi-path propagation, we now attempt to relate the measured target strength for the 155 mm shell made in the laboratory at short range (2 meters) and which contains only direct path rays to that measured in

St Andrew's Bay at a range of 42 m and having significant multi-path propagation. Specifically, we used the RAM code and the free-field measured target strength to predict what would be measured in the Bay, and the results are shown in Fig. 47. As can be seen, this introduction of the effects of multi-path propagation go a long way in producing the frequency-angle patterns actually measured at the longer ranges in the Bay. The remaining differences could be related to several factors. First, the sediment surface, assumed in our RAM projection to be flat, is actually not perfectly so. Second, there is some uncertainty regarding positioning of the target orientation and the source alignment (each of these are on the order of (± 5º).

Figure 47 – Target Strength versus Frequency and Aspect.
Measured in St. Andrew's Bay compared to that simulated using RAM and the laboratory measured free-field TS. In the bay results, the stationary source and moving receiver are 42 and 52 meters, respectively, from the 155mm shell target.
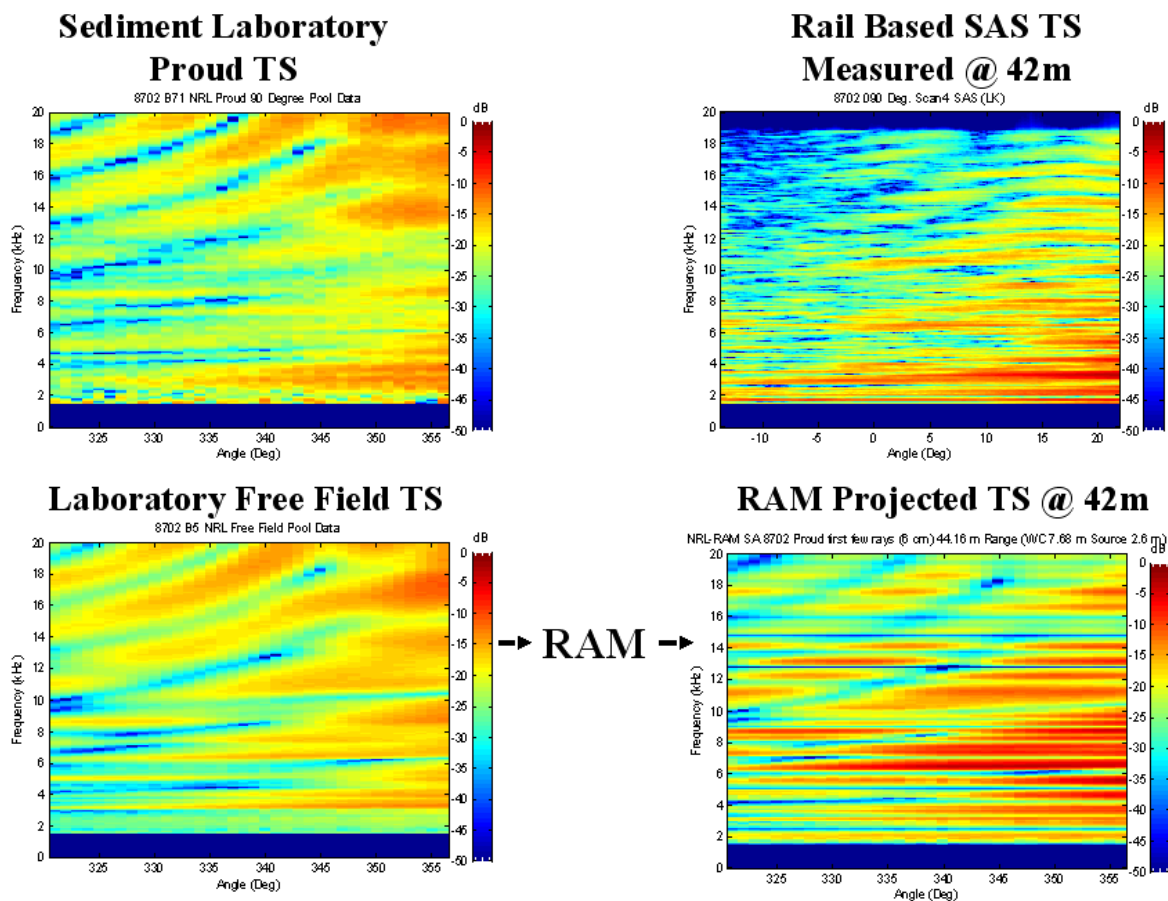
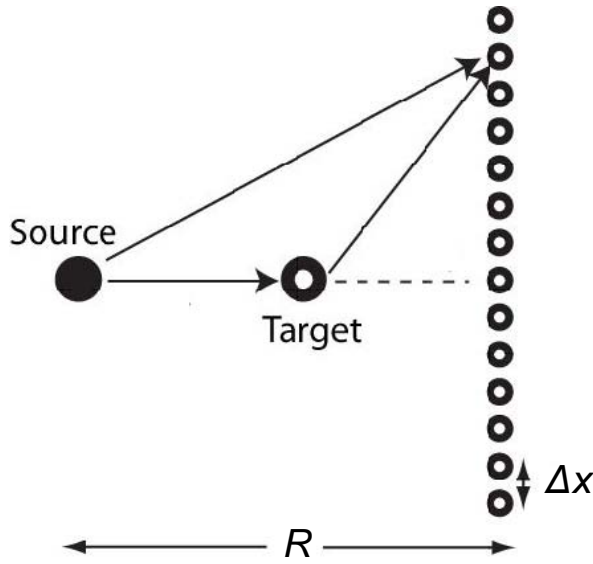# FORWARD SCATTERING MEASUREMENTS IN THE GULF OF MEXICO

Figure 48 – Typical Forward Scatter Geometry.
Point source and real or synthetic receiver array

Earlier, we discussed the observation of high forward scattering target strength (TS) levels for partially buried underwater unexploded ordnance (UXO) targets at low grazing angles and suggested that these high TS levels relative to backscattering could be exploited for detection of buried targets. This exploitation, however, requires that high quality forward scattering echo responses can be obtained in the presence of the much stronger spatially and temporally overlapping source signal. This has been possible in very stable laboratory pool environments by first mapping the incident source signal prior to insertion of the target and later subtracting this from the received signals. However, searching for targets in a real marine environment precludes the use of such techniques.

Here we describes a simple technique which exploits the hyperbolic character of the range - cross range dependence of the received acoustic signals to obtain a wavenumber-based filter which can remove the source signal from the receiver signals. Proper design and application of the filter to scattering measurements made in the Gulf of Mexico allowed a fairly accurate determination of the forward and near-forward scattering target strength of a spherical shell target lying proud on the sediment surface.

Range/Cross Range Description of the Source and Forward Echo Signals

Consider the forward scattering measurement geometry shown in Fig. 48. Here the parameter $\pm n$ denotes the receiver positions with the $n=0$ receiver on the line connecting the source and the target. One can realize these receiver positions, for example, using an autonomous vehicle traveling in a straight line or, as in the measurements described later, using a receiver moving on a rail mounted on the sediment. Ignoring bottom interactions and sound speed variations in the water column, the source signal, $P(n)$, at the nth receiver is

$$P(n) / P_S = \exp(ik_S\, r_{SR}(n))/r_{SR}(n) = \exp(ik_S\, r_{SR}(n))(R_{SR}^2+(\Delta x\cdot|n|)^2)^{-1/2} \qquad (20)$$

where P_S is the source strength, $r_{SR}(n)$ is the distance from the source to the nth receiver, R_{SR} is the distance from the source to the rail, k_S is the acoustic wavenumber, and Δx is the spacing

(uniform) between receiver locations. A similar expression can be written involving the point-scattered echo signal P_E at the nth receiver:

$$P_E(n) \, 10^{-TS/20} \exp(-ik_S r_{ST}) / (r_{ST} \, P_S) = \exp(ik_S r_{TR}(n)) / r_{TR}(n)$$

$$= \exp(ik_S r_{TR}(n)) \, (R_{TR}^2 + (\Delta x \cdot |n|)^2)^{-1/2} \tag{21}$$

where TS is the scattering object's target strength, r_{ST} is the distance from the source to the target center, $r_{TR}(n)$ is the distance from the target to the nth receiver, and R_{TR} is the distance between the target and the mid-point of the rail. The travel time versus cross-range plots associated with Eqs.(20) and (21) are hyperbolic functions each with their own apex and shape. If there were no uncertainties in the parameters, one could extract the source signal, $P(n)$, from the total received signals at each receiver using these known functions.

Three issues associated with the marine environment make this approach difficult. First, deviations from the hyperbolic function occur due to sound speed variations (both temporal and spatial), interactions with a sediment surface having height fluctuations, and receiver position uncertainty. Second, multiple hyperbolas appear caused by multi-path structure. Third, the echo level at the receiver could be very small compared to that of the source signal at the longer ranges often used in marine environments.

Figure 49 – Log of Ratio of Source to Scattered Pressure.
Parameterized by total range and plotted versus source to target distance over total range.

Figure 49 illustrates this third effect by showing the ratio of echo-to-source signal level at the center receiver for an object with a target strength of -20 dB. The curves are presented as a function of source-to-target distance normalized and parameterized by $R_{SR.}$. As can be seen, this ratio can be just a few percent for ranges approaching tens of meters, especially when the target is not close to the source or to the receiver.
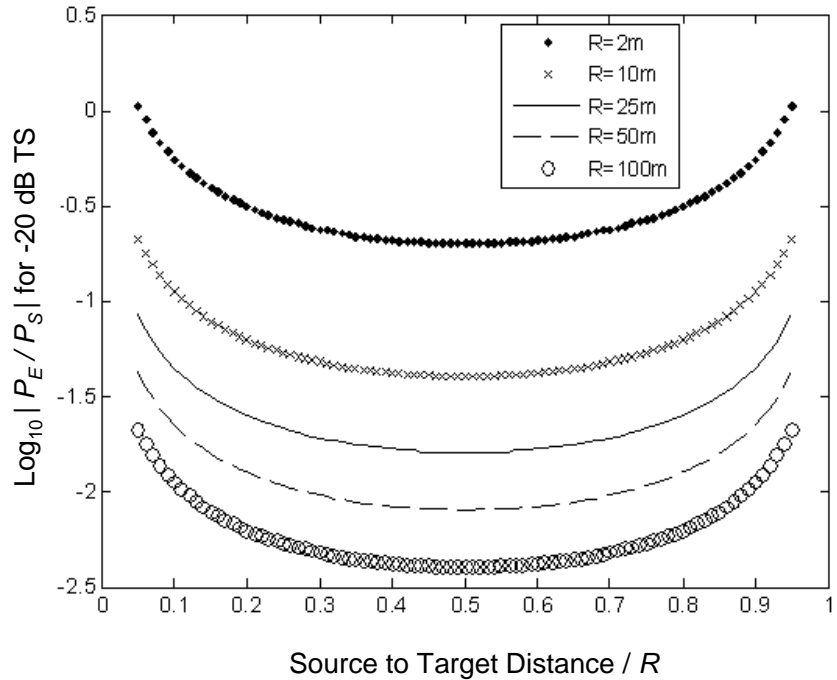
Wavenumber-Based Source Signal Removal Technique

The approach used here to extract and remove the source signal from the receiver signals is related to an approach used in ground penetrating radar. In particular, Yong *et al.*[34] and Kim *et al.*[40] use Radon transforms to map time/cross range functions into the ω/k (frequency/wavenumber) domain in order to design a filter for reducing clutter and ringing, respectively. The processing approach used here to extract forward scattering has five steps. (1) Project the signals at the equally-spaced N receivers back to the known source location. Were there no fluctuations, the source signals would be of the form $P_S\, r_{SR}^{-1}(n)\, exp\; ik_S\, r_{SR}(n)$. In this case the back projection would yield the source strength P_S. Fluctuations result in uncertainties in the $r_{SR}(n)$ denoted as $\Delta\, r_{SR}(n)$ such that the back-projection now results in terms of the form $exp[\; i\; k_S \Delta\, r_{SR}(n)]$. (2) Apply a spatial Fourier transform, which for small fluctuations gives

$$P_S \int dr \exp(-ikr) \exp ik_S \Delta r_{SR}(n)) \; \sim \; P_S\; [\; \delta(k) + \xi(k)] \; . \qquad (22)$$

Here the term $\xi(k) = k_S\, \Delta\, r_{SR}(k)$ includes all the fluctuation effects. (3) Apply a wavenumber-based filter of the form $\xi(k)$ to remove the source signal. The details of this filter are described in the following section. (4) Apply an inverse Fourier transform to the filtered signals, now expected to include only the forward scattered echo. (5) Project the result from the source back to the receiver positions.

Experimental Test in the Gulf of Mexico

Forward and near-forward scatter TS measurements were conducted in the Gulf of Mexico near Shell Island, Panama City Florida (see Fig. 50) in order to test this wavenumber-based filter approach. At this site, the water depth is 14m, and the bottom is covered with a medium-grain sand. The acoustic scattering response of a proud spherical shell target was measured around the forward direction over the 2 kHz to 23 kHz frequency band using a 16
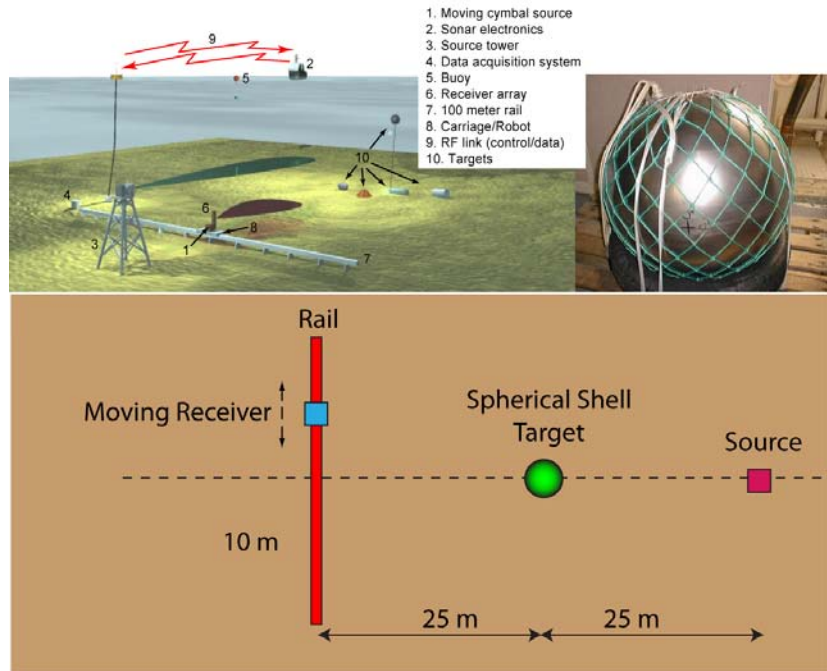

Figure 50 –Forward Scatter Measurements in the Gulf of Mexico. *Cartoon of the rail system, measurement geometry, and photo of the spherical shell.*

ms chirped waveform. The shell, made of 1.5 cm thick stainless steel, has a radius of 30 cm. With reference to Fig.48, the source was positioned 25 meters in front of the target (r_{ST}), and the receiver array was formed synthetically using a hydrophone moving along a 48 meter-long rail (Δx = 10 cm) positioned 25 meters beyond the target (R_{TR}). The source and receiver systems were 2.6m and 2.15m, respectively, above the sediment surface.

Fig. 51 (left) shows the resulting range/cross-range data curves where the multi-path hyperbolic structure for the incident source signal is quite evident. As indicated, the two strong source returns at the display bottom are the signals associated with the direct water path and the bottom bounce path. The strong source signal seen at upper portion of the display is due to the surface bounce. Most of the weaker features (some of which are indicated with white circles) are artifacts caused by the finite bandwidth source time-waveform deconvolution. Under close examination, one can see the scattered echo feature with its greatly reduced levels and much tighter hyperbolic curvature. Simple time-gating is effective in separating this forward echo from the direct and surface-bounce source signals but not from the bottom bounce source signal. For this the wavenumber filter approach was used.
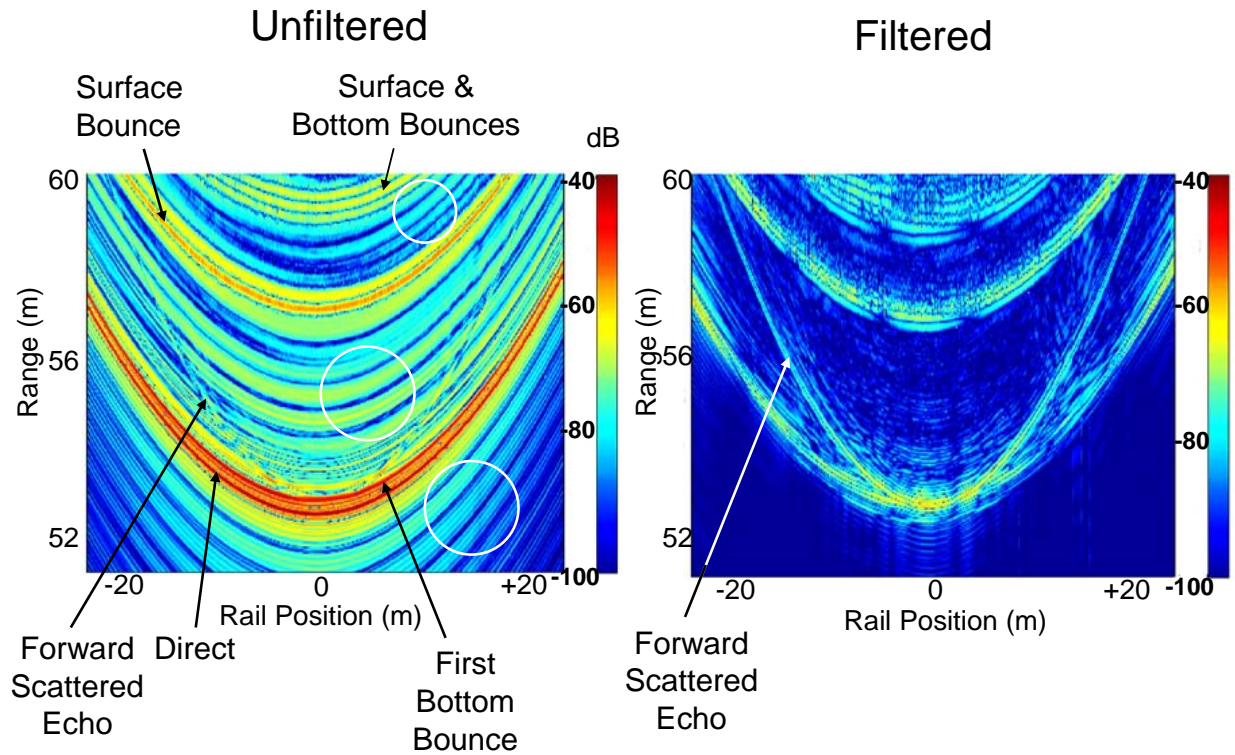

Figure 51 – Range – Cross-Range Maps of Gulf Receiver Measurements.
Left: Unfiltered data with various ray paths labeled. Right: After filtering using the wavenumber filter.

Equating the normalized width of the fluctuation term, $\xi(k)/k$, to $\Delta r_{SR}/r_{SR}$, a linear $\omega\text{-}k$ filter was implemented whose width is given by:

$$\Delta k(\omega) \ = \ k \ \Delta r_{SR}/r_{SR} \ = \omega/C_0 \ \Delta r_{SR}/r_{SR}. \qquad (23)$$

Here C_0 is the sound speed. Two sources of Δr fluctuations were considered, viz. spatially fluctuating sediment surface heights and sound speed variations in the water column. Sediment height variations on the order of 15cm and sound speed variations of 0.1%, both of which are reasonable for this environment, lead to Δr's ~ 5cm at the low grazing angles (~5°) and moderate ranges (~ 50 meters) associated with our measurements. Inserting these parameters into Eq.(23) results in a wavenumber filter width, Δk, of $8x10^{-3} \ m^{-1}$ at 2 kHz and $0.1 m^{-1}$ at 23 kHz.

Using the data as discussed above, a spatial Fourier transform was applied to the appropriate time-gated receiver array signals after projection back to the source location. The resulting signals were then passed through the linear wave number filter described above eliminating all energy centered at $k = 0$ and spread over $\Delta k \ = 3x10^{-4} \ \omega/C_0$. After application of an inverse Fourier transform, the transformed filtered signals were projected back to the receiver positions. The results are shown in the range cross-range plots of Fig.51 (right) where one can now clearly see the forward scattered echo even at angles approaching 180° (at the center of the receiver array).
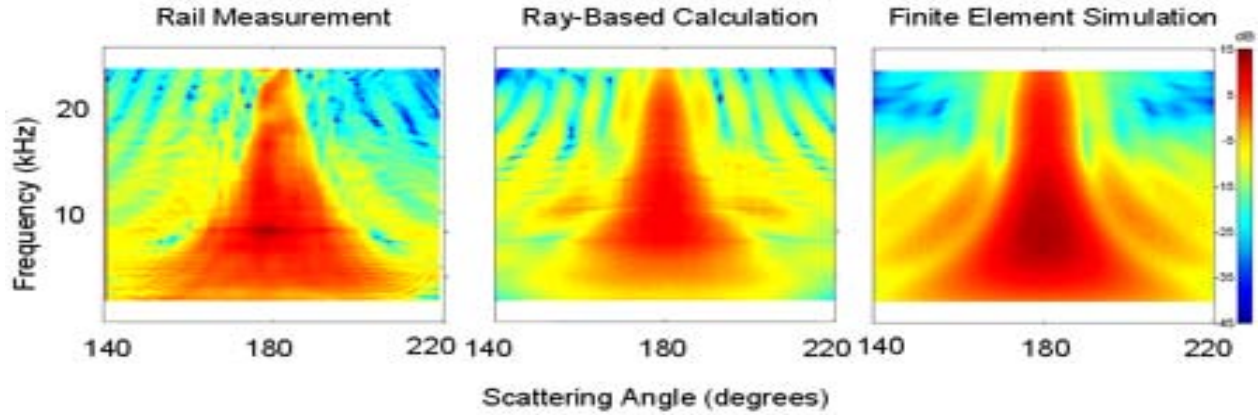
Figure 52 – Forward Scatter Acoustic Color Maps.
Left: rail measurement after filtering. Middle: computation with four rays. Right: finite element calculation

Figure 52 shows the scattered echo TS in the forward and near-forward directions obtained by this processing as a function of frequency and angle. Also shown are two predictions, one obtained from a finite element simulation and the other applying ray analysis to the well-known normal mode series solution for the free-field scattering from the spherical shell.[44] The former simulation uses the STARS 3D structural acoustics code[14] to model the elastic target, the water medium, and the sediment (treated as a fluid). The latter simulation

includes four source/echo ray component combinations: (1) the forward scattered echo reflects from the bottom; (2) the incident ray reflects from the bottom before striking the target; (3) the sound strikes the target at ~6º above the horizontal and is scattered in the near forward direction also ~6º above the horizontal; and (4) the incident ray reflects from the bottom before striking the target and the near-forward scattered echo (~6º from forward) does so as well. Line plots of the TS versus frequency at discrete angles between 140° and 210° are shown in Fig. 53. The general agreement between the measured TS and that of the two simulations can be seen in both Figs 52 and Figs. 53.

The agreement between the results of the simulations and the wavenumber-filtered measurements in the Gulf, while by no means perfect, indicates the validity of this approach and the potential in general for exploiting forward scattering in a real marine environment. The suppression of echo levels at the upper end 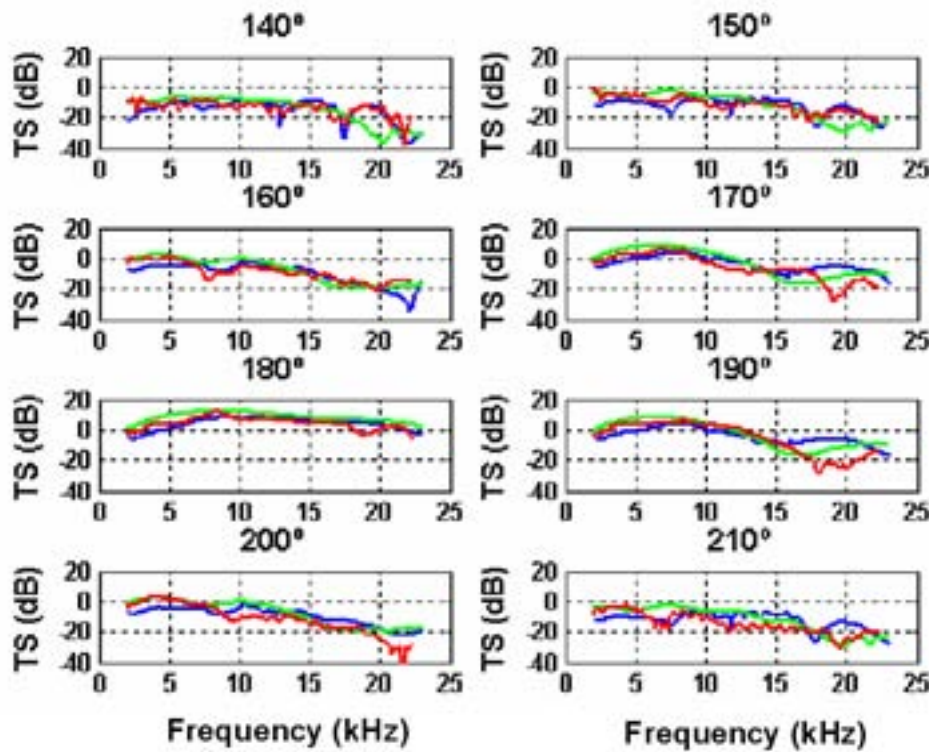of the frequency band, best seen in Fig. 53 for both the processed rail data and the simulations, is due to the Lloyd's mirror effect involving interference with reflections from the sediment surface. Although not shown here, the normal mode series solution at 180° and 23 kHz predicts a TS of 13 dB for the free-field case whereas our Gulf results yield -6 dB for the target proud on the sediment. The fact that our forward scatter extraction technique appears to be tracking these low echo levels is very encouraging.

Figure 53 – Target Strength versus Frequency.
TS at various angles for the filtered measurement (red), ray calculation (blue), and finite element calculation (green).

In this filter-based approach, one can expect under-estimation of the true echo level since some scattered energy is unavoidably eliminated in the subtraction process. However, the wavenumber-based approach tends to minimize this error since only a relatively small portion of the wavenumber echo spectrum is in fact eliminated as long as the fluctuations are not too large. This expectation was confirmed in our experimental case by passing the numerically simulated forward scattered echo (180º) received signals through our wavenumber filter and observing the impact on the frequency dependent TS. The worst case was found at the highest frequencies and resulted in less than 20% suppression in echo level.

60

In practice, although the bistatic approach described here is somewhat more complex than a monostatic system, the bistatic arrangement is fairly simple with only one source angle and a limited set of bistatic receivers. The source and receiver locations, however, must be known to about one acoustic wavelength, and coverage of a large area would of course require repositioning of the source and receiver array.

THE LARGE LOOK-DOWN ANGLE CASE

The large look-down angle case is illustrated in Fig. 54. Here one typically uses a limited aperture bi-static system in which the source illuminates the water-sediment surface below at angles well above the critical angle. In this case, the sound readily penetrates the sediment, and buried targets are detectable unless they are buried very deep in a sediment having a very high acoustic absorption. Of course, the trade off here compared to the long range, below critical angle case is a significant decrease in the area coverage rate.
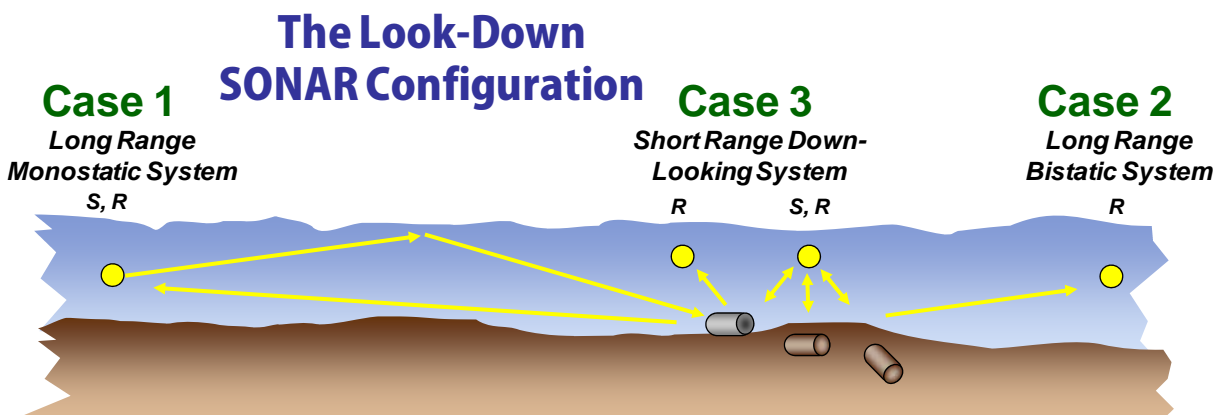
Figure 54 – The Three UXO Sonar Configurations.
The case 3 look-down configuration is highlighted. It is a short range, above critical angle, limited bistatic angle configuration.

In the final year of the program, the NRL sediment pool facility was extended to be able to collect buried target scattering data for the large look-down angle case. The resulting capability is diagrammed in Fig. 55. In this design, the receiver array is generated synthetically by robotically moving a receiver over a 2 dimensional planar surface just above the sediment surface. Although an actual operational system would not scan so near the sediment, we do so here because of the scientific information that is made available in this very near field. In

61

addition, data is easily propagated up to higher positions more typical of a system in the field so that we do not lose the system-relevant data. For lower part of the SA band, the receiver distance $<< \lambda$ so that we can obtain a so-called nearfield hologram (*NAH*)[42]. From this hologram, we can study the following questions:

- *Do evanescent waves matter?*
- *Can we project to water/ sediment interface?*
- *Can we project to planes below interface?*
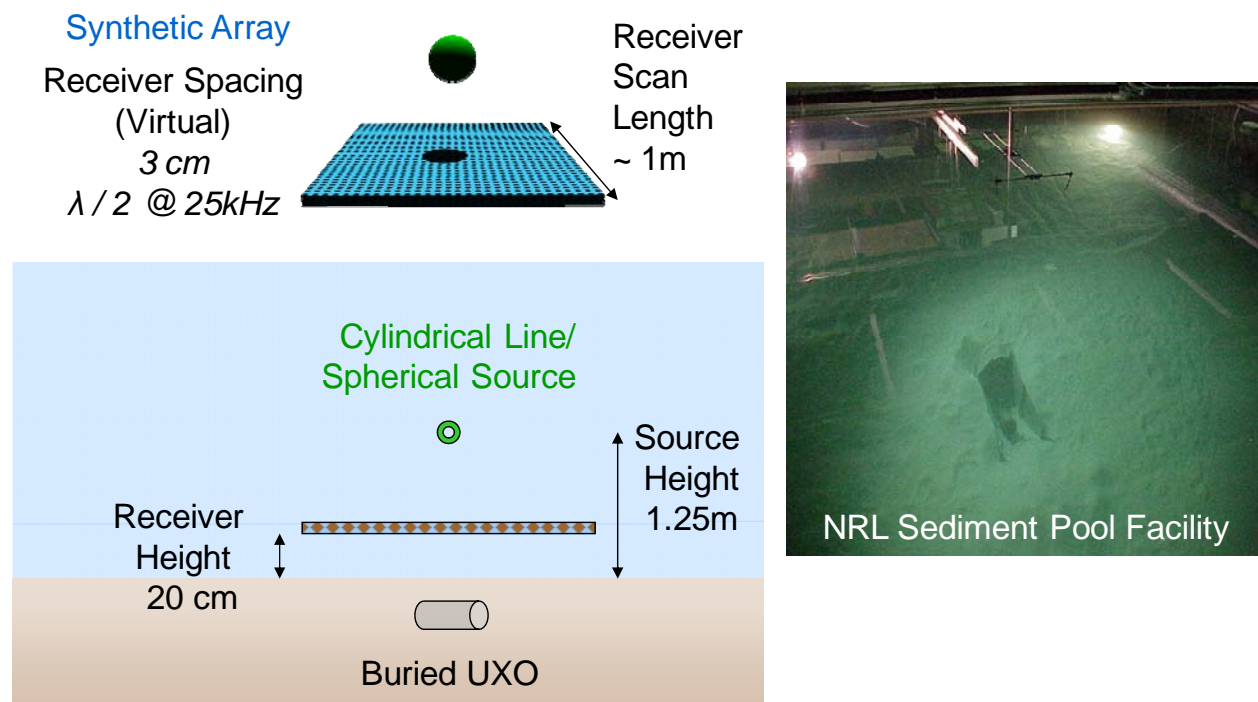
Figure 55 – New Look-Down Measurement System in the NRL Sediment Pool.
The system uses a near-field synthetic receiver array and a single point source.

If we can, in addition, construct velocity and intensity maps as described in the literature, we can also ask the question:

Are the latter more effective for target ID?

Using this new capability, we collected large look-down data from 5 targets buried 10 cm beneath the sediment. These are depicted in Fig. 56 and include the 5 inch rocket buried at a 30 degree pitch angle, the same target buried horizontally, a large rock, a cinder block, and the same cinder block buried with a 45 degree roll.
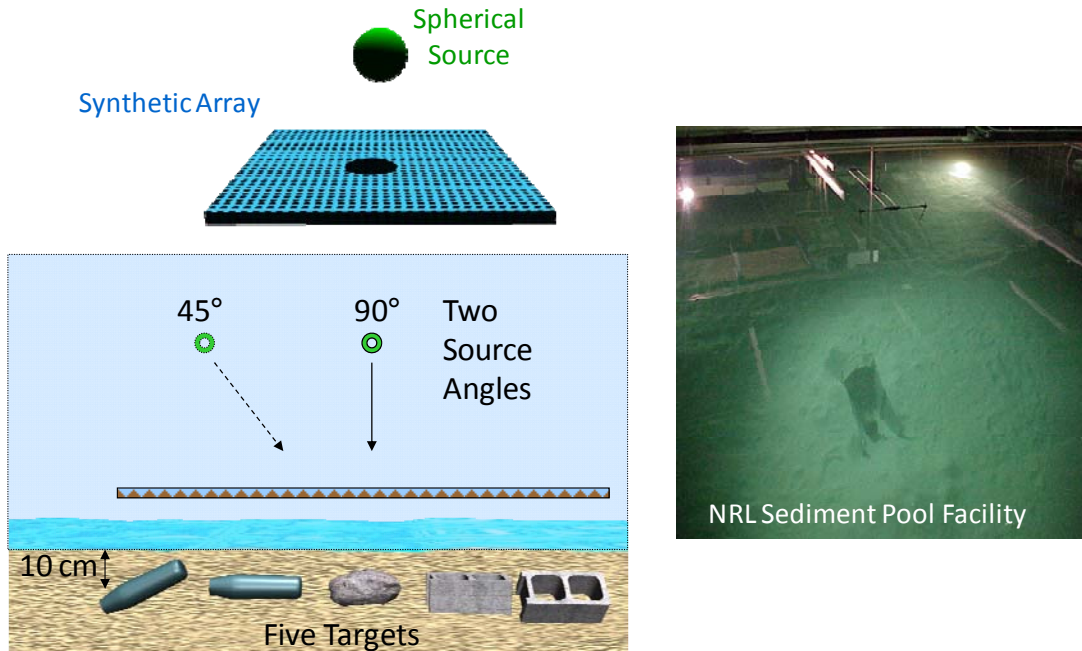
Figure 56 – Diagram for Buried Target Scattering Measurements.

The targets are buried 10 cm below the surface and include a five inch rocket (horizontal and 30 degree pitch), a rock, and a cinder block (flat and a 45 degree roll).

- Geometry is known due to high precision robotic system
- Target returns are isolated by temporal windowing:
    ~ Use a ray-approximation to estimate time of flight values
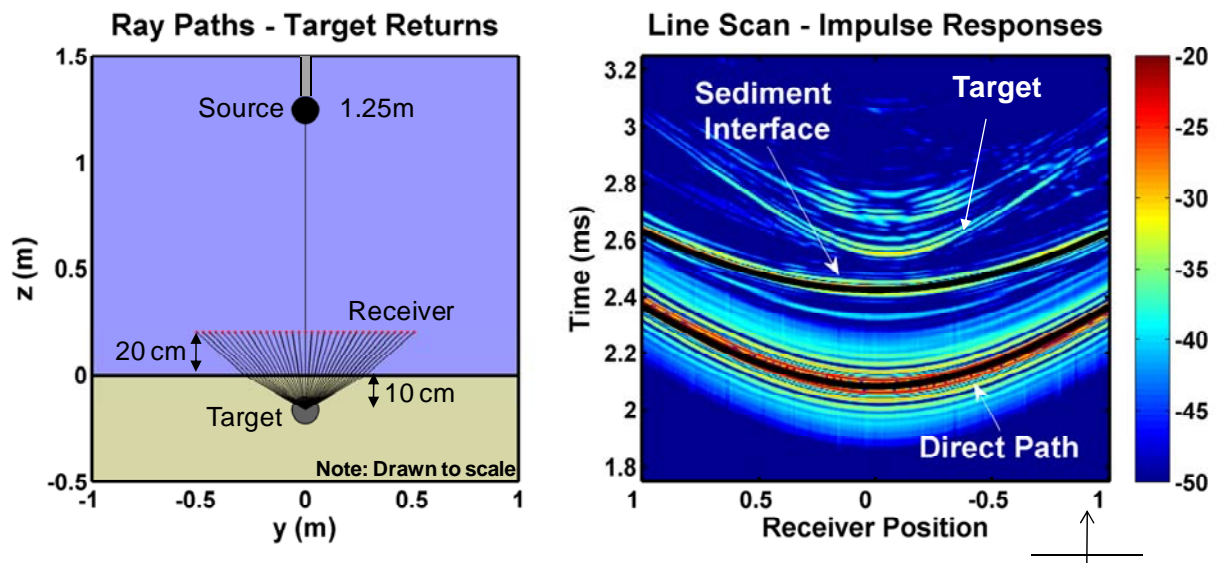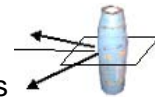
Figure 57 – Sediment Pool Look-Down Measurements.
Geometry and range (time) cross-range (receiver position) plots for one line scan.

An example of the data obtained in this facility is shown in Fig. 57. In the display on the right, one can see the time/cross range signals with the signal from the target echo, the direct source signal, and that from the sediment-water interface indicated. For this display, the data is extracted from the horizontal line depicted in the diagram.
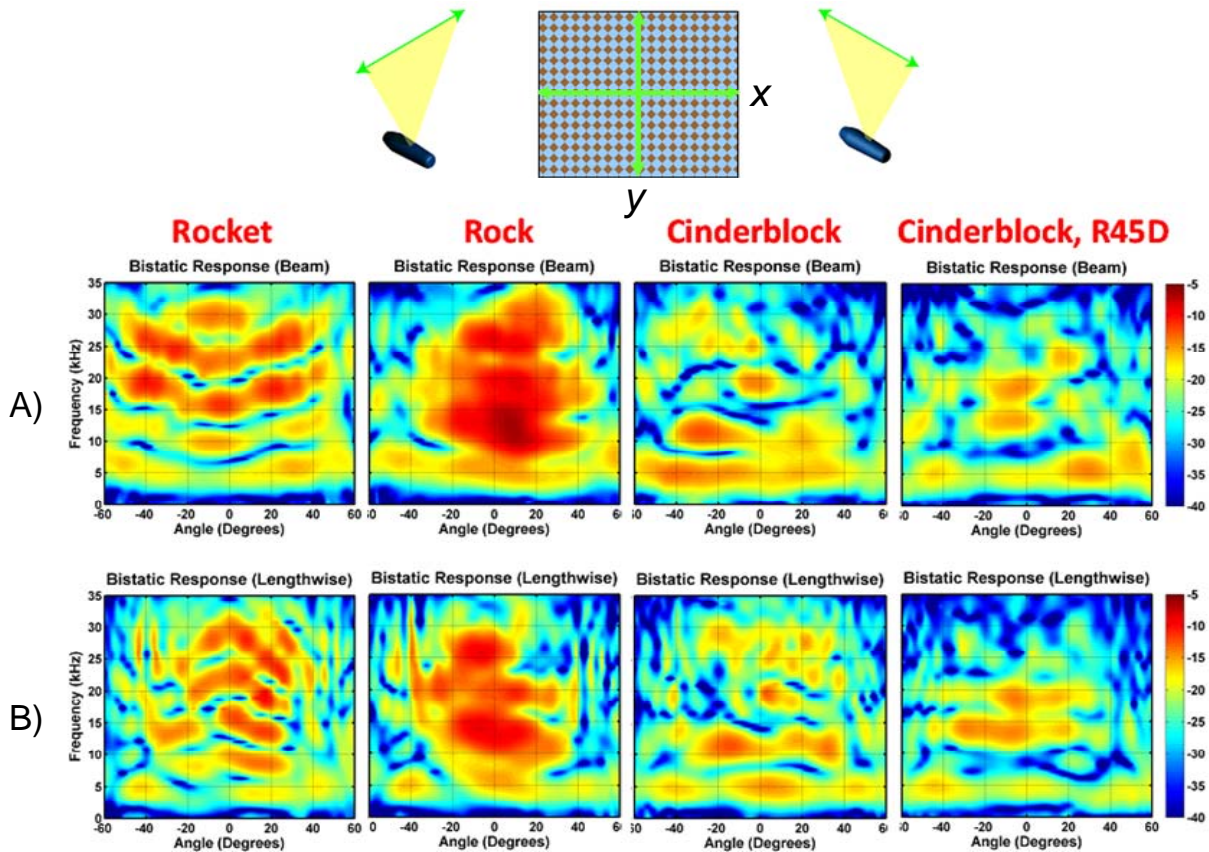
Figure 58 – Target Strength versus Frequency and Angle.
Targets include the five inch rocket, the rock, and the cinder block flat and rolled 45 degrees. Upper displays for line scan A and lower displays for line scan B.

Frequency-angle color maps are shown in Fig. 58 for four of the targets for two orthogonal line arrays. One can see clear differences in the 2-D features for the different targets which implies that one should be able to obtain good target identification based on these structural acoustic features. The complete data set will be analyzed under a new start SERDP program beginning in 2011.

A preliminary study was carried out with this data to examine the degree of target separation for various array sizes and for various amounts of added random noise. The results are shown in Fig 59. As can be seen, there is very good target separation between all the targets

even when only a small number of elements on the receiver array is used. This is very encouraging since a typical look-down receiver system will be much farther from the sediment surface than in this near-field case. The longer-range system would have a smaller angular aperture than that used in this study. But the good separation seen for small array areas in Fig. 59 implies that the longer range system would also have good target separation as well.
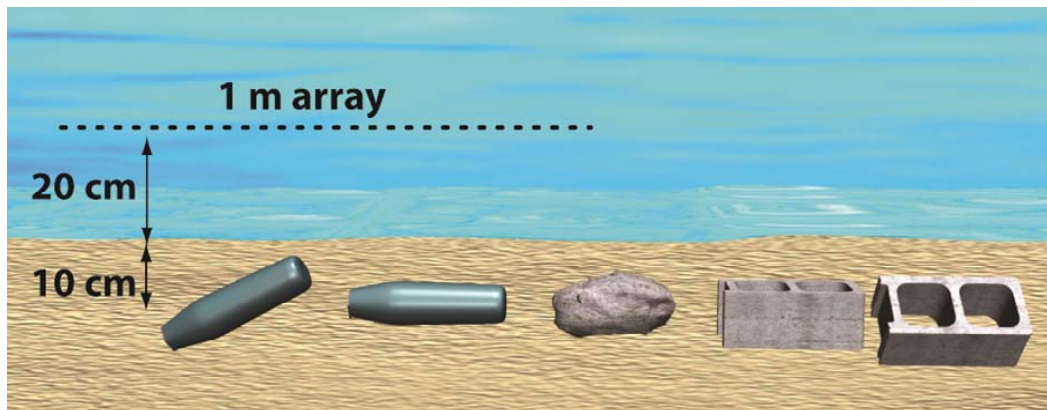
Rocket/False Target Feature Separation
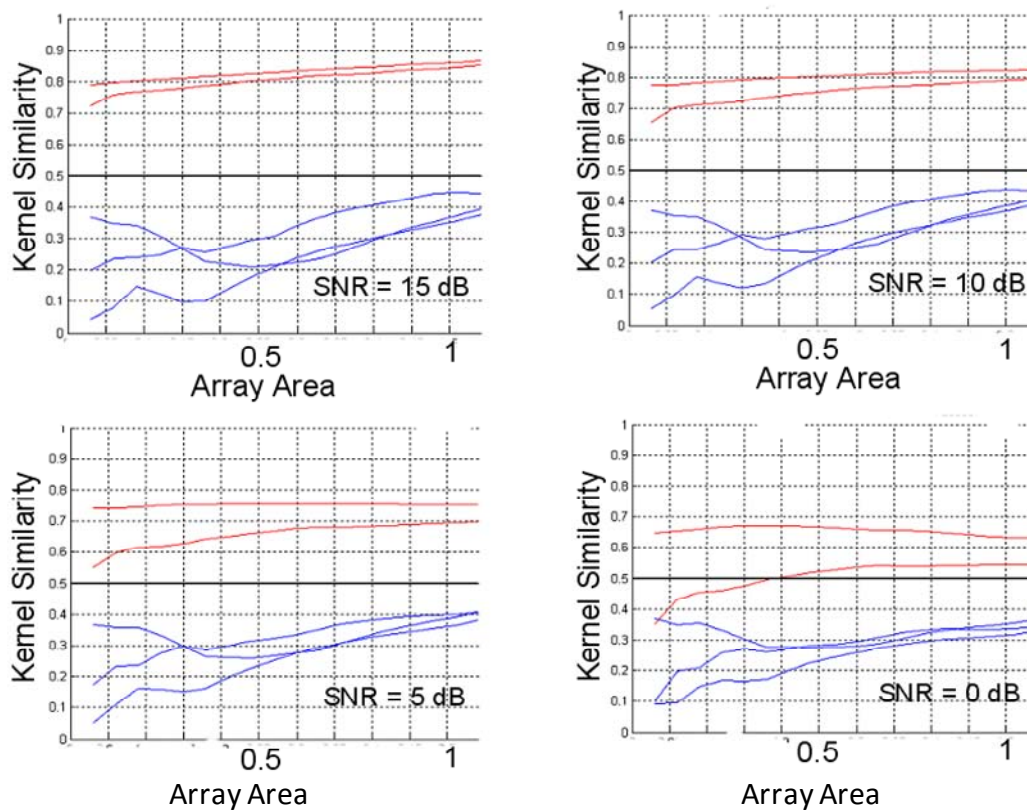
Figure 59 – Target Feature Separation for RVM.

Red curves for the five inch rocket (horizontal and 30 degree pitch) blue curves for the rock and cinder block (flat and rolled 45 degrees) for various S/N ratios.

65

The data was also used to form images using a typical time-based algorithm which incoherently sums up the returns at the receivers properly time delayed using the distance from each scattering point and the particular receiver. The 2-D views of these images are shown in Fig. 60 for the three targets. The clearest image is that of the cinderblock, presumably because the scattering is predominately from the geometric block surfaces. The image of the rocket, known to have elastic responses in this frequency band, exhibits several highlights not compatible with the geometry of the target's surface and probably due to pulse elongation from the elastic effects. It seems reasonable to conclude that fusion in some manner of the RVM identification algorithms and the imaging should improve our ability to identify one target from another, and it is expected that such studies will be undertaken.
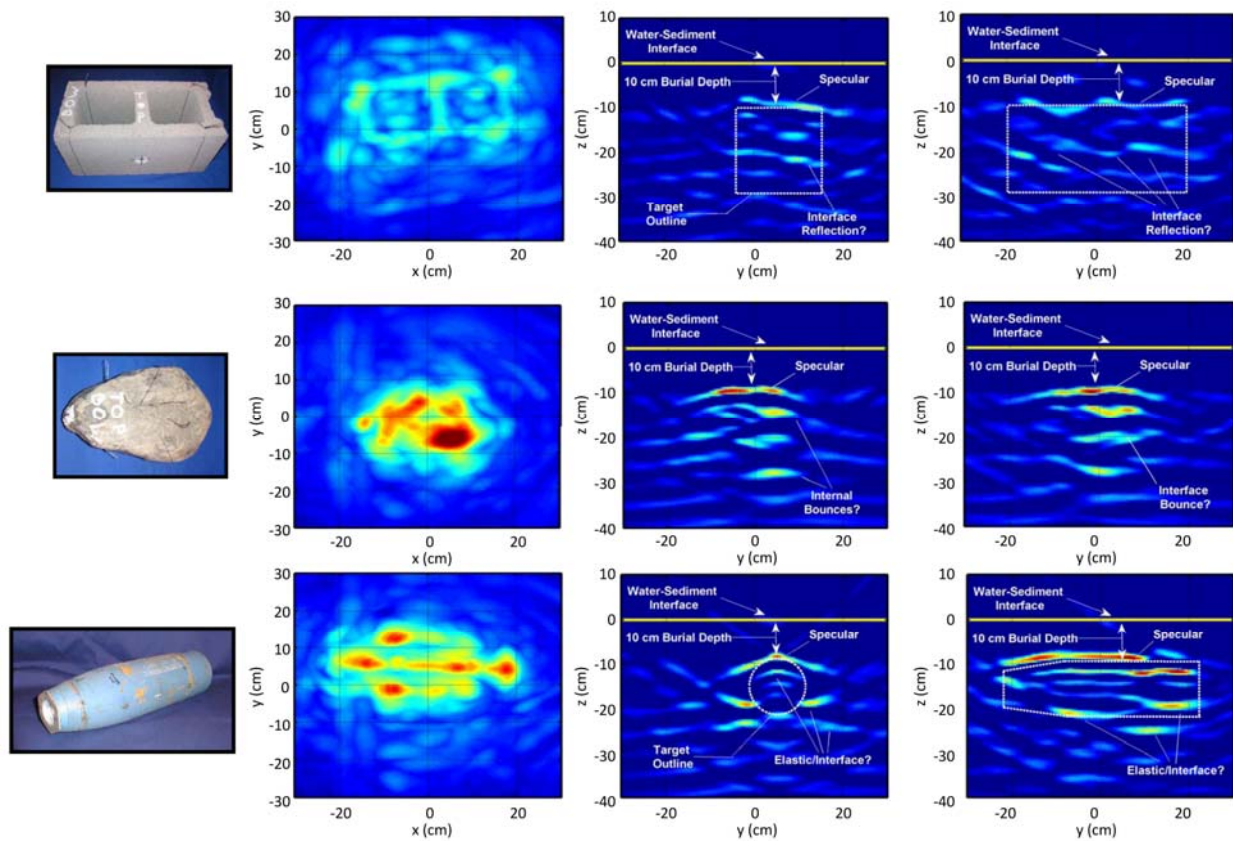
Figure 60 – Buried Target Images.
Three different 2D planes: from left to right plan view, short side view, long side view.

CONCLUSIONS AND IMPLICATIONS FOR FUTURE RESEARCH/IMPLEMENTATION

The conclusions and future implications to be drawn from this research are best understood in the context of Fig. 61 which illustrates the three UXO search sonar configurations in a general sense. Case 1 depicts a long range monostatic system which uses a collocated source and receiver. This configuration can provide a system having the potential for a large area coverage rate. In a typical shallow water environment, in this case the incident waves would strike the water-sediment interface at near grazing angles well below the critical angle. As such, a major issue centers around the question of how much acoustic energy penetrates into the sediment since for buried targets energy must penetrate the sediment, scatter from the target, and then pass back through the sediment-water interface. Both the sediment interface morphology and the acoustic frequency determine whether buried targets can be prosecuted in the Case 1 scenario. For flat surfaces, one must rely on evanescent sound penetration which implies low frequencies since meaningful sound pressure levels are expected to exist to distances about one acoustic wavelength beneath the interface. For surfaces with height fluctuations having sufficiently high magnitudes and lateral wavenumbers, sound penetration into the interface can be significant for higher frequencies as well. However, scattering from the buried object must compete with the incoherent intensity scattered back from the fluctuating interface itself, resulting in a drop in S/N.
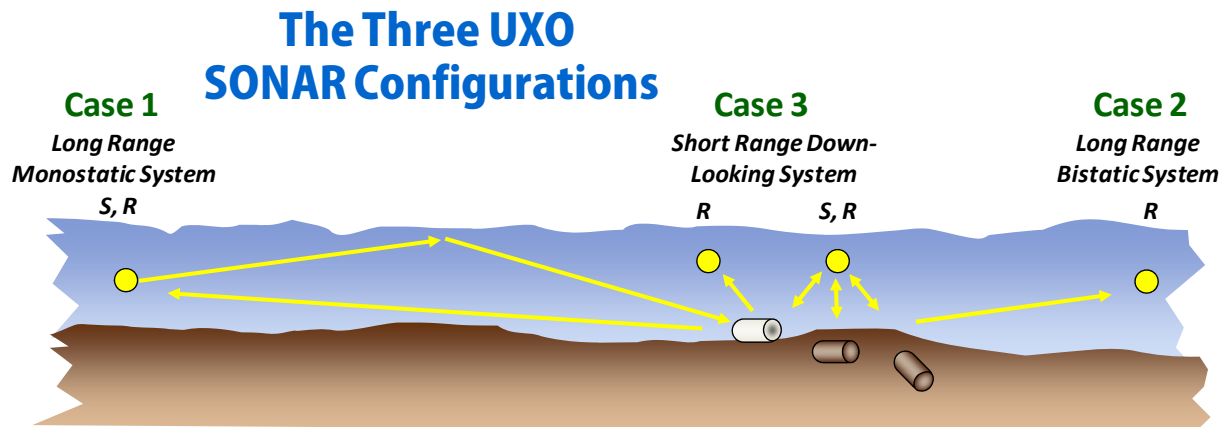
Figure 61 – The Three UXO Sonar Configurations.
Case 1: Long range monostatic below critical angle; case 2 Long range bistatic with special case of forward scatter; and case 3 short range large angle look-down.

The majority of this program's efforts were expended on the Case 1 scenario. For this case, the research clearly established the following. (1) Typical UXO targets of interest have sufficiently high mono-static target strength levels over the structural acoustic frequency band to be detectable out to modest ranges if they are proud or partially buried in the sediment. (2) RVM identification algorithms applied to the structural acoustic features they present allow one to

distinguish between a typical UXO and a false target such as a pipe, cinder block, or rock. Properly trained RVM algorithms can also distinguish between various UXO targets themselves. (3) It must be assumed at this point that RVM training data will have to include the mono-static response of targets of interest for various burial pitch angles in addition to the full range of in-plane aspect angles. (4) Multi-path acoustic propagation characteristic of long range scenarios significantly alters the frequency-angle (acoustic color) features in the backscattered echoes. However, a realistic propagation model (for example, the RAM code) can be used to include this complication in the operation of the RVM identification process.

The issues that remain unresolved with respect to Case 1 include the following. (1) The work thus far has involved pristine UXO targets. For proud and partially buried targets, corrosion or barnacle growth can become significant. Further, some targets may have become deformed in the impact process. At what point do the structural acoustic features become sufficiently modified so as to be associated with a now unknown target? How do we train for targets which are in this category? (2) What is the nature of both the naturally occurring and man-made clutter we can expect to encounter at typical clean-up sites? What are the structural acoustic features of such clutter? (3) How do we train RVM algorithms for use in an area wherein we have no a priori knowledge regarding the types of UXO apt to be there? (4) How far can we push identification algorithms that infer inter-relationships between data collected at the current scene under test, and data collected at previous scenes. Such algorithms are of particular interest here because of the fact that the acoustic signature from targets and clutter may be a relatively strong function of environmental factors, and therefore training (labeled) data from previous environments may or may not be relevant for the new scene under test. By inferring the inter-relationships between multiple data sets, the previous labeled data can be used appropriately. (5) Under what conditions will there be sufficient sound penetration into the sediment to be able to prosecute deeply buried targets?

A relatively modest portion of the program's efforts were expended on the Case 2 long range bi-static scenario. Further, the focus here was almost exclusively on the special case of forward and near-forward scattering. For this case, the research clearly established the following. (1) Numerical and analytic models confirm that for typical UXO forward scattered echo levels remain much higher than typical backscattered levels for all source-to-target aspect angles. (2) Sediment laboratory measurements and numerical simulations have confirmed that forward scattering remains strong for typical UXO targets as the target becomes buried in the sediment. This is in contradistinction to the situation for Case 1 wherein the backscattered echo levels become very low upon burial. (3) The efficacy of a novel wave-number filter-based approach for extracting the forward echo from the overlapping and much stronger incident source signal was demonstrated at 50 meter ranges in 40 feet of water in the Gulf of Mexico. The experimental study used a 60 cm diameter *proud* spherical shell target and a synthetic receiver array formed by a hydrophone moving on a bottom-mounted 48 meter rail. The study successfully obtained the frequency/angle acoustic color maps of the spherical shell at and near forward scatter angles.

The issues that remain unresolved with respect to Case 2 include the following. (1) Can the high forward scatter target strength levels predicted to remain upon burial be accurately extracted using the wave-number (or related) approach in the marine environment? (2) Is there a

practical design for such a system that can also provide some moderate area coverage?

Near the end of the program, some effort was expended addressing in a preliminary fashion some of the issues associated with Case 3, the short-range, down-looking system. The resulting information is now being used to expedite the new SERDP Program MR-2103 which is focused on experimental studies for Case 3 in a real marine environment.

In this preliminary case 3 effort, the following results were achieved. (1) A new sediment laboratory measurement system was implemented. In this design, the receiver array is generated synthetically by robotically moving a receiver over a 2 dimensional planar surface *just above* the sediment surface in order to exploit scientific information that is made available in this very near field. In addition, data is easily propagated up to higher positions more typical of a system in the field so that we do not lose the system-relevant data. For lower part of the SA band, the receiver distance $<< \lambda$ so that we can obtain a so-called nearfield hologram (*NAH*). From this hologram, we can study the following questions: Do evanescent waves matter? Can we project to water/ sediment interface? Can we project to planes below interface? (2) A strategy was developed for processing the acoustic color feature space associated with this 2-D measurement space. (3) 2-D echo data bases were collected on a UXO target and two false targets all of which were buried 10 cm beneath the sediment surface. (4) Preliminary RVM identification algorithms, trained on this data base as well as comparable data bases generated by a finite element-based structural acoustics model, demonstrated good target separability. Good target separation was maintained down to very small receiver array apertures. (5) Simple time-based images were generated on the measured data and exhibited some promise for image based data calls.

The Case (3) scenario is the focus of the new SERDP Program MR 2103 begun in 2011 entitled "Structural Acoustic UXO Detection and Identification in Marine Environments." The issues to be addressed in this new effort are as follows. (1) To what degree are the structural acoustic features to be exploited for target identification dependent upon the sediment, its structure, and the degree of target burial and vertical orientation? (2) How should the RVM algorithms and training exercises best be extended to the 2-D look-down case? (3) How will the ID algorithms perform in the presence of real environmental clutter, multi-path, and interface scattering? (4) How does the sediment, its structure, or out-of-plane target orientations alter the frequency/angle characteristics of proud or buried UXO? (5) How do these effects depend on the sediment surface roughness? (6) In designing a vehicle-borne structural acoustic sonar, how should one fuse volumetric sonar, vehicle motion, and newly developed processing, classification, and imaging algorithms able to efficiently detect, localize, and classify in-water UXO targets in a range of environments? (7) How can one maximize the number of opportunities of illuminating the range of target aspects most effective for implementing structural acoustic feature-based target identification and minimize the number of passes at different headings needed to survey the area of interest? (8) How might one optimize the receiver array gain so as to maximize the ratio of target echo amplitude and sediment surface scattering which acts as background noise. (9) How can one provide sufficient receiver aperture and sensor density for squint processing to obtain multi-aspect scattering data?

LITERATURE CITED

1. B. H. Houston, J.A. Bucaro, T. Yoder, L. Kraus, and J. Tressler, J. Fernandez, T. Montgomery,T. Howarth, "Broadband Low Frequency Sonar for Non–Imaging Based Identification," IEEE Oceans 2002.

2. H. J. Simpson and B. H. Houston, "Laboratory Measurements of Sound Scattering from a Buried Sphere Above and Below the Critical Angle," J. Acous. Soc. Am. 113, 2003.

3. P. Runkle, L. Carin, L. Couchman, T. Yoder, and J. Bucaro, "Multi–aspect Identification of Submerged Elastic Targets via Wave–based Matching Pursuits and Hidden Markov Models," J. Acous. Soc. Am., vol. 106, pp. 605–616, 1999.

4. P. Runkle, L. Carin, L. Couchman, T.J. Yoder, and J.A. Bucaro, "Multi–Aspect Target Identification with Wave–Based Matching Pursuits and Continuous Hidden Markov Models," IEEE Trans. Pattern Analysis and Machine Intelligence, vol. 21, pp. 1371–1378, 1999.

5. B. H. Houston, "Structural Acoustic Laboratories at NRL in Washington, D.C," J. Acoust. Soc. Am. 92(4), 1992.

6. H.J. Simpson, E.C. Porse, B.H. Houston, L.A. Kraus, A.R. Berdoz, P.A. Frank, and S.W. Liskey, "Very low frequency scattering experiments from proud targets in a littoral environment using a 55 meter rail," J. Acoust. Soc. Am. Suppl. 114, 2003.

7. M. Tipping, "Sparse Bayesian Learning and the Relevance Vector Machine," Journal of Machine Learning Research, 1, 211-244, 2001.

8. Xuejun Liao, Hui Li, and Balaji Krishnapuram, "An M-ary KMP Classifier for Multi-aspect Target Classification," Proceedings of IEEE International Conference on Acoustics, Speech, and Signal Processing (ICASSP), 2, 61-64, 2004.

9. J.A. Bucaro, B.H. Houston, M. Saniga, L.R. Dragonette, T. Yoder, S. Dey, L. Kraus, and L. Carin, "Broadband acoustic scattering measurements of underwater unexploded ordnance (UXO)," J. Acoustic. Soc. Am. 123, 738-746 (2008).

10. R. J. Urick, "Principles of Underwater Sound", Third Edition, pp 17-30, McGraw-Hill, Inc. 1983.

11. C. S. Clay and H. Medlin, "Acoustical Oceanography: Principles and Applications," pp 96 - 102, John Wiley & Sons, 1977.

12. S. Stanic, C.K. Kirkendall, A.B. Tveten, and T. Barock, "Passive Swimmer Detection," NRL Review, 97-98, 2004.

13. Urick, op. cit., pp 291-327.

14. S. Dey and D.K. Datta, "A parrallel hp-FEM infrastructure for three-dimensional structural acoustics," Int. J. Numer. Meth. Eng. 68, 583-603, 2006.

15. R.D. Doolittle and H. Uberall, "Sound scattering by elastic cylindrical shells, "J.Acoust. Soc. Am. 39 (2), 272-275, 1966.

16. L. Flax and W. Neubauer, "Acoustic reflection from layered elastic absorbtive cylinders," J.Acoust. Soc. Am. 61 (2), 307-312, 1977.

17.   "A Handbook of Sound and Vibration Parameters", prepared for the Naval Sea Systems Command, by the Systems Technology Department, General Dynamics Electric Boat Division, September 18, 1978.

18.   B. Krishnapuram and L. Carin, "Support Vector Machines for Improved Multi-Aspect Target Recognition Using the Fisher Kernel Scores of Hidden Markov Models," Proceedings of IEEE International Conference on Signal Processing, 3, 2989-2992, 2002.

19.   N. Dasgupta, P. Runkle, L. Carin, L. Couchman, T. Yoder, J. Bucaro, and G. Dobeck, "Class-Based Target Identification with Multiaspect Scattering Data," IEEE J. Oceanic Engineering, 28, 271-282, 2003.

20.   Robert, C. P., and Casella, G. *Monte Carlo statistical methods*, Springer-Verlag, 1999.

21.   Xuejun Liao, Ya Xue, and Lawrence Carin, "Logistic Regression with an Auxiliary Data Source", The 22nd International Conference on Machine Learning (ICML), 2005.

22.   B. Schölkopf and A. Smola, *Learning with Kernels Support Vector Machines, Regularization, Optimization and Beyond*, MIT Press, Cambridge, MA, 2002.

23.   T. M. Cover and J. A. Thomas, *Elements of Information Theory*, John Wiley, New York, 1991.

24.   V. V. Fedorov, *Theory of Optimal Experiments*, Academic Press, New York, 1972.

25. David Calvo, Brian Houston, Joseph Bucaro, Larry Kraus, Harry Simpson, Angie Sarkissian, "Scattering by unexploded ordnance (UXO) with variable burial depth and seafloor roughness: a parametric study," October 26, 2009 158th ASA Meeting, San Antonio, TX.

26.   D.C. Calvo, K.E. Rudd, M. Zampolli, W.M. Sanders, and L.D. Bibee, "Simulation of acoustic scattering from an aluminum cylinder near a rough interface using the elastodynamic finite integration technique," accepted for publication in Wave Motion.

27.   Harry J. Simpson, Brian H. Houston, and Raymond Lim, "Laboratory measurements of sound scattering from a buried sphere above and below the critical angle," J. Acoustic. Soc. Am. 113, 39-42 (2003).

28.   J.L. Lopes, C.L. Nesbit, R. Lim, D. Tang, K.L. Williams, and E.I. Thorsos, "Shallow grazing angle sonar detection of targets buried under a rippled sand interface," Proceedings of Oceans 2002,Biloxi, MS, Oct. 28-Nov.1 (2002).

29.   A. Tesei, J.A. Fawcett, and R. Lim, "Physics-based detection of man-made elastic objects buried in high-density-clutter areas of saturated sediments," Appl. Acoust. 69, 422-437 (2008).

30.   J.A. Bucaro, H. Simpson, L. Kraus, L.R. Dragonette, T. Yoder, and B.H. Houston, "Bistatic scattering from submerged unexploded ordnance lying on a sediment," J. Acoustic. Soc. Am. 126, 2315-2323 (2009).

31.   R. A. Ross, "Forward scattering from a finite, circular cylinder," Progress in Electromagnetics Research C, 2, 207-215 (2008).

32.   J.J. Bowman, T.B.A. Senior, and P.L.E. Uslenghi, *Electromagnetic And Acoustic Scattering by Simple Shapes*, 89-91, Hemisphere Publishing Corporation, New York (1987).

33.   Angie Sarkissian, "Extraction of a target scattering response from measurements made over long ranges in shallow water," J. Acoust. Soc. Am. **102**, 825-832(1997).

34. F. Yong, Z. Zheng-ou, and X. Jia-li, "Clutter reduction based on apex shifted radon transform in sub-surface forward-looking ground penetrating radar," International Conference on Radar CIE'06, 1-3, INSPEC # 9431360 (2006).

35. J.A. Bucaro, B.H. Houston, H.J. Simpson, L.R. Dragonette, L. Kraus, and T. Yoder, "Exploiting forward scattering for detecting submerged proud/half-buried unexploded ordnance," J. Acous. Soc. Am. **126**, EL171-EL176 (2009).

36. L. Kraus, J.A. Bucaro, B.H. Houston, A.R. Berdoz, D.L. Amon, P.A. Frank, S.W. Liskey, H. Simpson, and D. Calvo, "Forward scatter target strength extraction in a littoral environment," J. Acoust. Soc. Am. (2010).

37. Harry J. Simpson, Zachary J. Waters, David C. Calvo, Brian H. Houston, Alain R. Berdoz, Danial L. Amon, Philip A. Frank, Steve W. Liskey, Larry A. Kraus, Joseph A. Bucaro, "Forward scatter and backscatter low frequency synthetic array measurements of the structural acoustic response from proud targets using a 48 m long rail in a littoral environment," J. Acoust. Soc. Am. (2010)

38. M.D. Collins, "Generalization of the split-step Pade," J. Acoust. Soc. Am. 96, 382-385 (1994).

39. M.D. Collins, R. J. Cederberg, D.B. King, and S.A. Chin-Bing, "Comparison of algorithms for solving parabolic wave equations," J. Acoust. Soc. Am. 100, 178-182 (1996).

40. Jung-Ho Kim, Seong-Jun Cho, and Myeong-Jong Yi, "Removal of ringing noise in GPR data by signal processing," Geosciences J., **11**, 75-81 (2007).

41. T.K. Stanton, "Sound scattering by spherical and elongated shelled bodies," J. Acoust. Soc. Am. **88**, 1619-1633 (1990).

42. Earl G. Williams, *"Fourier Acoustics: Sound Radiation and Nearfield Holography,"* Academic Press, San Diego CA, (1999).

APPENDIX

A. Supporting Data: NA

B. List of Scientific/Technical Publications:

Articles in Peer-Reviewed Journals

H. J. Simpson, C. K. Frederickson, E. C. Porse, B. H. Houston, L. A. Kraus, S. W. Liskey, A. R. Berdoz, P. A. Frank, and S. Stanic, "Measurements of sound propagation in a littoral environment using a vertical synthetic array," J. Acoust. Soc. Am. 121, 85-97 (2007).

J.A. Bucaro, B.H. Houston, M. Saniga, L.R. Dragonette, T. Yoder, S. Dey, L. Kraus, and L. Carin, "Broadband acoustic scattering measurements of underwater unexploded ordnance (UXO)," J. Acous. Soc. Am. 123, 738-746 (2008).

J.A. Bucaro, H. Simpson, L. Kraus, L.R. Dragonette, T. Yoder, and B.H. Houston, "Bistatic scattering from submerged unexploded ordnance lying on a sediment," J. Acous. Soc. Am. 126, 2315-2323 (2009).

J.A. Bucaro, B.H. Houston, H. Simpson, L.R. Dragonette, L. Kraus, and T. Yoder, "Exploiting forward scattering for detecting submerged proud/half-buried unexploded ordnance," J. Acous. Soc. Am. 126, EL171-EL176 (2009).

J.A. Bucaro, L. Kraus, B.H. Houston, A. Sarkissian, and H. Simpson, "Forward Scatter Target Strength Extraction in a Marine Environment," conditionally accepted for publication as a Letter to the Editor in the Journal of the Acoustical Society of America.

S. Dey, A. Sarkissian, H. Simpson, B.H. Houston, F.A. Bulat, L. Kraus, M. Saniga, and J.A. Bucaro, "Structural-acoustic modeling for three-dimensional freefield and littoral environments with verification and validation," conditionally accepted for publication as a regular article in the Journal of the Acoustical Society of America.

Technical Reports

J. A. Bucaro, B.H. Houston, M. Saniga, H. Nelson, T. Yoder, L. Kraus, and L. Carin,
"Wide Area Detection and Identification of Underwater UXO Using Structural Acoustic Sensors: SERDP Annual Report," NRL/MR/7130--06-9014, December 1, 2006.

J. A. Bucaro, B.H. Houston, M. Saniga, A. Sarkissian, H. Nelson, T. Yoder, L. Kraus, and L. Carin, "Wide Area Detection and Identification of Underwater UXO Using Structural Acoustic Sensors: SERDP Annual Report," NRL/MR/7130—08-9103, August 12, 2008.

J. A. Bucaro, B.H. Houston, H. Simpson, L. Kraus, T. Yoder, M. Saniga, A. Sarkissian, and L. Carin, "Wide Area Detection and Identification of Underwater UXO Using Structural Acoustic Sensors: SERDP 3'rd Annual Report," January 1, 2009.

J. A. Bucaro, B.H. Houston, H. Simpson, D. Calvo, L. Kraus, T. Yoder, M. Saniga, and A. Sarkissian, "Wide Area Detection and Identification of Underwater UXO Using Structural Acoustic Sensors: SERDP 4'th Annual Report," NRL/MR/7130—10-9261, July 21, 2010.

Conference or Symposium Proceedings

D.C. Calvo, B.H. Houston, J.A. Bucaro, L. Kraus, H.J. Simpson, and A. Sarkissian. "Using sound to detect unexploded ordnance (UXO) with variable burial depth and seafloor roughness", ASA-AIP Online Lay-Language Article for the Acoustical Society of America Conference, San Antonio, November 2009.

Conference or Symposium Abstracts

J.A. Bucaro and B.H. Houston, "Sonar Systems for Prosecuting Underwater UXO," SERDP Partners in Environmental Technology Technical Symposium and Workshop, Washington, D.C., Dec. 2-4 (2008).

Joseph A. Bucaro, Brian H. Houston, Larry Kraus, Harry J. Simpson, David Calvo, and Louis R. Dragonette, "Bistatic Scattering from Underwater Unexploded Ordinance and the Impact of Burial," J. Acoust.Soc. Am. 125, 2733, 157th Meeting of the Acoustical Society of America, Portland, OR (May 2009).

Saikat Dey, Angie Sarkissian, Eris S. Mestreau, Brian H. Houston, and Larry Kraus, "Three-dimensional structural-acoustics modeling and its validation for free-field and littoral environments," J. Acoust. Soc. Am. 125, 2702, 157th Meeting of the Acoustical Society of America, Portland, OR (May 2009).

Harry J. Simpson, Brian H. Houston, Mike L. Saniga, Joseph A. Bucaro, Alain R. Berdoz, and Larry Kraus, "The broadband in-water structural acoustics of unexploded ordinance: tank comparisons with at-sea rail measurements," J. Acoust. Soc. Am. 125, 2733, 157th Meeting of the Acoustical Society of America, Portland, OR (May 2009).

David C. Calvo, Brian H. Houston, Joseph A. Bucaro, Larry Kraus, Harry J. Simpson, Angie Sarkissian, "Using sound to detect unexploded ordnance (UXO) with variable burial depth and

seafloor roughness," October 26, 2009 158th ASA Meeting, San Antonio, TX.

David Calvo, Brian Houston, Joseph Bucaro, Larry Kraus, Harry Simpson, Angie Sarkissian, "Scattering by unexploded ordnance (UXO) with variable burial depth and seafloor roughness: a parametric study," October 26, 2009 158th ASA Meeting, San Antonio, TX.

Harry J. Simpson, Zachary J. Waters, David C. Calvo, Brian H. Houston, Alain R. Berdoz, Danial L. Amon, Philip A. Frank, Steve W. Liskey, Larry A. Kraus, and Joseph A. Bucaro, "Forward scatter and backscatter low frequency synthetic array measurements of the structural acoustic target strength from proud targets using a 48 m long rail in a littoral environment," Acoustical Society of America , 159th Meeting - Baltimore, MD 19-23 April 2010.

Zachary J. Waters, Harry J. Simpson, Brian H. Houston Alain R. Berdoz, and Larry Kraus, "Detection of a resonant target in shallow water using iterative, single-channel time reversal at low frequencies (1-25 kHz)," Acoustical Society of America , 159th Meeting - Baltimore, MD 19-23 April 2010.

L. Kraus, J.A. Bucaro, B.H. Houston, A. R. Berdoz, D.L. Amon, P.A. Frank, S. W. Liskey, H. Simpson, and D. Calvo, "Forward Scatter Target Strength Extraction in a Littoral Environment," Acoustical Society of America , 159th Meeting - Baltimore, MD 19-23 April 2010.

J. A. Bucaro, B.H. Houston, H. Simpson, T. Yoder, Z. Waters, M. Saniga, A. Sarkissian, L. Kraus, and D. Calvo, "Broadband, Multi-Aspect Scattering from Proud and Buried UXO," SERDP Partners in Environmental Technology Technical Symposium and Workshop, Washington, D.C., Nov. 29 - Dec. 2 (2010).

C. Other Supporting Materials (Scientific Awards or Honors):

SERDP 2009 Munitions Management Project of the Year Award